SEARCH FOR PAIR PRODUCTION OF SCALAR TOP QUARKS IN JETS AND MISSING TRANSVERSE ENERGY CHANNEL WITH THE D0 DETECTOR

by

MANSOORA SHAMIM

Diploma, The Abdus Salam ICTP – Italy, 2000
M.S., University of the Punjab – Pakistan, 1998

AN ABSTRACT OF A DISSERTATION

submitted in partial fulfillment of the
requirements for the degree

DOCTOR OF PHILOSOPHY

Department of Physics
College of Arts and Sciences

KANSAS STATE UNIVERSITY
Manhattan, Kansas
2008

Abstract

This dissertation describes a search for the pair production of scalar top quarks, $\tilde{t}_1$, using a luminosity of 995 pb^{-1} of data collected in $p\bar{p}$ collisions with the D0 detector at the Fermilab Tevatron Collider at a center-of-mass energy $\sqrt{s} = 1.96$ TeV. Both scalar top quarks are assumed to decay into a charm quark and a neutralino, ($\tilde{\chi}_1^0$), where $\tilde{\chi}_1^0$ is the lightest supersymmetric particle. This leads to a final state with two acoplanar charm jets and missing transverse energy. The yield of such events in data is found to be consistent with the expectations from known standard model processes. Sets of $\tilde{t}_1$ and $\tilde{\chi}_1^0$ masses are excluded at the 95% confidence level that substantially extend the domain excluded by previous searches. With the theoretical uncertainty on the $\tilde{t}_1$ pair production cross section taken into account, the largest limit for $m_{\tilde{t}_1}$ is $m_{\tilde{t}_1} > 150$ GeV, for $m_{\tilde{\chi}_1^0} = 65$ GeV.

SEARCH FOR PAIR PRODUCTION OF SCALAR TOP QUARKS IN JETS AND MISSING TRANSVERSE ENERGY CHANNEL WITH THE D0 DETECTOR

by

Mansoora Shamim

Diploma, The Abdus Salam ICTP – Italy, 2000
M.S., University of the Punjab – Pakistan, 1998

A DISSERTATION

submitted in partial fulfillment of the
requirements for the degree

DOCTOR OF PHILOSOPHY

Department of Physics
College of Arts and Sciences

KANSAS STATE UNIVERSITY
Manhattan, Kansas
2008

Approved by:

Major Professor
T. A. Bolton

Abstract

This dissertation describes a search for the pair production of scalar top quarks, $\tilde{t}_1$, using a luminosity of 995 pb^{-1} of data collected in $p\bar{p}$ collisions with the D0 detector at the Fermilab Tevatron Collider at a center-of-mass energy $\sqrt{s} = 1.96$ TeV. Both scalar top quarks are assumed to decay into a charm quark and a neutralino, ($\tilde{\chi}_1^0$), where $\tilde{\chi}_1^0$ is the lightest supersymmetric particle. This leads to a final state with two acoplanar charm jets and missing transverse energy. The yield of such events in data is found to be consistent with the expectations from known standard model processes. Sets of $\tilde{t}_1$ and $\tilde{\chi}_1^0$ masses are excluded at the 95% confidence level that substantially extend the domain excluded by previous searches. With the theoretical uncertainty on the $\tilde{t}_1$ pair production cross section taken into account, the largest limit for $m_{\tilde{t}_1}$ is $m_{\tilde{t}_1} > 150$ GeV, for $m_{\tilde{\chi}_1^0} = 65$ GeV.

Table of Contents

List of Figures

List of Tables

ACKNOWLEDGMENTS

First of all I am thankful to God for giving me the opportunity to get education in a country that has been playing a leading role in the field of knowledge for many decades. Without His special blessings it would not have been possible.

I am sincerely thankful to my adviser Prof. Tim Bolton for making me join Kansas State University by writing a strong invitation letter in addition to the formal one. His constant guidance and support helped me a lot in overcoming the difficulties that came in the way of completing this dissertation. There never was an occasion when he did not understand the problem that I wanted to explain to him. After listening to the problem he always came up with an answer. I am very thankful to him for giving me the opportunity to stay in the academic environment available at the Fermilab, a place where many students in the physics community dream to carry out research activities. I have always been impressed by his intellectual thinking and the ways of handling the problems that are different from other people. His sense of humor and the little amusing things that he mentioned from time to time, made me see the light at the other end of the tunnel even in very difficult times. Many many thanks for all the useful discussions I had with him over the last several years.

I am especially thankful to Dr. Talat Rahman, who is no longer at KSU, but she is the one who joined Dr. Bolton and advised me to be a part of KSU high energy physics group. She has been extremely helpful and encouraging both, academically and socially and a source of inspiration and strength for a female student coming from a third world country. The great parties that were held at her place and the food that was served will never be forgotten. I am also thankful to all my teachers who taught me physics during the first two years at KSU.

I am extremely thankful to all my D0 colleagues whose efforts have brought this dissertation to a completion. Without their dedicated work and tireless efforts in keeping the detector running and providing necessary support to make the essential ingredients for the analysis available, this thesis would not have been written. Thanks to the spokes person, the physics coordinators and the con-

veners of new phenomenon and jet plus $\not\!\!E_T$ subgroup for providing positive and useful feedback on the analysis. Their efforts made it possible to submit the results for publication in a timely manner.

Special thanks to my teacher Prof. Mujahid Kamran in Pakistan who has been in a state of continuous transition, from Professor and Chairman to Dean Faculty of Sciences to Vice Chancellor of the University of the Punjab, during the time I started and finished my Ph.D. He is the one whom I first requested to guide me to get a Ph.D degree when I was doing my masters at Punjab University. He promised to do that and later on made it possible not only for me but for many other students. His continuous moral support and encouragement, over the phone and through his visits to the U.S, have been a great source of strength. I owe him a lot as he is the one who always believed in me and told me that I would get the degree. Thanks so much sir for making me believe in myself.

I do not think I have words to thank my parents for their support and sending me so far from home for such a long time. Their prayers have played an important role in achieving my goals. Thanks to my brothers and sister for being supportive and listening to me whenever I needed to share my problems and difficulties with someone. I am thankful to my friend Mahsana who has been with me since 2001. We learned a lot from each other both academically and socially. I cannot forget to thank Prof. Masood and his wife the late auntie Ghazala, who always thought of me as their surrogate daughter, for their useful advice and unconditional love.

Thanks to Mudessar and Wajiha for the social gatherings and providing us with the company of Rohan and Sabih. They were a reason to smile in the times of stress. Thanks to all other members of the Pakistani community for appreciating my "pakoras" so much and taking time to have many memorable parties.

DEDICATION

To my parents,

brothers and sister

Chapter 1

Overview

Particle physics is the study of fundamental constituent of matter and the interactions between them. The four types of forces through which particles interact with each other are strong, electromagnetic, weak and gravitational interactions. The strong force, that exist at the sub-nuclear level holds quarks together within hadrons. The electromagnetic force is responsible for chemical reactions as well as electrical and magnetic phenomena. The weak force manifests itself in radioactivity and β-decays while the gravitational interaction is responsible for gravity. Gravitational force is only important at the large scale and can be ignored when we talk about the objects whose sizes are of the order of 1 fm (10^{-15}m). All elementary particles which make up the matter of the universe are spin $1/2$ particles and are divided into two groups: quarks and leptons. Quarks are strongly interacting particles due to the color charge that carry, but they also experience electromagnetic force due to the electric charge and weak force due to the two different helicity states they can have. Leptons on the other hand experience only weak and electromagnetic forces. Examples of leptons include electron ($e^{\pm}$), muon ($\mu^{\pm}$), tau ($\tau^{\pm}$) and neutrinos ($\nu, \bar{\nu}$), while those for quarks include up quark (u), down quark (d), charm quark (c), strange quark (s), top quark (t), bottom quark (b).

Bound states of quarks are known as hadrons. A pair of quark and anti-quark can be combined to make up a meson while three quarks make up a baryon. The proton is an example of a baryon as it is made up of two up-type and one down-type quarks. π^+ is an example of a meson and is made up of an up-type and an anti down-type quarks. The interactions among elementary particles occur

through the exchange of particles that carry spin 1 and are known as gauge vector bosons. The examples include gluons, $W^{\pm}, Z^{o}, \gamma$ responsible for mediating strong, weak and electromagnetic interactions, respectively among the particles.

In particle physics the model that describes the properties of elementary particles and interactions among them is known as standard model (SM). There is one elementary scalar (spin 0) particle within the SM that is introduced to generate masses for all quarks, leptons and gauge bosons, and is called Higgs boson. This is still a hypothetical particle and its discovery will help to understand many unanswered questions within the SM. Many physicists believe that SM is only an effective low energy theory and physics beyond the SM does exist.

Supersymmetry (SUSY) provides a possible extension of the symmetry that SM possess and can answer a few other questions (explained in detail in Chapter 2). In SUSY, each SM particle is assigned one partner with identical quantum numbers except spin being different by half a unit. In the construction of SUSY theory, there is no mechanism to avoid the violation of lepton and baryon number conservation. The non conservation of these quantum numbers may lead to a faster decay of proton which has not been observed yet. In order to avoid such interactions a symmetry know as R-parity is imposed. As a consequence of R-parity conservation all SUSY particles must be produced in pairs and all heavy SUSY particles will eventually decay into the lightest SUSY particle (LSP). It is believed that the LSP should be neutral and stable. In this dissertation LSP is denoted as $\tilde{\chi}_1^0$. The SUSY partner of the top quark is called scalar top quark as it has spin zero and is denoted by $\tilde{t}_1$.

The scalar top quark is a strongly interacting particle and should be produced copiously in hadron colliders. Its production cross section depends on its mass. The mass of the particle is not predicted by SUSY but it is a free parameter that needs to be determined experimentally. There are several theoretical reason which make physicist believe that the scalar top quark can be light enough to be produced at a center of mass energy available at the Fermilab Tevatron collider. Furthermore depending on its mass it can have several different decay modes. This thesis presents details of a search for scalar top quark production and decay via the process $p\bar{p} \rightarrow \tilde{t}_1\tilde{t}_1 \rightarrow c\bar{c}\tilde{\chi}_1^0\tilde{\chi}_1^0$, which

produces a final state with two charm-quark jets plus $\not\!\!E_T$. $\not\!\!E_T$ is the imbalance in the energies of the initial and final state particles in the plane transverse to the beam axis. The missing transverse energy indicates the presence of particles that are neutral and do not interact with the detector material and neutralino is one such candidate. The result presented here is based on the full 1.2 fb^{-1} of Run IIa dataset. The data were collected with the D0 detector located at the Fermilab Tevatron Collider. Certain selection criteria are applied to select signal like events in data. The background contributions are estimated from simulated Monte Carlo (MC) samples. In the end the observed number of events in data are compared with the expected number of background and signal events. Since we do not see any significant excess in data over the expected background therefore we exclude the possibility of having any signal in the data. The organization of the thesis is as follows.

In Chap. 2, we describe the theoretical background and the motivation to have supersymmetry as a theory for physics beyond the SM. In Chap. 3, after reviewing the scalar top quark mass matrix, we discuss its production cross section and, the decay channels. Chapter 4 describes an overview of the accelerator complex at Fermilab and the D0 detector. Chapter 5 states how we identify physics objects such as the jets, electrons etc. and, reconstruct events using the information recorded in $p\bar{p}$ collisions. In Chap. 6 we present the details of data and simulated MC samples used to carry out the search. In Chap. 7 we outline the details of the study of $Z/\gamma^*(\rightarrow ee)+$ jets events. We use this dataset to normalize the vector boson plus jets background in the scalar top quark search. We adapted this procedure to reduce the normalization uncertainties on the background estimation. Chapter 8 describes the details of the analysis, which include the selection criteria, background estimation, identification of charm jet in the final state and, limit calculation procedure. After the final optimization of selection requirements, we do not see any excess in data over the expected background. Accordingly, we set lower limits on the scalar top quark and neutralino masses after final $m_{\tilde{t}}$-dependent tweaks on topological and tagging cuts. The final results are presented in Chap. 9.

A few important terms that will be used later in this dissertation are explained below.

System of Units

Due to the small masses of elementary particles, it is not convenient to use mechanical units in the field of particle physics. The unit of energy that is most commonly used in atomic physics is called electron volt, which is the amount of energy acquired by an electron when it is accelerated through a potential difference of 1 volt. The particle momenta are measured in eV/c while the masses are measured in eV/c^2. Typical energies in particle physics are MeV(10^6eV), GeV(10^9eV) and TeV(10^{12}eV).

Two fundamental constants that enter in almost every expression in high energy physics are Planck's constant ($\hbar$) and the velocity of light in vacuum c. The numerical values of these constants are

$$\hbar = 6.5822 \times 10^{-22}\ \mathrm{MeV\ s}. \tag{1.1}$$

$$c = 2.99810^8\ \mathrm{m/s}. \tag{1.2}$$

In high energy physics, a "natural" system of units is adopted in order to conveniently handle the frequent occurrences of these constant. In this system both $\hbar$ and c are set to 1. The momenta and masses are expressed in eV and distance and time are measured in eV^{-1}. We will use this notation in this dissertation.

Cross Section and Luminosity

Cross section of a process that involves colliding and scattering of particles is a measure of the interaction between two particles. It can also be defined as the probability of the occurrence of an event, e.g. scattering, over a given area. The rate at which particles in two identical colliding beams interact can be expressed in terms of the three factors: the relative velocity of particles (v), the effective cross sectional area (σ) and the average number of particles per unit volume (ρ). This

is written as

$$R = \rho v \sigma. \tag{1.3}$$

The cross section is measured in units of barn where $1\ \mathrm{barn} = 10^{-24}\mathrm{cm}^2$. Another way of writing the Eq. 1.3 is to absorb ρv factor into one constant $\mathcal{L}$, known as the instantaneous luminosity. This is a measure of the flux of particles and is measured in units of $\mathrm{cm}^{-2}\mathrm{s}^{-1}$. The total integrated luminosity is calculated by integrating the instantaneous luminosity over a period of time and is expressed in units of inverse pico barn (pb^{-1}) or femto barn (fb^{-1}), where $1\ \mathrm{pb}^{-1} = 10^{36}\ \mathrm{cm}^{-2}$, and $1\ \mathrm{fb}^{-1} = 10^{39}\ \mathrm{cm}^{-2}$. Given the theoretical cross section for a particular process and the integrated luminosity of an experiment one can easily calculate the number of expected events of that particular process to be produced in the collisions.

Chapter 2

Theoretical Background

2.1 An Overview of Standard Model

The SM of particle physics, also known as "a low energy effective theory", was proposed by S. L. Glashow, S. Weinberg and A. Salam [1]. It describes the interactions between elementary particles and its predictions have been successfully verified by many experiments over the past several decades. The SM incorporates the strong, electromagnetic and weak interactions but does not describe the gravitational interaction. It is a Lorentz invariant renormalizable non-abelian gauge theory. The gauge group is $SU(3)_C \times SU(2)_L \times U(1)_Y$ with g_3, g and $\acute{g}$ respectively as the gauge couplings. In the expression $SU(3)_C \times SU(2)_L \times U(1)_Y$, "C" stands for the color quantum number which characterizes the strong interaction among quarks and gluons, while "L" denotes the handedness of fermions (only the left handed fermions form an SU(2) doublet in the SM) and "Y" is called the hypercharge. The hypercharge Y is related to the usual electric charge Q through the relation $Q = T_3 + \frac{Y}{2}$. Here T_3 and Y denote the eigenvalues of the appropriate generators of the $SU(2)$ and $U(1)$ gauge groups respectively.

The quarks and leptons are the matter fields in the SM while $W^{\pm}$, and Z^o bosons along with the photon constitute the gauge fields. Tables 2.1 and 2.2 show the gauge field and the particle content of the SM [2].

The SM contains three families or generations of quarks and leptons with different mass scales. In the SM left handed fermions are grouped in pairs called weak isospin doublets while the right

Gauge group	Gauge bosons	Mass
$SU(3)_C$	Gluons	0
$SU(2)_L$ and $U(1)_Y$	$W^{\mp}, Z^0$	$80 - 90$ GeV
$U(1)_{em}$	γ	0

Table 2.1: Gauge fields in the SM and their masses.

Generation	1	2	3
Quark doublets	$\begin{pmatrix} u \\ d \end{pmatrix}_L$	$\begin{pmatrix} c \\ s \end{pmatrix}_L$	$\begin{pmatrix} t \\ b \end{pmatrix}_L$
Quark singlets	u_R, d_R	c_R, s_R	t_R, b_R
Lepton doublets	$\begin{pmatrix} \upsilon_e \\ e^- \end{pmatrix}_L$	$\begin{pmatrix} \upsilon_\mu \\ \mu^- \end{pmatrix}_L$	$\begin{pmatrix} \upsilon_\tau \\ \tau^- \end{pmatrix}_L$
Lepton singlets	e_R^-	μ_R^-	τ_R^-

Table 2.2: Quarks and leptons multiplets in the SM.

handed fermions transform as singlets. As long as the $SU(2)_L \times U(1)_Y$ symmetry remains unbroken, all quarks, leptons and gauge bosons remain massless. These particles acquire mass only if electroweak symmetry is broken. The renormalizability and gauge invariance of the SM Lagrangian require $SU(2)_L \times U(1)_Y$ symmetry to be broken spontaneously. The spontaneous symmetry breaking is achieved through the Higgs mechanism and requires the introduction of a complex scalar field known as the Higgs boson. The neutral component of the Higgs field acquires a vacuum expectation value. As a result of this all fermions and gauge bosons except the photon acquire mass and the $SU(2)_L \times U(1)_Y$ gauge symmetry reduces to $U(1)\mathrm{em}$. Table 2.3 shows the masses of all the fermions that reside in the SM.

Fermion	Mass	Fermion	Mass
e	0.511 MeV	u	5 MeV
ν_e	< 50 eV	d	10 MeV
μ	105.6 MeV	c	1.5 GeV
ν_μ	< 0.5 MeV	s	100 MeV
τ	1.784 GeV	t	175 GeV
ν_τ	< 80 MeV	b	4.7 GeV

Table 2.3: Fermions in the SM and their masses.

2.2 The SM Lagrangian

The electroweak part of the SM Lagrangian can be written as a sum of four terms [3].

$$\mathcal{L}_{\text{int}} = \mathcal{L}_1 + \mathcal{L}_2 + \mathcal{L}_3 + \mathcal{L}_4. \tag{2.1}$$

The symbol $\mathcal{L}_1$ denotes the kinetic energies and self interactions of the four gauge bosons viz. $W^{\pm}$, Z_0, and γ. It is written as

$$\mathcal{L}_1 = -\frac{1}{4}\boldsymbol{W}_{\mu\nu} \cdot \boldsymbol{W}_{\mu\nu} - \frac{1}{4} B_{\mu\nu} \cdot B_{\mu\nu}, \tag{2.2}$$

where

$$B_{\mu\nu} = \partial_\mu B_\nu - \partial_\nu B_\mu, \tag{2.3}$$

$$\boldsymbol{W}_{\mu\nu} = \partial_\mu \boldsymbol{W}_\nu - \partial_\nu \boldsymbol{W}_\mu - g\boldsymbol{W}_\mu \times \boldsymbol{W}_\nu. \tag{2.4}$$

Please note that the gauge field $\mathbf{W}$ is written in bold face letter since the $SU(2)$ gauge group has three generators corresponding to a triplet of gauge fields. The $U(1)$ gauge group on the other hand has only one generator denoted as B which corresponds to a single gauge boson. The following equations reveal the connection between the charged bosons $W^{\pm}$, the neutral Z^o boson,

the photon and the previously mentioned gauge fields ($\mathbf{W}$ and B):

$$W_\mu^\pm = \frac{1}{\sqrt{2}}\left(W_\mu^1 \mp iW_\mu^2\right), \tag{2.5}$$

$$Z_\mu = -\sin\theta_W B_\mu + \cos\theta_W W_\mu^3, \tag{2.6}$$

$$A_\mu = \cos\theta_W B_\mu + \sin\theta_W W_\mu^3, \tag{2.7}$$

where θ_W is the weak mixing angle and $\frac{\acute{g}}{g} = \tan\theta_W$.

The last term in Eq. 2.4 arises due to the fact that the generators of the $SU(2)$ gauge group do not commute mutually and satisfy the following algebra:

$$[T_j, T_k] = i\,\epsilon_{jkl}T_l, \tag{2.8}$$

where each of j, k, l can have values $1-3$.

The Hermiticity and tracelessness of these generators lead to the choice of the Pauli matrices as their matrix representatives upto a normalization constant. Therefore we write $T_j = \frac{\tau_j}{2}$ where

$$\tau_1 = \begin{pmatrix} 0 & 1 \\ 1 & 0 \end{pmatrix} ;\ \tau_2 = \begin{pmatrix} 0 & -i \\ i & 0 \end{pmatrix} ;\ \tau_3 = \begin{pmatrix} 1 & 0 \\ 0 & -1 \end{pmatrix}.$$

The term $\mathcal{L}_2$ in Eq. 2.1 represents the kinetic energies of leptons and quarks and their interactions with the gauge bosons, $W^\pm, Z^0$, and γ. If we denote all left-handed fermion (quarks or leptons) doublets by L and right-handed fermion singlets by R then we can write

$$\begin{aligned}\mathcal{L}_2 &= \bar{L}\gamma^\mu\left(i\partial_\mu - g\frac{1}{2}\boldsymbol{\tau}\cdot\boldsymbol{W}_\mu - \acute{g}\frac{Y}{2}B_\mu\right)L \\ &+ \bar{R}\gamma^\mu\left(i\partial_\mu - \acute{g}\frac{Y}{2}B_\mu\right)R,\end{aligned} \tag{2.9}$$

where Y represents the hypercharge.

The $\mathcal{L}_3$ term in Eq. 2.1 contains the masses of Higgs boson (denoted as ϕ) and gauge particles, $W^\pm, Z^0$ and can be written as

$$\mathcal{L}_3 = \left|\left(i\partial_\mu - g\frac{1}{2}\boldsymbol{\tau}\cdot\boldsymbol{W}_\mu - \acute{g}\frac{Y}{2}B_\mu\right)\phi\right|^2 - V(\phi), \tag{2.10}$$

where $V(\phi)$ is given by

$$V(\phi) = \mu^2 \phi^\dagger \phi + \lambda \left(\phi^\dagger \phi\right)^2 \; ; \mu^2 < 0 \; ; \; \lambda > 0. \tag{2.11}$$

The last piece of Lagrangian $\mathcal{L}_4$, which contains the masses of leptons and quarks and their couplings to Higgs boson, can be written as

$$\mathcal{L}_4 = -\left(G_1 \bar{L} \phi R + G_2 \bar{L} \phi_c R + h.c.\right), \tag{2.12}$$

where G_1 and G_2 are Yukawa couplings of fermions to the Higgs boson. Please note that in order to write a mass term for the upper members of a fermion doublet in a gauge invariant way we need to introduce a new object $\phi_c = -i\tau_2 \phi*$ which, under the gauge group $SU(2)$, transforms in the same way as ϕ does.

Explicitly written, the masses of W and Z bosons are

$$M_W = \frac{1}{2} v g \; ; \; M_Z = \frac{1}{2} v \sqrt{g^2 + \acute{g}^2}, \tag{2.13}$$

where v is the vacuum expectation value of the Higgs boson. Using the value for Fermi coupling $G_F \sim 10^{-5}/m_N^2$, it is predicted to be 246 GeV. The masses of the fermions can in general be written as

$$m_f = h_f v, \tag{2.14}$$

where h_f is the coupling of the corresponding fermion to the Higgs boson.

The only missing part from the Lagrangian is the one that represents strong interaction. A Lagrangian which is invariant under $SU(3)_C$ can be written as

$$\mathcal{L}_{\text{QCD}} = \sum_q \bar{q} i \gamma^\mu D_\mu q - \frac{1}{4} G^a_{\mu\nu} G^{\mu\nu}_a \; ; a = 1, 2, ..., 8, \tag{2.15}$$

where q is a color triplet of a particular flavor of quark and where in first term summation is over all quark flavors.[1] The subscript QCD stands for quantum chromodynamics, the theory that

[1]This must be borne in mind that each q carries a Lorentz as well as a color index. An example term which represents the interaction of gluons with quarks may look like

$$- i g_3 \, \bar{q}_\alpha^{\, i} \, \gamma^{o \; \alpha\beta} \, T_{1_{ij}} \, G^1_o \, q^j_\beta, \tag{2.16}$$

where $i = 1, 2, 3$ is a color index and represents red, green and blue colors of a quark. For simplicity only first term in summation over μ and a is considered.

describes the strong interactions between quarks. The gluon field strength tensor is given by

$$G^a_{\mu\nu} = \partial_\mu G^a_\nu - \partial_\nu G^a_\mu - g_3 f_{abc} G^b_\mu G^c_\nu, \tag{2.17}$$

and the covariant derivative is

$$D_\mu = \partial_\mu + i g_3 T_a G^a_\mu, \tag{2.18}$$

where T_a are eight generators of the $SU(3)$ gauge group whose matrix representatives satisfy the following commutation relations.

$$[T_a, T_b] = i f_{abc} T_c. \tag{2.19}$$

The local gauge invariance requires the gluons to be massless. This explains why there is no mass term for the gluons in Eq. 2.15.

2.2.1 Fundamentality of the SM

The predictions of the SM have been tested in numerous experiments that have been carried out over the last few decades. With the exception of the neutrino sector no significant deviations from the predictions of the SM have been observed. The phenomenon of neutrino oscillations [4] establishes the presence of a non zero neutrino mass in contradiction with the SM which assumes neutrinos to be massless. The successes of the SM include [1]

- renormalizability.
- suppression of flavor changing neutral currents (GIM Mechanism).
- prediction of the existence of CP violation.
- conservation of lepton and baryon numbers without imposing any additional symmetry requirement.

Despite its numerous successes there remain many unanswered questions whose answers cannot be found within the SM. For example if one looks at Table 2.3 one notices the considerable differences between the masses of different fermions? The following section presents a few more reasons to look for physics beyond the SM.

2.2.2 Physics Beyond the SM

The mass "hierarchy" problem is one of the motivations in the search for physics beyond the SM. In the SM, the scale of the electroweak symmetry breaking is of the order of $M_W \sim 10^2$ GeV. In other words this means that electromagnetic and weak force are combined into one force at an energy scale which is approximately 10^2 GeV. This mass scale derives from the vacuum expectation value of the Higgs boson. It has been shown that when one attempts to combine the strong force with the electroweak force into a grand unified theory (GUT), the unification scale M_X turns out to be at least fourteen orders of magnitude higher than the electroweak scale. This leaves us with a mystery as to why the ratio M_W/M_X is so small. The technical aspect of the hierarchy problem is to keep this ratio stable in higher orders of perturbation theory without requiring an enormous amount of "fine tuning".

A second motivation behind looking for physics beyond the SM is the "mass problem". All fermions in the SM are chiral which means that the left and right handed fields transform differently under the gauge transformation. This prohibits us from writing any arbitrary mass term of the form $m_f\bar{\psi}\psi$ for fermions. This in turn implies that the fermions in the SM cannot acquire any arbitrary mass. The fermion masses depend on their couplings to the Higgs boson and are thus protected by the chiral symmetry.

A gauge boson within the SM remains massless as long as the gauge symmetry remains an exact symmetry. It can acquire mass only when the corresponding generator of the gauge group is "broken". This means that the particular generator doesn't leave the vacuum invariant. We therefore say that the masses of the gauge bosons are protected by the gauge symmetry [5, 6, 7].

On the other hand there is no symmetry in the context of the SM that prevents scalars (Higgs boson in this case) from acquiring any arbitrary massso that their masses cannot be made small, "naturally". An example is shown in Fig. 2.1 where a fermion anti-fermion pair (e.g top quark) contributes to the two-point function of the SM Higgs field [5]. Mathematically this correction

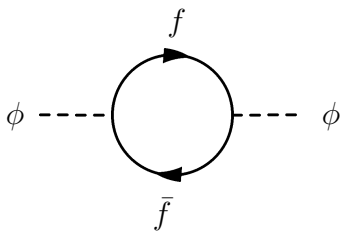

Figure 2.1: Radiative correction to the Higgs mass through the fermion loop.

can be written as

$$-2N(f)\lambda_f^2 \int \frac{d^4k}{(2\pi)^4} \left[\frac{1}{k^2 - m_f^2} + \frac{2m_f^2}{\left(k^2 - m_f^2\right)^2} \right], \tag{2.20}$$

where $N(f)$ is the color factor for fermion, λ_f is the strength with which Higgs boson couples to the fermions, m_f is the mass of the fermion and k is the momentum running in the loop . A simple dimensional analysis reveals that the first term in Eq. 2.20 is quadratically divergent.

If we take the momentum cutoff to be the scale at which the electromagnetic, weak and the strong forces unify into one force (10^{16} GeV), the correction to the Higgs mass will be at least 30 orders of magnitude larger than the physical mass of Higgs boson. The mass of the Higgs boson is assumed to be less than 1 TeV. This may not allow the Higgs mechanism to work in the SM where we need the electroweak symmetry breaking scale to be around 10^2 GeV. This fact provides a solid reason to look for a possible extension of the symmetry, that SM has, to prevent scalars from acquiring any arbitrary masses.

These are only a few motivations to search for physics beyond the SM. There may be many others such as, how does the mixing between different quark flavors arise, what, if any, is the pattern of lepton flavor mixing, what is the mechanism of CP violation? Next section presents an overview of how supersymmetry can answer a few of these questions.

2.3 Supersymmetry

2.3.1 What is Supersymmetry

Supersymmetry (SUSY) is a hypothetical symmetry of the basic laws of nature. It proposes that the laws of nature are symmetric provided bosons and fermions are interchanged in an appropriate manner [8]. The generators of SUSY transformation convert a bosonic state into a fermionic one and vice versa. For instance such a transformation will conver photon which is a spin one boson into a spin one particle known as photino and vice versa. Similarly it may convert an electron, which is a spin one half fermion, into a spin zero partcile known the selectron. Thus if Q denotes a generator of a SUSY transformation one may write

$$Q|\texttt{boson}\rangle = |\texttt{fermion}\rangle \; ; \; Q|\texttt{fermion}\rangle = |\texttt{boson}\rangle$$

2.3.2 Why do we need Supersymmetry

As discussed in Sec. 2.2.2, there is no symmetry within the SM that can prevent scalars from acquiring very large masses. If we couple a theory of scalar particles to some new physics at an arbitrary scale Λ, the quantum corrections to the scalar squared-mass, due to the quadratic divergences in the scalar self energy, are $O(\Lambda^2)$. If Higgs boson is a fundamental scalar we have two choices:

- Either we make this assumption that there do not exist any heavy particles that couple to Higgs scalar field.
- Or we can somehow cancel the various contributions to m_H^2.

The systematic cancellation of divergent contributions is achieved by introducing a new symmetry between fermions and bosons, called "Supersymmetry". As a consequence, as long as SUSY is a good symmetry, scalar masses enjoy the same chiral protection as fermions. Furthermore the quadratically divergent contributions to the Higgs boson mass, mentioned in Sec. 2.2.2, also cancel out as each fermion in the SM has a scalar partner with same quantum numbers except spin.

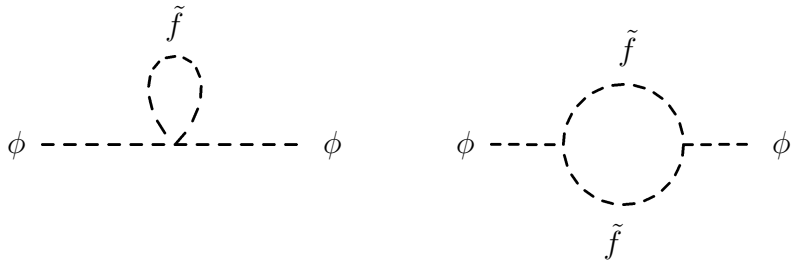

Figure 2.2: Scalar fermion loop corrections to Higgs mass.

This means in addition to the contribution shown in Fig. 2.1 there will be additional contributions as shown in Fig. 2.2.

The combined contribution to the Higgs boson mass from Fig. 2.2 can be written as [5]

$$\begin{aligned}
&-N(\tilde{f})\tilde{\lambda}_f \int \frac{d^4k}{(2\pi)^4}\left[\frac{1}{k^2-m^2_{\tilde{f}_L}}+\frac{1}{k^2-m^2_{\tilde{f}_R}}\right] \\
&+N(\tilde{f})\left(\tilde{\lambda}_f v\right)^2 \int \frac{d^4k}{(2\pi)^4}\left[\frac{1}{\left(k^2-m^2_{\tilde{f}_L}\right)^2}+\frac{1}{\left(k^2-m^2_{\tilde{f}_R}\right)^2}\right] \\
&+|\lambda_f A_f|\, N(\tilde{f}) \int \frac{d^4k}{(2\pi)^4}\frac{1}{\left(k^2-m^2_{\tilde{f}_L}\right)\left(k^2-m^2_{\tilde{f}_R}\right)},
\end{aligned} \tag{2.21}$$

where $N(\tilde{f})$ is the color factor for scalar partner of the fermion, $m_{\tilde{f}}$ and $\tilde{\lambda}_f$ are its mass and coupling to Higgs boson, respectively. Only the first term in Eq. 2.21 is quadratically divergent. Comparing it with the fermionic contribution, given in Eq. 2.20, one notices that the quadratic contributions can be canceled if we choose

$$\begin{aligned}
N(\tilde{f}_L) &= N(\tilde{f}_R) = N(f), \\
\tilde{\lambda}_f &= -\lambda_f^2,
\end{aligned} \tag{2.22}$$

and a complete cancellation between fermionic and bosonic contributions can be obtained if in addition to Eqs. 2.22 we require

$$\begin{aligned}
m_{\tilde{f}} &= m_f, \\
A_f &= 0.
\end{aligned} \tag{2.23}$$

Thus by introducing a symmetry between the fermions and bosons within the SM, the problem of divergent contributions to the Higgs boson mass can be overcome.

The unification of the coupling constants is another motivation to have SUSY. We know that the coupling constants depend on the energy at which the interactions are probed. Following the work of Georgi, Glashow, Pati and Salam it was predicted that the coupling constants for electromagnetic, weak and strong forces should meet at an energy scale $>> M_W$. This is not however the case unless additional particles are introduced, which is what SUSY provides. This is shown in Fig. 2.3 where $\alpha_1, \alpha_2, \alpha_3$ are electromagnetic, weak and strong coupling constants respectively. Their values at the energy scale equal to M_Z, determined from a fit to the LEP and the Tevatron data are [9]

$$\alpha_1(M_Z) = 0.017,\ \alpha_2(M_Z) = 0.034,\ \alpha_3(M_Z) = 0.0118. \tag{2.24}$$

It is evident from the right hand plot in Fig. 2.3 that the particle spectrum of SUSY gives a better

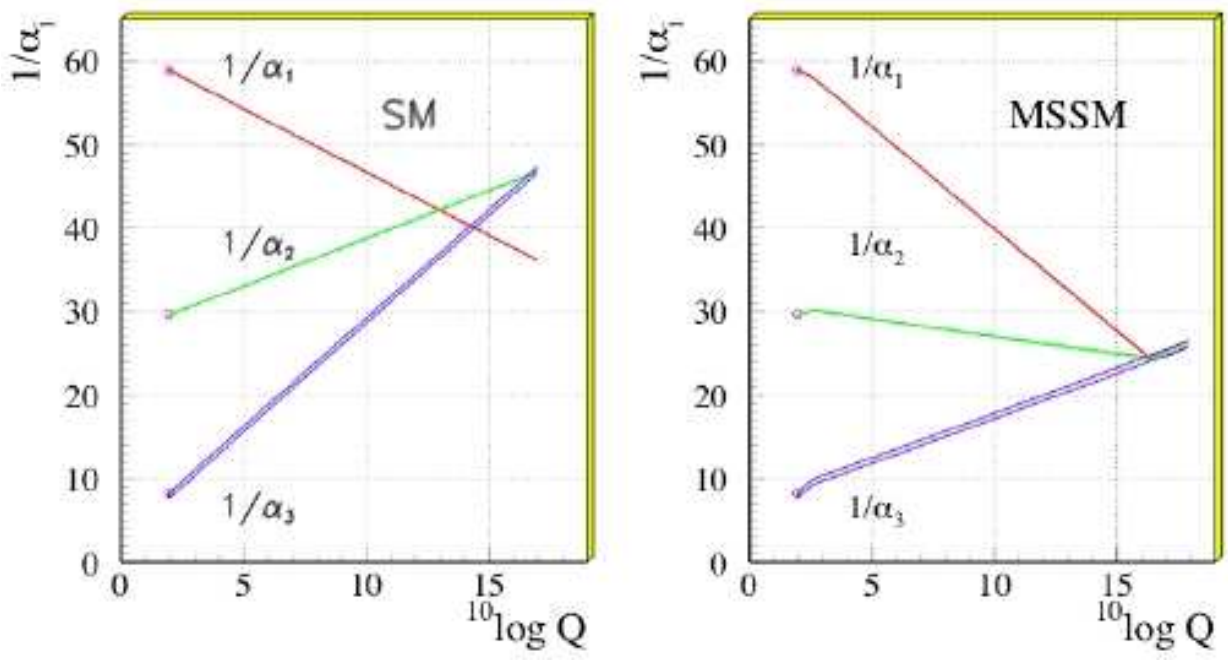

Figure 2.3: Evolution of the coupling constants in SM (left) and MSSM (right).

unification of the coupling constants than the one in the SM.

2.4 Formulation of SUSY Algebra

Since the supersymmetric transformations combine space-time symmetry with the internal spin symmetry, a review of Poincare algebra is presented here. A Poincare transformation is a proper Lorentz transformation followed by a translation in space. The generators of the Poincare group consist of six generators, $M_{\mu\nu}$, that represent Lorentz group, and four generators P^{λ}, that represent translations in space [8, 10]. Out of six generators $M_{\mu\nu}$, three represent rotations and three represent boosts. Following relations define the algebra of these generators.

$$[P^{\mu}, P^{\nu}] = 0, \tag{2.25}$$

$$\left[M^{\mu\nu}, P^{\lambda}\right] = i\left(g^{\nu\lambda}P^{\mu} - g^{\mu\lambda}P^{\nu}\right), \tag{2.26}$$

$$[M^{\mu\nu}, M^{\rho\sigma}] = i\left(g^{\nu\rho}M^{\mu\sigma} + g^{\mu\sigma}M^{\nu\rho} - g^{\mu\rho}M^{\nu\sigma} - g^{\nu\sigma}M^{\mu\rho}\right), \tag{2.27}$$

where $g^{\mu\nu}$ is the space-time metric tensor with

$$g^{00} = 1 \; ; \; g^{11} = g^{22} = g^{33} = -1, \tag{2.28}$$

while all other elements are zero.

As discusses in Sec. 2.3.1 a supersymmetric transformation changes the spin of the particle involved, implying that the generators of the supersymmetric transformation carry spin. This tells that the algebra of the SUSY generators will involve not only commutators but anti-commutators as well.

The generators of supersymmetric transformations, denoted by Q_{α}, satisfy the following commutation relations.

$$\{Q_{\alpha}, Q_{\beta}\} = 0 = \{\bar{Q}_{\dot{\alpha}}, \bar{Q}_{\dot{\beta}}\}, \tag{2.29}$$

$$\left[P^{\lambda}, Q_{\alpha}\right] = 0 = \left[P^{\lambda}, \bar{Q}_{\dot{\alpha}}\right], \tag{2.30}$$

$$[M^{\mu\nu}, Q_{\alpha}] = -i(\sigma^{\mu\nu})_{\alpha}^{\ \beta}Q_{\beta}, \tag{2.31}$$

$$\left[M^{\mu\nu}, \bar{Q}^{\dot{\alpha}}\right] = -i(\bar{\sigma}^{\mu\nu})^{\dot{\alpha}}_{\ \dot{\beta}}\bar{Q}^{\dot{\beta}}, \tag{2.32}$$

$$\{Q_{\alpha}, \bar{Q}_{\dot{\alpha}}\} = 2(\sigma_{\alpha\dot{\alpha}})^{\mu}P_{\mu}, \tag{2.33}$$

Field	Mass Dimension
ϕ	1
ψ	$\frac{3}{2}$
F, D	2

Table 2.4: Scalar, spinor and auxiliary fields and their mass dimensions.

where σ^μ are the Pauli spin matrices, and $\alpha, \beta, \dot{\alpha}, \dot{\beta}$ are the spinor indices that can have values $1, 2$. The generator of the supersymmetric transformation for left handed spinor is, by convention, denoted as Q_α while that for right handed spinor is denoted as $\bar{Q}_{\dot{\alpha}}$.

2.4.1 Representation of SUSY Algebra

The single particle states of a supersymmetric theory fall naturally into the irreducible representations of supersymmetry algebra which are called supermultiplets. Each supermultiplet contains both fermionic and bosonic states which are commonly known as superpartners of each other. A simplest chiral supermultiplet is given as [8, 10, 11]

$$\Phi \equiv (\phi, \psi_\alpha, F), \tag{2.34}$$

where ϕ is a complex scalar, ψ_α is a two component Weyl spinor, and F is a complex scalar auxiliary field. The field F does not propagate and can be eliminated using its equation of motion. A supersymmetric transformation will rotate the components of a supermultiplet into each other. The infinitesimal supersymmetric transformations for components of a supermultiplet are

$$\delta_\xi \, \phi = \sqrt{2} \, \xi \, \psi, \tag{2.35}$$

$$\delta_\xi \, \psi = i\sqrt{2} \, \sigma^\mu \, \bar{\xi} \, \partial_\mu \, \phi + \sqrt{2} \, \xi \, F, \tag{2.36}$$

$$\delta_\xi \, F = i\sqrt{2}\bar{\xi} \, \bar{\sigma^\mu} \, \partial_\mu \, \psi, \tag{2.37}$$

where ξ is an anti-commuting Grassmann variable. Some important points to be noted are:

- Each supermultiplet contains an equal number of fermionic and bosonic degrees of freedom.

- The $(mass)^2$ operator, $P^2 = P_\mu P^\mu$ commutes with all the generators of supersymmetric transformation, so the particles which inhabit the same irreducible supermultiplet must have equal masses.

- The component of the chiral supermultiplet with highest mass dimensions always transforms as a total divergence where the mass dimensions of all fields are shown in Table 2.4.

- It is clear from the relation in Eq. 2.33 that the energy P_0 in supersymmetric theories is always positive as shown in the equation below.

$$P_0 = \frac{1}{4}\left[Q_1\bar{Q}_1 + \bar{Q}_1 Q_1 + Q_2\bar{Q}_2 + \bar{Q}_2 Q_2\right] \geq 0. \tag{2.38}$$

This formalism of the representation of SUSY algebra is known as the off-shell formalism.
A different approach of constructing the representation of supersymmetry algebra, in which supersymmetry is manifest like Lorentz invariance is the superspace formalism introduced by Salam and Strathdee [12]. In this formalism, one extends the Minkowski space to superspace. The elements of the superspace are called super coordinates which consists of space-time coordinates x^μ and four anti-commuting Grassmann numbers. In terms of two component Weyl spinor formalism, latter are θ_α and $\bar{\theta}_{\dot{\alpha}}$, and are considered to be independent. The most general superfield which is a function of super coordinates can be written as a Taylor expansion in θ and $\bar{\theta}$ and is given by

$$\begin{aligned} S(x,\theta,\bar{\theta}) \;=\; & f(x) + \theta\eta(x) + \bar{\theta}\,\bar{\chi}(x) + \theta\theta\, m(x) + \bar{\theta}\bar{\theta}n(x) + \theta\sigma^\mu\bar{\theta}\mathrm{v}_\mu(x) + \\ & \theta\theta\bar{\theta}\bar{\lambda}(x) + \bar{\theta}\bar{\theta}\theta\psi(x) + \theta\theta\bar{\theta}\bar{\theta}\, d(x), \end{aligned} \tag{2.39}$$

where each of $\eta, \chi, \lambda, \psi$ is a 2-component Weyl spinor, v_μ is a vector and f and d are scalars.

2.4.2 Chiral, Anti-Chiral, and Vector Superfields

The general superfield discussed in Sec. 2.4.1 is a reducible representation of the super algebra. In order to find the irreducible representation, additional constraints are imposed on the most general

superfields. First the covariant derivative D_α and $\bar{D}_{\dot{\alpha}}$ are defined as

$$D_\alpha \equiv \partial_\alpha + i(\sigma_{\alpha\dot{\alpha}})^\mu \bar{\theta}^{\dot{\alpha}} \partial_\mu, \tag{2.40}$$

$$\bar{D}_{\dot{\alpha}} \equiv -\bar{\partial}_{\dot{\alpha}} - i\theta^\alpha (\sigma_{\alpha\dot{\alpha}})^\mu \partial_\mu. \tag{2.41}$$

A chiral superfield is obtained from general superfield and satisfies the constraint $\bar{D}_{\dot{\alpha}}\, S = 0$. In component form it can be written as[2]

$$\Phi = \phi(x) + \sqrt{2}\theta\psi(x) + \theta\theta F, \tag{2.42}$$

where ϕ and F are complex scalar fields and ψ is a left handed Weyl spinor field.

Similarly an anti-chiral superfield is the one that satisfies the constraint $D_\alpha\, S^\dagger = 0$ and can be written as

$$\Phi^\dagger = \phi^*(x) + \sqrt{2}\bar{\theta}\bar{\psi}(x) + \bar{\theta}\bar{\theta}F^*. \tag{2.43}$$

A vector superfield V satisfies the constraint $V^\dagger(x, \theta, \bar{\theta}\ ) = V(x, \theta, \bar{\theta})$. In Wess-Zumino gauge, vector superfield is given by

$$V(x, \theta, \bar{\theta}) = -\theta\sigma^\mu\bar{\theta}\mathrm{v}_\mu(x) + i\theta\theta\bar{\theta}\bar{\lambda}(x) - i\bar{\theta}\bar{\theta}\theta\lambda(x). + \frac{1}{2}\theta\theta\bar{\theta}\bar{\theta}\, D(x) \tag{2.44}$$

Chiral and anti-chiral superfields contain spin 0, spin $\frac{1}{2}$ fields and an auxiliary scalar field F. A vector superfield contains a spin one field which is the gauge boson and its super partner called gaugino (spin $\frac{1}{2}$), along with an auxiliary field D.

2.5 Supersymmetric Interactions

In order to be able to describe supersymmetric interactions we need to construct a Lagrangian which is invariant under supersymmetric transformation. The most general renormalizable, supersymmetric Lagrangian is constructed from superfields defined in Sec. 2.4.2 [7]. If Φ is a chiral superfield then one can write the Lagrangian density as

$$L = \Phi_i^\dagger \Phi_i \Big|_{\theta\theta\bar{\theta}\bar{\theta}} + \left[k_i\Phi_i + \frac{1}{2}m_{ij}\Phi_i\Phi_j + \frac{1}{3}g_{ijk}\Phi_i\Phi_j\Phi_k\right]\Big|_{\theta\theta}, \tag{2.45}$$

[2]The spinor indices have been suppressed.

where m_{ij} and g_{ijk} are symmetric matrices and Φ_i are all left chiral fields. It can be shown from simple power counting that the term which is a product of more than three superfields will have mass dimensions five, giving rise to a possibility of a coupling constant with negative mass dimensions in front of it. This will destroy the renormalizability of the theory. The mass dimensions of the fields are given in Table 2.4 while the anti-commuting Grassmann variable θ and the vector field have mass dimensions $-\frac{1}{2}$ and 1 respectively. The term $\Phi_i^\dagger \Phi_i$ in Eq. 2.45 gives the kinetic energy terms for the scalar and spinor fields while the combination

$$W = \frac{1}{2} m_{ij} \Phi_i \Phi_j + \frac{1}{3} g_{ijk} \Phi_i \Phi_j \Phi_k, \tag{2.46}$$

is known as superpotential. In terms of the component fields, L can be written as

$$L = \partial_\mu \phi_i^\dagger \partial_\mu \phi_i - i\bar{\psi}_i \bar{\sigma}^\mu \partial_\mu \psi_i - |m_{ij}\phi_j + \lambda_{ijk}\phi_j\phi_k|^2 - \left(\frac{1}{2} m_{ij}\psi_i\psi_j + \lambda_{ijk}\psi_i\psi_j\phi_k + h.c.\right) \tag{2.47}$$

Up to this point the Lagrangian for supersymmetric theory describes the kinematics of scalar and spinor fields and interactions between them. However all the quarks, leptons, squarks and sleptons participate in gauge theories which involve vector gauge bosons. Squarks and sleptons are the supersymmetric partners of the quarks and leptons respectively. In order to accommodate the interactions between gauge and matter particles, additional terms need to be added to L. This is done by introducing vector superfields which contain a vector gauge boson A_ν^a, its superpartner gaugino λ^a and an auxiliary filed D^a. In the simplest form one can write

$$L_{\text{gauge}} = -\frac{1}{4} F_{\mu\nu}^a F^{\mu\nu a} - i\bar{\lambda}^a \bar{\sigma}^\mu D_\mu \lambda^a + \frac{1}{2} D^a D^a, \tag{2.48}$$

where

$$F_{\mu\nu}^a = \partial_\mu A_\nu^a - \partial_\nu A_\mu^a - g f^{abc} A_\mu^b A_\nu^c, \tag{2.49}$$

is the field strength tensor and

$$D_\mu \lambda^a = \partial_\mu \lambda^a - g f^{abc} A_\mu^b \lambda^c, \tag{2.50}$$

is the covariant derivative of the gaugino field. The index a runs over the adjoint representation of the gauge group[3] and f_{abc} are the structure constants for any particular gauge group.

[3] As an example $a = 1, .., 8$ for $SU(3)_C$ color gluons and gluinos; $a = 1, 2, 3$ for $SU(2)_L$ weak isospin gauge bosons W, Z; and $a = 1$ for $U(1)_Y$ weak hypercharge gauge boson.

Superfield	Spin $\frac{1}{2}$	Spin 1	$SU(3)_c, SU(2)_L, U(1)_Y$
gluino, gluon	$\tilde{g}$	g	$(\mathbf{8}, \mathbf{1}, 0)$
winos, W bosons	$\tilde{W}^{\pm}\ \tilde{W}^0$	$W^{\pm}\ W^0$	$(\mathbf{1}, \mathbf{3}, 0)$
bino, B bosons	$\tilde{B}^0$	B^0	$(\mathbf{1}, \mathbf{1}, 0)$

Table 2.5: Gauge supermultiplets in the MSSM.

2.6 Minimal Supersymmetric Standard Model

The minimal supersymmetric standard model (MSSM) is the minimal supersymmetric extension of the SM. Each SM particle is assigned one supersymmetric partner with identical quantum numbers except spin different by half a unit. The symbols for the squarks and sleptons are the same as for the corresponding fermions, but with a tilde drawn on top of them. The spin $1/2$ partners of the gauge bosons are called gauginos. In order to give masses to up and down type quarks and to cancel gauge anomalies caused by fermion loops, two complex Higgs doublets are introduced. The gauge and chiral supermultiplets in Tables. 2.5 and 2.6 make up the content of the MSSM.

2.6.1 The Superpotential and Supersymmetric Interactions in the MSSM

Having found the particle content for the MSSM, next step is to write the superpotential for the MSSM. This can be written as [7]

$$W_{\text{MSSM}} = \bar{u} y_u Q H_u - \bar{d} y_d Q H_d - \bar{e} y_e L H_d + \mu H_u H_d. \tag{2.51}$$

The objects $H_u, H_d, Q, L, \bar{u}, \bar{d}, \bar{e}$ are chiral superfields corresponding to the chiral supermultiplet[4] in Table 2.6. The dimensionless Yukawa coupling parameters y_u, y_d, y_e are 3×3 matrices in family space. Explicitly showing all family, color, and $SU(2)_L$ weak isospin indices, one can write the first term as

$$\bar{u}_a{}^i (y_u)_i{}^j Q^a_{j\alpha} (H_u)_\beta \epsilon^{\alpha\beta},$$

[4]The label u stands for all up-type quarks and d for down-type quarks.

Superfield		Spin 0	Spin $\frac{1}{2}$	$SU(3)_c, SU(2)_L, U(1)_Y$
squarks, quarks ($\times$ 3 families)	Q $\bar{u}$ $\bar{d}$	$(\tilde{u}_L\ \tilde{d}_L)$ $\tilde{u}^*_R$ $\tilde{d}^*_R$	$(u_L\ d_L)$ $u^\dagger_R$ $d^\dagger_R$	(**3**, **2**, $\frac{1}{6}$) ($\bar{\mathbf{3}}$, **1**, -$\frac{2}{3}$) ($\bar{\mathbf{3}}$, **1**, $\frac{1}{3}$)
sleptons, leptons ($\times$ 3 families)	L $\bar{e}$	$(\tilde{\nu}\ \tilde{e}_L)$ $\tilde{e}^*_R$	($\nu\ e_L$) $e^\dagger_R$	(**1**, **2**, - $\frac{1}{2}$) (**1**, **1**, 1)
Higgs, Higgsinos	H_u H_d	$(H^+_u\ H^0_u)$ $(H^0_d\ H^-_d)$	$(\tilde{H}^+_u\ \tilde{H}^0_u)$ $(\tilde{H}^0_d\ \tilde{H}^-_d)$	(**1**, **2**, + $\frac{1}{2}$) (**1**, **2**, - $\frac{1}{2}$)

Table 2.6: Chiral supermultiplets in the MSSM.

where $i = 1, 2, 3$ is a family index, $a = 1, 2, 3$ is a color index, and $\epsilon^{\alpha\beta}$ an antisymmetric tensor with $\epsilon_{12} = -\epsilon_{21} = 1$ is used to tie together $SU(2)_L$ weak isospin indices in a gauge invariant way. The μ term is the supersymmetric version of the Higgs mass in the SM.

After the neutral components of H_u and H_d acquire vacuum expectation values, the Yukawa matrices determine the masses and CKM mixing angles of quarks and leptons. For simplicity it is safe to assume that only the third family components of each Yukawa coupling matrix are important as top quark, bottom quark and tau lepton are the heavy fermions in the SM. Thus

$$\mathbf{y_u} \approx \begin{pmatrix} 0 & 0 & 0 \\ 0 & 0 & 0 \\ 0 & 0 & y_t \end{pmatrix} \ ; \ \mathbf{y_d} \approx \begin{pmatrix} 0 & 0 & 0 \\ 0 & 0 & 0 \\ 0 & 0 & y_b \end{pmatrix} \ ; \ \mathbf{y_e} \approx \begin{pmatrix} 0 & 0 & 0 \\ 0 & 0 & 0 \\ 0 & 0 & y_\tau \end{pmatrix}.$$

The detailed interaction terms for the third family of quarks will be

$$y_t(\bar{t}tH^0_u - \bar{t}bH^+_u) - y_b(\bar{b}tH^-_d - \bar{b}bH^0_d).$$

In the supersymmetric version of the SM potential, we can find not only Higgs-quark-quark and Higgs-lepton-lepton couplings, but also squark-Higgsino-quark and slepton-Higgsino-lepton in-

teractions. There are also scalar quartic interactions. The couplings of the SM gauge bosons (photon, $W^{\pm}$, Z^0 and gluons) to the MSSM particles are determined completely by the gauge invariance of the kinetic terms in the Lagrangian.

The mass terms for Higgs bosons and its superpartner are

$$-\mu \left(\tilde{H}_u^+ \tilde{H}_d^- - \tilde{H}_u^0 \tilde{H}_d^0 \right),$$

and

$$|\mu|^2 \left(|H_u^0|^2 + |H_u^+|^2 + |H_d^0|^2 + |H_d^-|^2 \right).$$

Since the mass term for Higgs boson is positive definite, we will need additional terms in order to accommodate SUSY and in turn electroweak symmetry breaking.

The cubic terms for scalar fields which play an important role in determining the mixing of top squarks, bottom squarks and tau sleptons, arise from a combination of μ-term and Yukawa couplings and can be written as

$$\mu^* \left(\tilde{\bar{u}} \mathbf{y_u} \tilde{u} H_d^{0*} + \tilde{\bar{d}} \mathbf{y_d} \tilde{d} H_u^{0*} + \tilde{\bar{e}} \mathbf{y_e} \tilde{e} H_u^{0*} + \tilde{\bar{u}} \mathbf{y_u} \tilde{d} H_d^{-*} + \tilde{\bar{d}} \mathbf{y_d} \tilde{u} H_u^{+*} + \tilde{\bar{e}} \mathbf{y_e} \tilde{\nu} H_u^{+*} \right). \tag{2.52}$$

This completes the information that we will need in order to write the mass matrix for scalar top quark, which is presented in Chap. 3.

2.6.2 R-Parity

The supersymmetric potential shown in Eq. 2.51 is the most general one that can be written using the chiral superfileds. However one can add following terms to it [7]

$$\frac{1}{2} \lambda^{ijk} L_i L_j \bar{e}_k + \acute{\lambda}^{ijk} L_i Q_j \bar{d}_k + \acute{\mu}^i L_i H_u \; ; \; \Delta L \neq 0, \tag{2.53}$$

and

$$\acute{\lambda}^{ijk} \bar{u}_i \bar{d}_j \bar{d}_k \; ; \; \Delta B \neq 0, \tag{2.54}$$

where i, j, k are the family indices and L and Q are the supermultiplets representing leptons and quarks. The baryon and lepton number assignment for different fields are given in Table 2.7.

Superfield	Baryon Number	Lepton Number
Q_i	$\frac{1}{3}$	0
$\bar{u}_i, \bar{d}_i$	$-\frac{1}{3}$	0
L_i	0	1
$\bar{e}_i$	0	-1

Table 2.7: Baryon and lepton number assignment for chiral superfields.

All of these terms are gauge invariant and analytic in chiral superfields. The terms in first line violate the conservation of lepton number ($\Delta L \neq 0$) while the terms in second line violate baryon number conservation ($\Delta B \neq 0$). One unpleasant aspect of having these terms is the outcome of very short lifetime of proton through the presence of scalar quarks as mediators.

In order to avoid the existence of such terms in MSSM a new symmetry is introduced which is known as "R-parity". For a particle with baryon number B and lepton number L, R-parity is defined as

$$P_R = (-1)^{3(B-L)+2s}. \tag{2.55}$$

It is a multiplicative quantum number which should be conserved in each term written in superpotential. All SM particles have even $(+1)$ R-parity while their superpartners have odd (-1) R-parity. The important phenomenological consequences of requiring R-parity conservation are

- The lightest supersymmetric particle (LSP) with $P_R = -1$ is stable. Here $\tilde{\chi}_1^0$, a mass eigenstates resulting from the mixing of the SUSY partners of the neutral gauge and Higgs bosons, is taken to be the LSP.

- Each supersymmetric particle other than the LSP will eventually decay into a state which contains an odd number of LSPs.

- In collider experiments, supersymmetric particles will be produced in pairs.

The analysis presented in this thesis assumes R-parity conservation.

2.6.3 Soft SUSY Breaking in MSSM

The MSSM Lagrangian constructed so far fulfills the criteria that the masses of ordinary SM particles and their superpartners are identical. In the real world, no experiment has yet discovered a spin zero partner of electron with the same mass. This is true for other particles as well. For this reason SUSY is thought to be a broken symmetry of the nature. It is not straightforward to break supersymmetry spontaneously.

As is evident from Eq. (2.38) that the energy in the supersymmetric theory is always positive definite, the minimum value of energy being zero. Supersymmetry breaking is therefore achieved by adding the "soft breaking" terms to the Lagrangian. The terms are called soft because they do not reintroduce the quadratic divergences that SUSY has eliminated. The most general SUSY breaking terms are [7]

$$
\begin{aligned}
L_{\text{soft}}^{\text{MSSM}} = & - \frac{1}{2}(M_3\tilde{g}\tilde{g} + M_2\tilde{W}\tilde{W} + M_1\tilde{B}\tilde{B}) + c.c. && (2.56)\\
& - (\tilde{\bar{u}}\mathtt{a_u}\tilde{Q}H_u - \tilde{\bar{d}}\mathtt{a_d}\tilde{Q}H_d - \tilde{\bar{e}}\mathtt{a_e}\tilde{L}H_d) + c.c.\\
& - \tilde{Q}^\dagger\mathbf{m_Q^2}\tilde{Q} - \tilde{L}^\dagger\mathbf{m_L^2}\tilde{L} - \tilde{\bar{u}}\mathbf{m_{\bar{u}}^2}\tilde{\bar{u}}^\dagger - \tilde{\bar{d}}\mathbf{m_{\bar{d}}^2}\tilde{\bar{d}}^\dagger - \tilde{\bar{e}}\mathbf{m_{\bar{e}}^2}\tilde{\bar{e}}^\dagger\\
& - m_{H_u}^2 H_u^* H_u - m_{H_d}^2 H_d^* H_d - (bH_uH_d + c.c.) && (2.57)
\end{aligned}
$$

In the above equation M_3, M_2, M_1 are the gluino, wino and bino mass terms. Each of $\mathtt{a_u}$, $\mathtt{a_d}$, $\mathtt{a_e}$, $\mathbf{m_Q^2}$, $\mathbf{m_{\bar{u}}^2}$, $\mathbf{m_{\bar{d}}^2}$, $\mathbf{m_L^2}$, $\mathbf{m_{\bar{e}}^2}$ is a 3×3 matrix in family space. Squark and slepton mass terms are of the type $(m^2)_i^j$. The supersymmetry breaking part of the Lagrangian introduces more than hundred unknown real constants.

This completes the definition of the MSSM. With the help of Lagrangian and soft SUSY breaking terms one can describe all kind of interactions between the SM particles and their superpartners.

2.7 Summary

The SM can describe electromagnetic, weak and strong interactions among the elementary particles of nature. It does not accommodate gravitational interactions. Its predictions have been tested and verified by several high energy experiments. There remain a few compelling questions that

motivate to search for SUSY as a possible extension of the symmetry that SM already exhibits. SUSY provides a solution for the cancellation of quadratic divergences and also helps to achieve a better unification of strong, electromagnetic and weak interactions.

Chapter 3

The Scalar Top Quark

The scalar top quark ($\tilde{t}$) is the superpartner of the heaviest quark in the SM - the top quark. In this chapter after briefly describing the facts that can make us believe that $\tilde{t}$ can be the lightest of all squarks within the MSSM, its production and decay modes are discussed. At the end of the chapter an overview of the current status of experimental searches for $\tilde{t}$ is presented.

3.1 A Light $\tilde{t}$

3.1.1 $\tilde{t}$ Mass Matrix

From the superpotential in the MSSM, the soft SUSY breaking terms and the part of the Lagrangian that describes gauge interaction as given in Eqs. 2.51, 2.48, 2.57, five contributions to $\tilde{t}$ mass matrix arise [5]. Each of these is briefly discussed below.

The first contribution to the diagonal mass term comes from the interaction of $\tilde{t}$ quark with Higgs field and can be written as [7, 13, 14]

$$\tilde{t}_L : y_t(H_u^0 \tilde{t}_L^* \tilde{t}_L) = \left(\frac{y_t v_2}{\sqrt{2}}\right)^2 = m_t^2, \tag{3.1}$$

$$\tilde{t}_R : y_t(H_u^0 \tilde{t}_R^* \tilde{t}_R) = \left(\frac{y_t v_2}{\sqrt{2}}\right)^2 = m_t^2, \tag{3.2}$$

where v_2 is the vacuum expectation value of H_u^0 and y_t is the top quark Yukawa coupling.

Other contributions to the diagonal mass term arise from the soft SUSY breaking mass terms and are given by $m_{\tilde{t}_L}^2$ and $m_{\tilde{t}_R}^2$ for left and right handed $\tilde{t}$ quarks respectively. A third diagonal

contribution to the mass matrix comes from the terms that are cubic in the scalar field, which arise from the gauge interaction part of the Lagrangian. These can be written as

$$\frac{1}{2}g_a^2\left(\bar{\phi}_i T_{ij}^a \phi_j\right)^2, \tag{3.3}$$

where for the $SU(2)$ gauge group, a runs from $1-3$, and T_{ij} can be expressed in terms of Pauli spin matrices. As for the $SU(2)$ gauge group, σ_3 is the only diagonal matrix therefore the above contribution can be written in a simpler form as

$$\frac{1}{2}g^2\left[H_u^{0*}\mathbf{t_3}H_u^0 + H_d^{0*}\mathbf{t_3}H_d^0 + \tilde{t}_L^*\mathbf{t_3}\tilde{t}_L\right]^2 + ..., \tag{3.4}$$

where g is the coupling constant for the $SU(2)$ gauge group. In the above equation there is no contribution for $\tilde{t}_R$ as it transforms as a singlet under the $SU(2)$ gauge group. After replacing the Higgs fields with the corresponding expectation values and keeping only the terms that are quadratic in $\tilde{t}_L$ we get

$$\frac{1}{2}g^2\left[\frac{1}{4}\left(v_1^2 - v_2^2\right) + \frac{1}{2}\right]\tilde{t}_L^*\tilde{t}_L. \tag{3.5}$$

In Eq. 3.3, if we take the gauge group to be $U(1)_Y$ and collect the terms that are quadratic in $\tilde{t}_L$ and $\tilde{t}_R$ we get

$$-\frac{1}{8}g'^2\left(v_2^2 - v_1^2\right)\left[\frac{1}{3}\tilde{t}_L^*\tilde{t}_L - \frac{4}{3}\tilde{t}_R^*\tilde{t}_R\right]. \tag{3.6}$$

where g' is the coupling constant of $U(1)_Y$ gauge group. Further using the following relations

$$\cos 2\beta = \frac{v_2^2 - v_1^2}{v_2^2 + v_1^2}, \tag{3.7}$$

$$\sin^2\theta_w = \frac{g'^2}{g^2 + g'^2}, \tag{3.8}$$

$$M_Z^2 = \frac{v_1^2 + v_2^2}{4(g^2 + g'^2)}, \tag{3.9}$$

and combining the contributions in Eqs. 3.5 and 3.6 we get

$$\tilde{t}_L \;:\; M_Z^2\cos 2\beta\left(\frac{1}{2} - \frac{2}{3}\sin^2\theta_W\right), \tag{3.10}$$

$$\tilde{t}_R \;:\; \frac{2}{3}M_Z^2\cos 2\beta\sin^2\theta_W, \tag{3.11}$$

where θ_W is the weak mixing angle and $\tan\beta$ is the ratio of the vacuum expectation values of two Higgs doublets i.e. $\tan\beta = v_2/v_1$.

Next we evaluate the off diagonal contributions to the $\tilde{t}$ mass matrix. These arise from the terms that are cubic in the scalar fields where a Higgs field is sandwiched between left and right $\tilde{t}$ fields. The terms from soft SUSY breaking part are

$$a_t v \sin\beta \tilde{t}_L^* \tilde{t}_R + a_t v \sin\beta \tilde{t}_R^* \tilde{t}_L. \tag{3.12}$$

Finally, the last off-diagonal contribution arises from the F-terms of the form $-\mu v y_t \cos\beta \tilde{t}_L^* \tilde{t}_R - \mu v y_t \cos\beta \tilde{t}_R^* \tilde{t}_L$.

After combining all contributions, we obtain a (mass)^2 matrix for the $\tilde{t}$ which in gauge eigen-state basis $(\tilde{t}_L\ \tilde{t}_R)$ is written as:

$$\mathbf{m_{\tilde{t}}}^2 = \begin{pmatrix} m_{\tilde{t}_L}^2 + m_t^2 + M_Z^2 \cos 2\beta \left(\frac{1}{2} - \frac{2}{3}\sin^2\theta_W\right) & v(a_t \sin\beta - \mu y_t \cos\beta) \\ v(a_t \sin\beta - \mu y_t \cos\beta) & m_{\tilde{t}_R}^2 + m_t^2 + \frac{2}{3} M_Z^2 \cos 2\beta \sin^2\theta_W \end{pmatrix}.$$

The mass eigenvalues are

$$\begin{aligned} m_{\tilde{t}_{1,2}}^2 &= \frac{1}{2}\left(m_{\tilde{t}_L}^2 + m_{\tilde{t}_R}^2\right) + \frac{1}{4} m_Z^2 \cos 2\beta + m_t^2 \\ &\pm \left[\left\{\frac{1}{2}\left(m_{\tilde{t}_L}^2 - m_{\tilde{t}_R}^2\right) + m_Z^2 \cos 2\beta \left(\frac{1}{4} - \frac{2}{3}\sin^2\theta_W\right)\right\}^2 + v^2 \left(a_t \sin\beta - \mu y_t \cos\beta\right)^2\right]^{\frac{1}{2}}. \end{aligned} \tag{3.13}$$

In Eq. 3.13 as the number a_t is in one to one correspondence with y_t we can rewrite last term as $m_t^2(A_t - \mu\cot\beta)$. The physical mass eigenstates can be obtained by performing a unitary rotation and are given by

$$\begin{pmatrix} \tilde{t}_1 \\ \tilde{t}_2 \end{pmatrix} = \begin{pmatrix} \cos\theta_{\tilde{t}} & \sin\theta_{\tilde{t}} \\ -\sin\theta_{\tilde{t}} & \cos\theta_{\tilde{t}} \end{pmatrix} \begin{pmatrix} \tilde{t}_L \\ \tilde{t}_R \end{pmatrix}.$$

where $\theta_{\tilde{t}}$ is $\tilde{t}$ mixing angle. One can see from the mass eigenvalue equation that the splitting between the masses of two scalar top quarks is proportional to the mass of the top quark, which makes one of the scalar top quark lighter than the other.

A second reason to believe that the $\tilde{t}$ is light is related to the SUSY breaking at a very high scale compared to the electroweak scale [6, 7]. In the minimal Supergravity (mSUGRA) model,

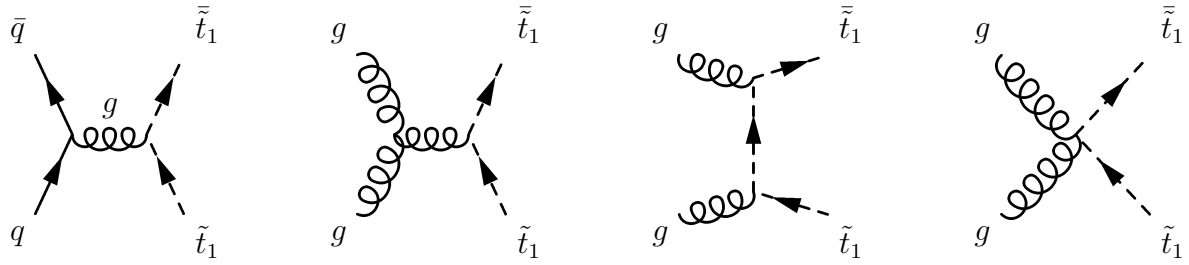

Figure 3.1: Feynman diagrams for $\tilde{t}_1$ pair production at the Fermilab Tevatron Collider.

SUSY is assumed to be broken at a high energy scale. The high energy scale parameters are taken to be universal which include a universal scalar mass m_o, a universal gaugino mass $m_{1/2}$, a universal trilinear coupling A_0, ratio of the vacuum expectation values of two Higgs, $\tan\beta$ and sign of the higgsino mixing parameter μ. All these parameters are the input variables at the GUT scale. Their values at the electroweak scale are calculated using renormalization group equations (RGE). RGE evolution tend to order the squark masses in an inverse hierarchy with respect to their Yukawa couplings [15]. Top Yukawa coupling being the largest of all therefore makes the $\tilde{t}$ weak eigenstates lighter than all other squarks at the electroweak scale.

For the reasons discussed above, one of the two scalar top quarks, can be the lightest of all squarks. We will use the symbol $\tilde{t}_1$ to denote the lightest scalar top quark.

3.2 $\tilde{t}_1$ Production at the Tevatron

The $\tilde{t}_1$ is a colored object like top quark and is produced at the Fermilab Tevatron Collider through strong interactions. The $\tilde{t}_1$ pair production will occur through quark-antiquark annihilation (85%) and gluon-gluon fusion (15%) [16, 17, 18].

$$q\bar{q} \rightarrow \tilde{t}_1\bar{\tilde{t}}_1. \tag{3.14}$$

$$gg \rightarrow \tilde{t}_1\bar{\tilde{t}}_1. \tag{3.15}$$

Figure 3.1 shows the relevant diagrams for $\tilde{t}_1$ pair production. The partonic level cross section for

these processes can be written as

$$\hat{\sigma}_{\mathtt{LO}}[q\bar{q} \to \tilde{t}_1\bar{\tilde{t}}_1] = \frac{\alpha_s^2\pi}{\hat{s}}\frac{2}{27}\beta_1^3, \tag{3.16}$$

$$\hat{\sigma}_{\mathtt{LO}}[gg] \to \tilde{t}_1\bar{\tilde{t}}_1] = \frac{\alpha_s^2\pi}{96\hat{s}}\left\{\beta_1\left(41-31\beta^2\right)+\left(18\beta^2-\beta^4-17\right)\mathtt{log}\left(\frac{1+\beta_1}{1-\beta_1}\right)\right\}, \tag{3.17}$$

where $\sqrt{\hat{s}}$ is the center of mass energy and $\beta_1 = \sqrt{(1-4m_{\tilde{t}_1}^2/\hat{s})}$. Figure 3.2 shows the $\tilde{t}_1$ pair

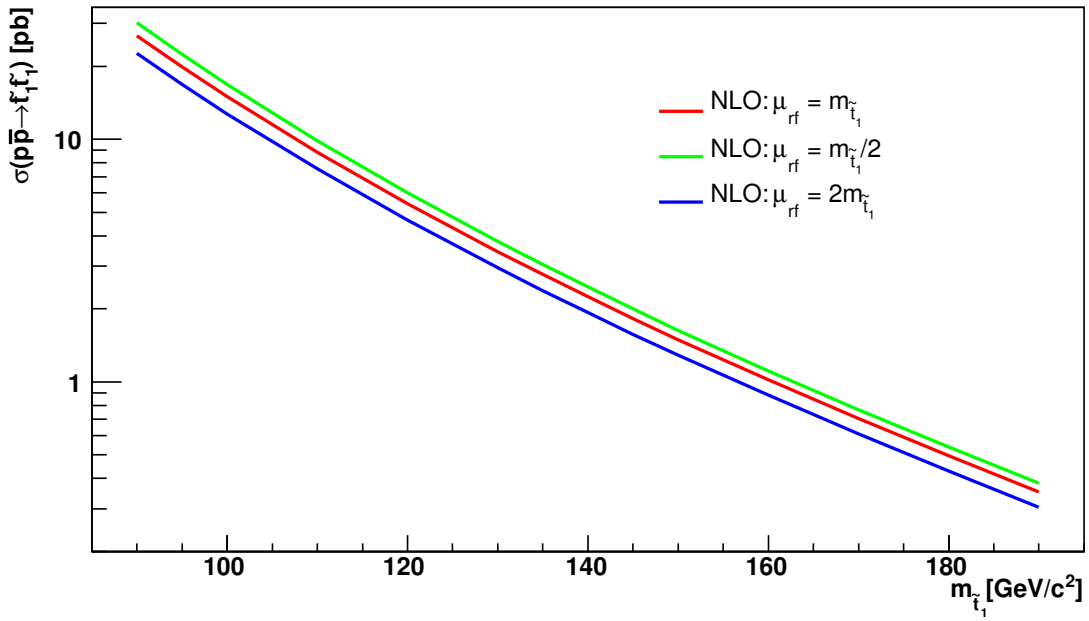

Figure 3.2: Theoretical $\tilde{t}_1$ pair production cross section at next to leading order using PROSPINO. Three different plots correspond to different choices of factorization and renormalization scale.

production cross section at next to leading order obtained using PROSPINO [19]. The cross section ranges from 20 pb to 1 pb for $\tilde{t}_1$ masses between $95-160$ GeV. This is important to note that though $\tilde{t}_1$ quark is produced like top quark through gluon exchange but the cross section for a $\tilde{t}_1$ having the same mass as top is ten times smaller than that for top quark production. This suppression is due to the fact that $\tilde{t}_1$ quark has spin 0 while top quark is a spin $1/2$ object. In the evaluation of cross section values, CTEQ6.1M parton distribution functions [20, 21] are used. The three lines in Fig. 3.2 correspond to three different choices of renormalization and factorization scales i.e. $\mu_{rf} = m_{\tilde{t}_1}$, $\mu_{rf} = m_{\tilde{t}_1}/2$, $\mu_{rf} = 2m_{\tilde{t}_1}$. The renormalization and factorization scales are

the choices of energy scales to have finite values of partonic level cross sections at high energies and parton distribution functions at low energies respectively.

The upward and downward errors due to the PDF choice are evaluated as

$$\delta\sigma^{\rm up}_{\rm PDF} = \frac{\sqrt{\sum_{xx=0}^{xx=40}|\sigma({\rm CTEQ6.1M.xx})-\sigma({\rm CTEQ6.1M})|^2}}{\sigma({\rm CTEQ6.1M})}, \tag{3.18}$$

for $\sigma({\rm CTEQ6.1M.xx}) > \sigma({\rm CTEQ6.1M})$, and

$$\delta\sigma^{\rm down}_{\rm PDF} = -\frac{\sqrt{\sum_{xx=0}^{xx=40}|\sigma({\rm CTEQ6.1M.xx})-\sigma({\rm CTEQ6.1M})|^2}}{\sigma({\rm CTEQ6.1M})}, \tag{3.19}$$

for $\sigma({\rm CTEQ6.1M.xx}) < \sigma({\rm CTEQ6.1M})$.

The upward and downward errors due to the renormalization and factorization scale are evaluated as

$$\delta\sigma^{\rm up}_{\mu_{\rm rf}} = \frac{\sigma(\mu_{\rm rf}=m_{\tilde{t}_1}/2)-\sigma(\mu_{\rm rf}=m_{\tilde{t}_1})}{\sigma(\mu_{\rm rf}=m_{\tilde{t}_1)}}. \tag{3.20}$$

$$\delta\sigma^{\rm down}_{\mu_{\rm rf}} = \frac{\sigma(\mu_{\rm rf}=2\times m_{\tilde{t}_1})-\sigma(\mu_{\rm rf}=m_{\tilde{t}_1})}{\sigma(\mu_{\rm rf}=m_{\tilde{t}_1)}}. \tag{3.21}$$

The total error is then evaluated as

$$\delta\sigma^{\rm up}_{\rm tot} = \sqrt{(\delta\sigma^{\rm up}_{\rm PDF})^2+(\delta\sigma^{\rm up}_{\mu_{\rm rf}})^2}. \tag{3.22}$$

$$\delta\sigma^{\rm down}_{\rm tot} = \sqrt{(\delta\sigma^{\rm down}_{\rm PDF})^2+(\delta\sigma^{\rm down}_{\mu_{\rm rf}})^2}. \tag{3.23}$$

The combined uncertainty on the $\tilde{t}_1$ pair production cross section due to the scale and PDF choice were estimated to be $\approx 20\%$. This uncertainty was added (subtracted) to the nominal value of the cross section in order to obtain the upper (lower) values of the cross section.

3.3 Decay Modes of $\tilde{t}_1$

Since the decay width of $\tilde{t}_1$ depends on the mass of $\tilde{t}_1$, therefore the kinematically available phase space may be different for different masses under consideration. The $\tilde{t}_1$ quark can have two, three

or four body decay modes [15, 22, 23, 24, 25].

Two Body Decays of $\tilde{t}_1$

If $m_{\tilde{t}_1} > m_t$, where $m_{\tilde{t}_1}$ is the $\tilde{t}_1$ mass and m_t is the top quark mass, a possible two body decay mode at tree-level can be $\tilde{t}_1 \rightarrow t\tilde{\chi}_1^0$. This decay mode is strongly suppressed due to the large top quark mass and the phase space required for this process to occur. If, on the other hand, chargino-the lightest mass eigen state resulting from the mixing of the SUSY partners of the charged gauge and Higgs bosons-is lighter than the $\tilde{t}_1$, the two body decay via $\tilde{t}_1 \rightarrow b\tilde{\chi}^+$ becomes available. The chargino decays into a W boson and a $\tilde{\chi}_1^0$ giving rise to a final state with two b jets, four fermions and a $\tilde{\chi}_1^0$ pair. The event signature is very similar to the one for top quark decay except the presence of neutralinos. One can also write down the decay mode $\tilde{t}_1 \rightarrow t\tilde{g}$. The current lower limit on the gluino mass (308 GeV) [26] requires a rather heavy $\tilde{t}_1$ for this decay to happen.
For a $\tilde{t}_1$ lighter than the top quark and with $m_{\tilde{t}_1} < m_b + \tilde{\chi}^+$ the only two body decay available is the loop decay into a charm quark and a $\tilde{\chi}_1^0$ via $\tilde{t}_1 \rightarrow c\tilde{\chi}_1^0$. For this decay mode $\tilde{t}_1$ is taken to be the next to the lightest supersymmetric particle.

Three Body Decays of $\tilde{t}_1$

If $m_{\tilde{\chi}^\pm} < m_{\tilde{t}_1} - m_b$, the $\tilde{t}_1$ will decay at tree level via three-body decays $\tilde{t}_1 \rightarrow b\ell\tilde{\nu}$ or $\tilde{t}_1 \rightarrow b\nu\tilde{\ell}$ where l is a lepton and can be an electron, muon or tau.

Four Body Decay of $\tilde{t}_1$

If sleptons and sneutrinos are heavier than the top squark, the dominant decay at tree level will be a four body decay via $\tilde{t}_1 \rightarrow bf\bar{f}\tilde{\chi}_1^0$ where f is a light quark or lepton.

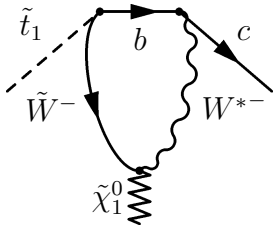

Figure 3.3: Loop decay of $\tilde{t}_1$ into a charm quark and a neutralino.

3.4 $\tilde{t}_1 \rightarrow c\tilde{\chi}_1^0$ Decay Mode

In the search presented in this thesis, it is assumed that $m_{\tilde{t}_1} < m_W + m_b + m_{\tilde{\chi}_1^0}$ and $m_{\tilde{t}_1} < m_b + m_{\tilde{\chi}_1^+}$ and $\tilde{t}_1$ is assumed to decay with 100% branching fraction into a charm quark and a $\tilde{\chi}_1^0$. The tree-level two body decay into a top quark and $\tilde{\chi}_1^0$ is kinematically forbidden and tree-level four body decay can be neglected. R-parity conservation requires $\tilde{t}_1$ to be produced in pairs giving rise to an event signature with two acoplanar charm jets and missing energy in the plane transverse to the beam direction. The missing transverse energy arises due to the presence of neutralinos which escape detection [27]. Figure 3.3 shows the Feynman diagram describing the two body loop decay of $\tilde{t}_1$ into a charm quark and a $\tilde{\chi}_1^0$.

3.5 Current Experimental Limits on $\tilde{t}_1$ Mass

Supersymmetric top quark has been searched for in several different channels in the data taken by colliders which include Large Electron Positron (LEP) and Tevatron. Four experiments[1] at LEP have searched for $\tilde{t}_1$ in $\tilde{t}_1 \rightarrow c\tilde{\chi}_1^0$ and $\tilde{t}_1 \rightarrow b\ell\tilde{\nu}$ channels [28, 29, 30, 31]. Lower limits on $\tilde{t}_1$ mass have been set at 95% C.L. for two different values of $\theta_{\tilde{t}}$, 0° and 56° by LEP. $\theta_{\tilde{t}} = 56^\circ$ corresponds to a situation when there is no contribution from Z^0 exchange in e^+e^- collisions. The excluded $\tilde{t}_1$ mass in $\tilde{t}_1 \rightarrow c\tilde{\chi}_1^0$ mode ranges from $98 - 100$ GeV for $\theta_{\tilde{t}} = 0^\circ$ and $95 - 98$ GeV for $\theta_{\tilde{t}} = 56^\circ$ depending on the difference between $\tilde{t}_1$ and $\tilde{\chi}_1^0$ masses which is taken to be between $20 - 60$ GeV. At Tevatron, both CDF and D0 collaborations have searched for $\tilde{t}_1$ in events with leptons, jets and

[1] ALEPH, DELPHI, OPAL, L3.

missing transverse energy. CDF search modes include $\tilde{t}_1 \rightarrow c\tilde{\chi}_1^0$ and $\tilde{t}_1 \rightarrow b\ell\tilde{\nu}$ where in the latter two leptons can be electrons or muons, or one electron and a muon [32, 33, 34]. In $\tilde{t}_1 \rightarrow c\tilde{\chi}_1^0$ mode, CDF collaboration has excluded $m_{\tilde{t}_1} < 132$ GeV, for $m_{\tilde{\chi}_1^0} = 48$ GeV using 295 pb^{-1} of luminosity [35].

D0 Run I [36, 37] and RunII [38, 39] searches include $\tilde{t}_1 \rightarrow b\tilde{\chi}^{\pm}$, $\tilde{t}_1 \rightarrow c\tilde{\chi}_1^0$, $\tilde{t}_1 \rightarrow b\ell\tilde{\nu}$ decay modes. The largest $\tilde{t}_1$ mass excluded by the D0 collaboration in $\tilde{t}_1 \rightarrow c\tilde{\chi}_1^0$ mode is 134 GeV obtained for $m_{\tilde{\chi}_1^0} = 48$ GeV using 310 pb^{-1} of luminosity [39] .

Figure 3.4 shows the regions of $\tilde{t}_1 - \tilde{\chi}_1^0$ mass plane excluded by LEP, CDF and D0 collaborations

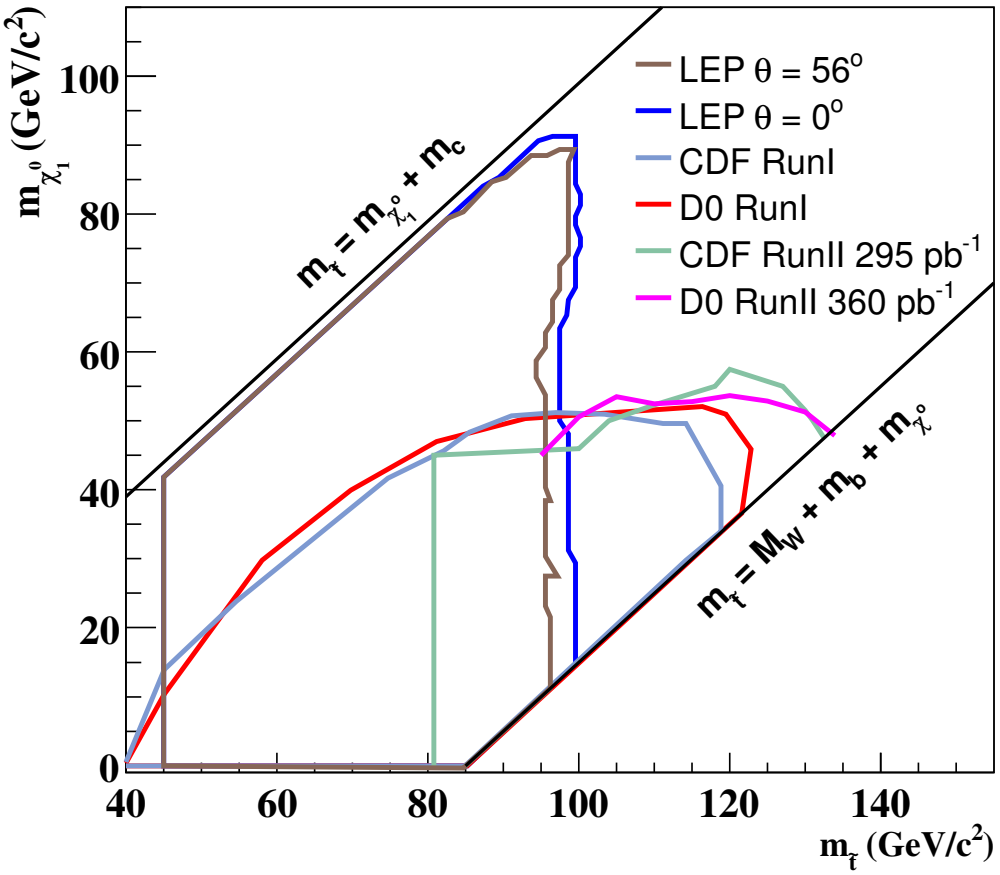

Figure 3.4: Region in $\tilde{t}$ - $\tilde{\chi}_1^0$ mass plane excluded by CDF, D0 and LEP collaborations at the 95% C.L. The limits are set using the $\tilde{t}_1 \rightarrow c\tilde{\chi}_1^0$ decay channel.

at the 95% C.L., using the $\tilde{t}_1 \rightarrow c\tilde{\chi}_1^0$ decay channel. The areas under the curves are excluded by

the corresponding searches.

Chapter 4

Experimental Apparatus

The search for $\tilde{t}_1$ was performed on the data collected with the D0 detector at the Fermilab Tevatron collider. In this chapter, after presenting an overview of the accelerator complex at Fermilab, to which Tevatron belongs, a brief description of the D0 detector will be given.

4.1 Fermilab

Fermilab, a national accelerator laboratory located in Batavia, IL was built in 1967 to perform research in the field of high energy particle physics. The Tevatron accelerator located at Fermilab is a proton anti-proton ($p\bar{p}$) collider and is a part of the accelerator complex shown in Fig. 4.1. In the Tevatron, protons and anti-protons are accelerated up to the energies of 980 GeV before collisions between them take place. The collisions between protons and anti-protons occur every 396 ns at a total center of mass energy of 1.96 TeV.

4.2 Fermilab Accelerator Complex

Due to the limitations of each type of accelerator, the accelerator chain at Fermilab is a collection of different types of accelerators. These include [40]

- Cockcroft-Walton accelerator.
- Linac.

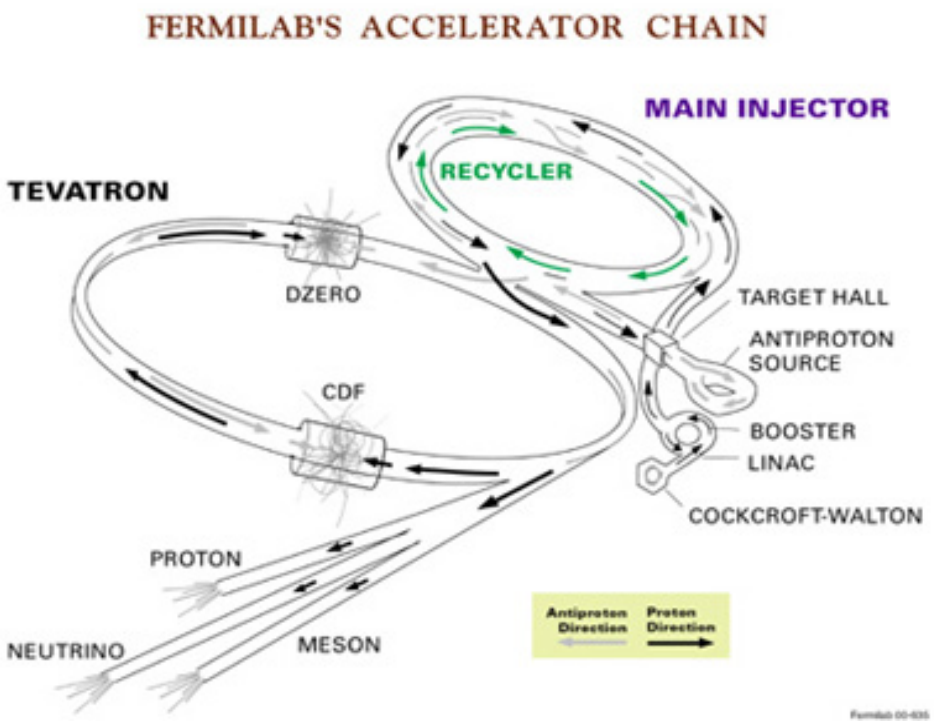

Figure 4.1: Chain of accelerators at Fermilab.

- Booster.
- Main injector.
- Tevatron.

The acceleration of protons takes place in five steps which are described in next sections.

4.2.1 Pre-accelerator

In the first step hydrogen gas is ionized to produce H^- ions. These ions have two electrons and one proton [41]. In the Cockcroft-Walton accelerator, positive voltage is used to accelerate these negative ions up to 750 keV.

4.2.2 Linac

Linac stands for linear accelerator. The 750 keV H^- ions are passed through the linac which is about 500 feet long. With the help of oscillating electric fields, the negative ions are accelerated

up to 400 MeV. Before entering into the next stage of acceleration, the negative ions are passed through a carbon foil to strip off the electrons.

4.2.3 Booster

After removing the electrons from the negative ions, the 400 MeV protons are then sent into the booster which is a circular ring located about 20 feet below ground. At this stage magnets are used to bend the proton beam. While circulating in the booster protons pick up more energy at each revolution and before leaving the booster have gained energies up to 8 GeV.

4.2.4 Main Injector

Main injector is used to perform four different tasks. It

- accelerates protons coming from booster to 150 GeV.
- produces 120 GeV protons to go into anti-proton source where they strike the nickel target. In p-Ni collisions a bunch of particles are produced including anti-protons. The 8 GeV anti-protons are separated from other particles using a magnetic dipole spectrometer. For every million protons only 15 anti-protons are produced. The 8 GeV anti-protons are then transfered to the debuncher. The transverse momentum profile of anti-protons is reduced and they are induced into an ideal orbit using stochastic cooling. Next anti-protons are moved to an accumulator where they are stored and bunched until a sufficient number has been produced.
- accelerates anti-protons to 150 GeV.
- injects protons and anti-protons into the Tevatron.

4.2.5 Tevatron

After being accelerated up to 150 GeV, protons and anti-protons are injected into the Tevatron ring. Tevatron consists of a circular ring of circumference 6.3 km and uses superconducting dipole and

quadrapole magnets to keep protons and anti-protons on track while accelerating them up to 980 GeV. While circulating in the Tevatron tunnel, protons and anti-protons meet at two points known as B0 and D0 where the two detectors known as CDF and D0 are located. After the collisions have occurred, the detectors are used to record and search for newly created particles in the debris of $p\bar{p}$ collisions.

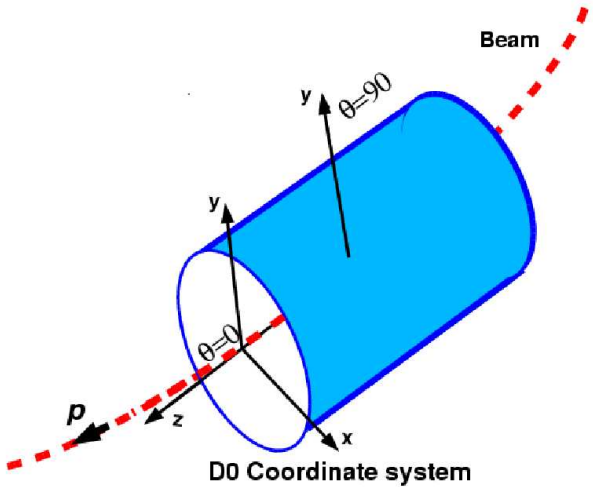

Figure 4.2: Coordinate system used at D0.

4.3 D0 Coordinate System

Before going into the details of the sub-detector systems at D0, a brief introduction to the coordinate system used at D0 is presented. A right handed coordinate system, as shown in Fig. 4.2 [42], is used at D0 with z-axis taken along the outgoing proton beam direction, the y axis being vertically upwards and x axis lying in the horizontal plane pointing towards the center of the Tevatron ring. The origin of the detector is taken to be the geometrical center of the central fiber tracker. The azimuthal and polar angles are denoted by ϕ and θ respectively.

This is important to note that protons and anti-protons move along $\pm z$ directions which means

that the net momentum in the transverse direction i.e. in xy-plane is zero. The laws of conservation of energy and momentum in xy-plane are used to determine the quantities of interest like transverse momentum[1], transverse energy and missing transverse energy which is the imbalance in the energy of the initial and final state particles.

A useful quantity in experimental particle physics is "rapidity", denoted as y, which is used to measure polar angle. It is defined as

$$y = \frac{1}{2}\ln\frac{E + p_z}{E - p_z}.$$

where E is the energy of the particle and p_z is its momentum along z-axis. In the zero mass limit this variable reduces to *pseudorapidity* which is given by

$$\eta = -\ln\left(\tan\frac{\theta}{2}\right).$$

Two reasons for employing η instead of θ are

- pseudorapidities are additive under Lorentz boosts.
- rapidity differences are Lorentz invariant [43].

The difference between two directions (η_1, ϕ_1) and (η_2, ϕ_2) is expressed in terms of ΔR defined as

$$\Delta R = \sqrt{\Delta\eta^2 + \Delta\phi^2}.$$

where $\Delta\eta = |\eta_2 - \eta_1|$ and $\Delta\phi = \min(|\phi_2 - \phi_1|, 2\pi - |\phi_2 - \phi_1|)$.

4.4 The D0 Detector

The D0 detector was proposed in 1983 to search for the new particles produced in the $p\bar{p}$ collisions at the Tevatron. It ran successfully during Run I of the Tevatron, $1992 - 1996$, and was later

[1]Transverse momentum is denoted by p_T and is calculated using the expression

$$p_T = \sqrt{p_x^2 + p_y^2}.$$

where p_x and p_y denote the momentum of a particle along x and y direction respectively.

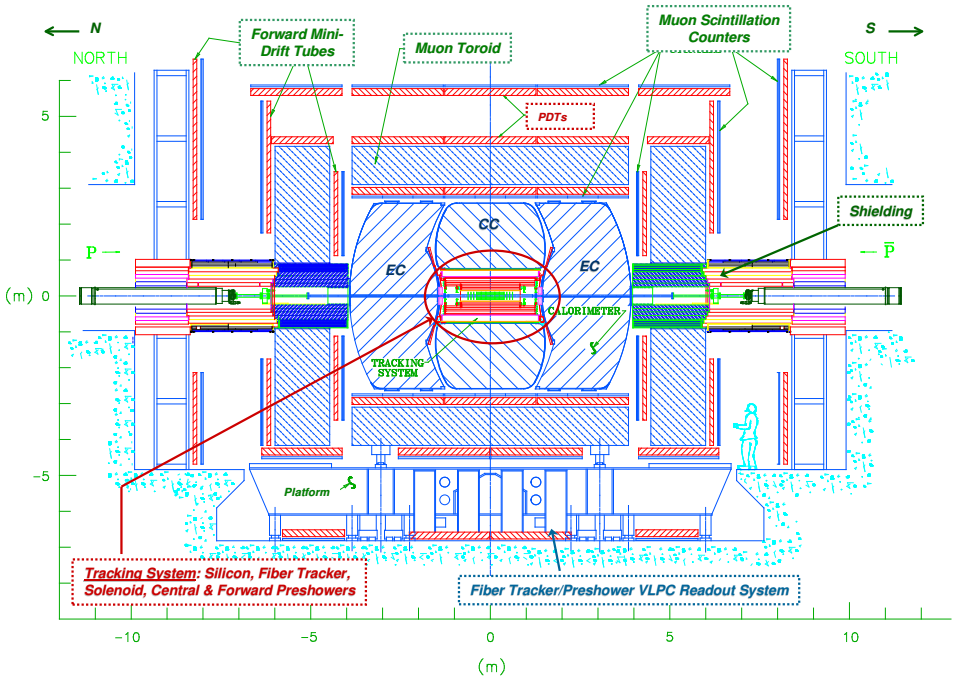

Figure 4.3: Schematic view of the D0 detector showing the sub-detector components including central tracker, calorimeter and muon system.

upgraded to take advantage of the high luminosities delivered by the Tevatron. Three major sub-systems of the detector are central tracking system, which is placed inside a 2 T solenoid magnet, uranium/liquid-argon calorimeter, and a muon spectrometer [44, 45].

The purpose of having the central tracking system is to identify the trajectories of the particles, as they pass through the material, along with the vertex information. The calorimeter is used to measure the energy of each particle. Muons, due to their less interactions with material do not deposit their energy in the calorimeter and are detected by the muon system outside of the calorimeter. Figure 4.3 hows a schematic view of the D0 detector. In the following sections a brief overview of each of the sub-detectors will be presented.

4.4.1 Central Tracking System

The tracking system at D0 consists of two sub-detectors

- Silicon Microstrip Tracker (SMT).

- Central Fiber Tracker (CFT).

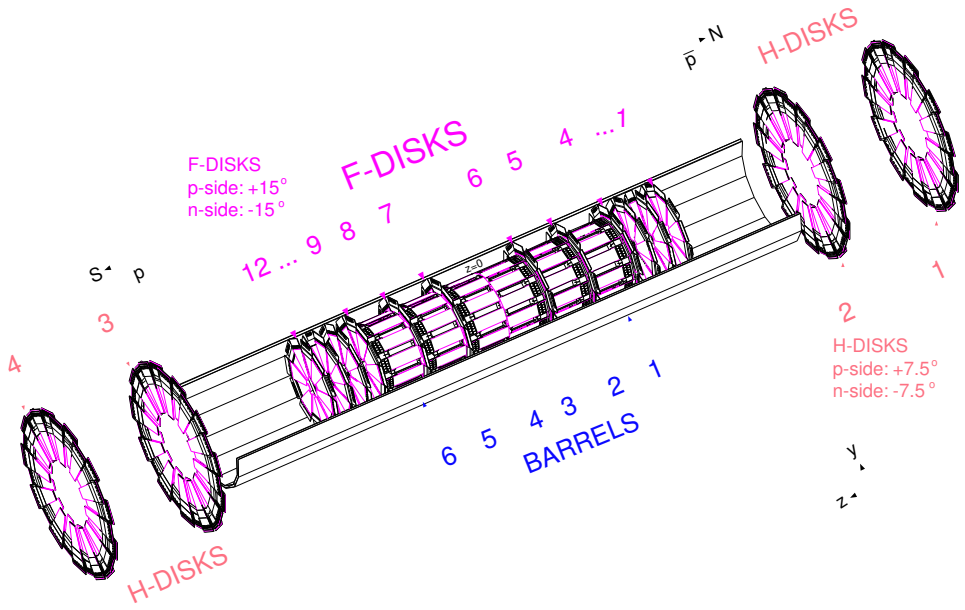

Figure 4.4: Schematic view of the silicon microstrip tracker illustrating the geometry of the barrels, F-disks and H-disks.

Silicon Microstrip Tracker (SMT)

The SMT is a subsystem of the D0 detector which is the closest to the Tevatron beam line. It consists of six barrels, twelve F-disks and four H-disks as shown in Fig. 4.4. Each barrel has eight layers of silicon detectors (also called ladder) while each F-disk has twelve and each H-disk has 24 wedge shaped silicon detectors. The length of the tracker extends form $z = -121$ cm to $z = 121$ cm and its η coverage is up to $|\eta| = 3.0$. The barrel detectors measure the $r - \phi$ coordinate and the disk detectors measure $r - z$ as well as $r - \phi$ for tracks.

When a charged particle passes through the SMT it ionizes the material and produces electron-hole pairs. In the presence of electric field these pairs are attracted towards anode and cathode depending on the charge. The result is a pulse of charge proportional to the deposited energy of the particle that is collected by an amplifier.

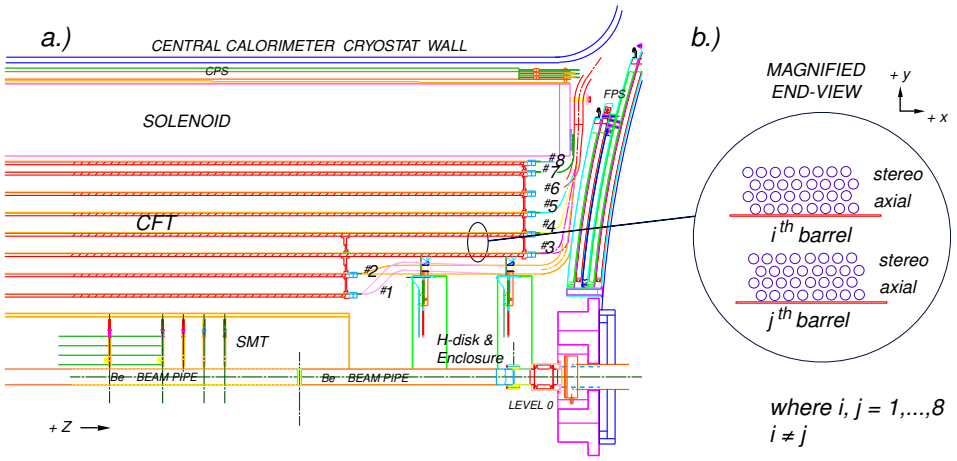

Figure 4.5: a) A quarter $r - z$ view of the CFT detector showing eight concentric cylinders. b) A magnified view of the doublet layer configuration.

Central Fiber Tracker (CFT)

The central fiber tracker as shown in Fig. 4.5 is a cylindrical shape detector outside the SMT and provides coverage up to $|\eta| < 1.7$. It complements the SMT in track reconstruction and momentum measurement due to being located inside a 2 T solenoid magnet. It has scintillating fibers mounted on eight concentric carbon-fiber cylinders. Each cylinder has a layer of fibers parallel to beam pipe (axial layers) and another layer with an angle of $\pm 3^o$ relative to the axial layers (stereo layer). The stereo layers alternate between being at $+3^o$ and -3^o. The axial fibers provide ϕ measurement and, when combined with stereo layers, can provide a measurement of z.

When a charged particle goes through CFT, it excites the atoms in the material which during de-excitation emit visible light which is transmitted to visible light photon counters (VLPC) through waveguides. Photons incident upon the surface of VLPC are converted into electron-hole pairs and are subsequently collected via a 6V bias voltage.

4.4.2 Preshower Detectors

During the D0 upgrade for RunII of Tevatron, a solenoid magnet was placed outside the central tracking system. This increased the amount of material in front of the calorimeter and affected the energy resolution of the calorimeter. In order to recover from this preshower detectors were

placed before the calorimeter to improve the energy measurement in calorimeter. The preshower detectors are divided into two subsystems: one central preshower located in front of the central calorimeter, and two forward preshowers placed in front of the end calorimeters.

The central preshower system (CPS) is a cylindrical detector consisting of three layers of triangular shape scintillator strip. The strips in first layer are placed parallel to the beam axis while those in outer two layers are placed at angles of $\pm 23^o$ with respect to the axial layer. The CPS covers the region of $|\eta| < 1.2$. At the center of each triangular strip, there is a wavelength shifting fiber that carries the light to the VLPCs.

The two forward preshower detectors, very similar in construction to the CPS, are placed in front of the two end cap calorimeters and cover the region with $1.5 < |\eta| < 2.5$. The FPS has two stereo layers of scintillator strips and is read out in the same way as CFT and CPS. The information provided by preshower detectors can be used both on-line (to trigger on the objects) and offline (for improving the identification of electromagnetic objects and hadrons and their energy measurement).

4.4.3 Calorimeter

The calorimeter at the D0 is designed to identify the particles, after combining the information from central trackers, and to measure their energies. It is divided into three parts; one central calorimeter (CC) which is 226 cm long and occupies radii from 75 cm to 222 cm and covers $|\eta| \lesssim 1$; and two end cap calorimeters (EC) which extend converge to $|\eta| \approx 4$. Three different sections of the calorimeter, as shown in Fig. 4.6, are

- Electromagnetic (EM) Calorimeter.
- Fine Hadronic (FH) Calorimeter.
- Coarse Hadronic (CH) Calorimeter.

The active medium for all three calorimeters is liquid argon. The absorber material in EM section is in the form of thin plates (3 or 4 mm thick) made of depleted uranium. The FH part uses rela-

tively thick plates (6 mm) of a uranium-niobium alloy. The coarse hadronic section contains 46.5 mm thick plates of copper in the CC and of stainless steel in the EC.

The principle in identifying the particles and measuring their energy in calorimeter is the identifi-

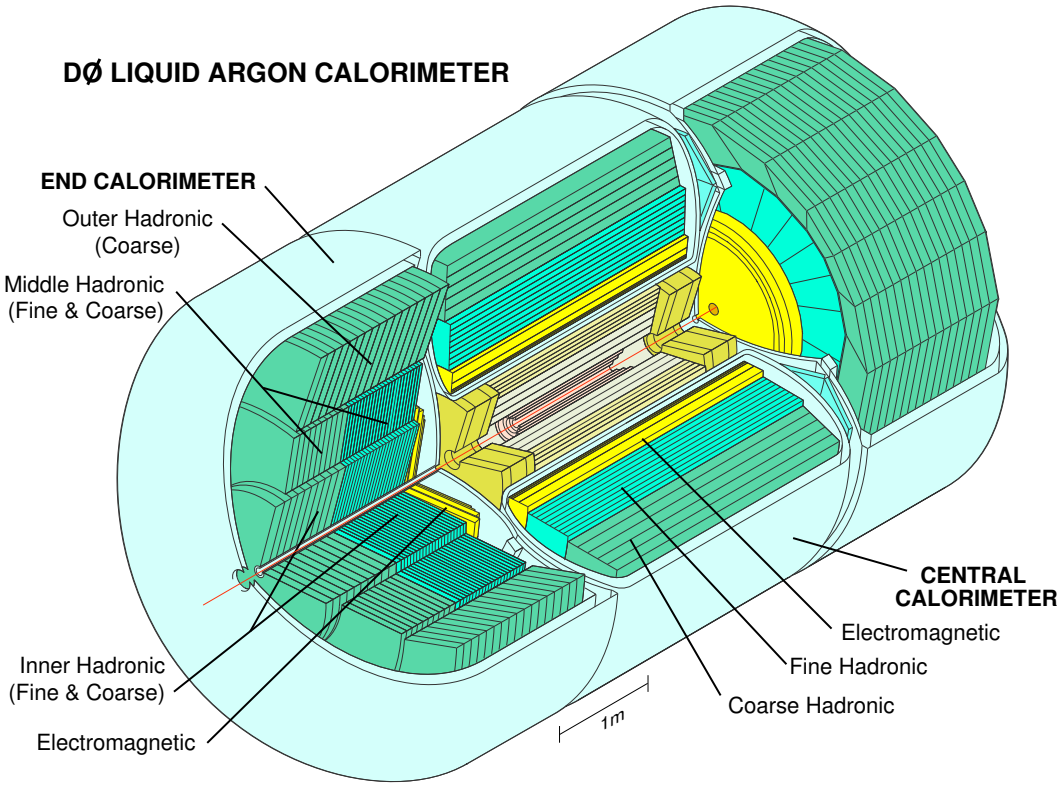

Figure 4.6: A three dimensional view of the D0 calorimeter showing three cryostats as well as electromagnetic and hadronic layers.

cation of showers generated by charged particles. When a highly energetic electron goes through a medium, it loses most of its energy through bremsstrahlung giving rise to the creation of a photon which in turn creates an electron positron pair. Thus a cascade or shower of electrons and positrons develops. When each of these charged particles passes through argon, it ionizes the argon and the ions collected at the anode give rise to voltage pulses. This signal is then amplified and collected to obtain the information about the energy of the incident particle. The calorimeter modules used for this purpose, have 0.1×0.1 segmentation in $\eta \times \phi$ space except in the third layer of EM calorimeter where 0.05×0.05 segmentation is used. The third layer of EM calorimeter is

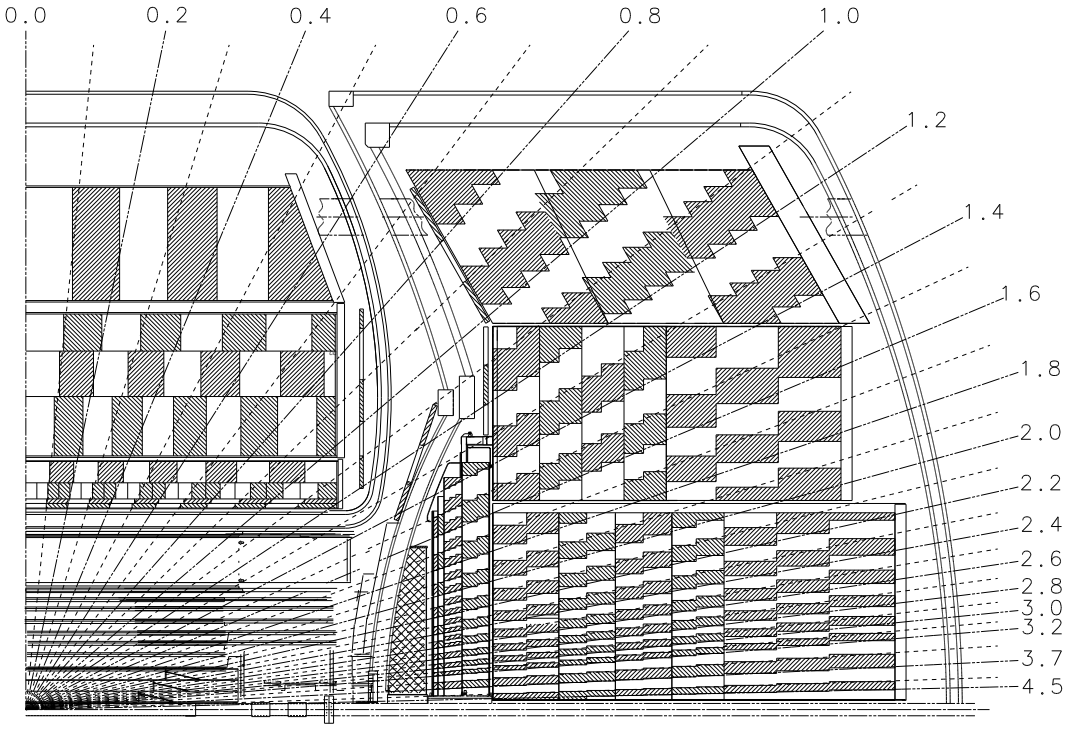

Figure 4.7: Schematic view of one quarter of the D0 calorimeter. Lines extending from the center of the detector represent the η coverage of the readout towers.

placed where electromagnetic shower is expected to reach its maximum, and cell size is reduced to provide improved resolution. The readout modules combined into groups of $\Delta\eta \times \Delta\phi = 0.2 \times 0.2$ readout geometry and, referred to as towers, are shown in Fig. 4.7.

Other than the electromagnetic particles, hadrons are also produced in the interactions that can also cause showers that are qualitatively different from electromagnetic showers. Hadrons lose most of their energies through inelastic collisions with atomic nuclei which can further undergo inelastic collisions and produce secondary showers of hadrons. Since the interaction length for hadrons is much larger than the radiation length for electromagnetic particles[2], hadronic showers are more extended in space than the electromagnetic showers [46]. This is the reason why thick layers of absorber plates are used in the hadronic part of the calorimeter.

[2]For uranium interaction length is 10.2 cm while radiation length is 3.2 mm.

4.4.4 Muon Spectrometer

The outermost detector at the D0 is the muon detector which is used to identify muons and measure their momentum. Though the muon has the same electric charge as electron but it is about 210 times more massive than the electron. The electric force is not large enough to change the muon direction significantly. Therefore the muon goes straight through the calorimeter without radiating photons that can produce showers. The muon system is divided into two parts. Central muon system, that provides coverage for $|\eta| \lesssim 1$ and consists of proportional drift tubes (PDTs) organized in three layers A, B and C. Layer A is located between the calorimeter cryostat and the toroid magnet while layers B and C are outside the toroid. The PDTs in the A layer are covered with scintillator counters and provide a fast detector for triggering on and identifying muons. Second part of the muon spectrometer is forward muon system and consists of three layers of mini drift tubes for muon track reconstruction and three layers of scintillation counters for triggering. It extends the coverage up to $|\eta| \approx 2$. A schematic view of the muon system is shown in Fig. 4.8.

The principle behind the muon detection is as follows; when a muon passes through the drift chamber it ionizes the gas and the resulting free charges drift towards the gold wire (anode) which is held at a positive potential. The resulting electrical signal is collected to measure the position of the muon. Additionally, the scintillator counters also produce light when muon passes through them. In time scintillation counter hits are matched with tracks in the central tracker to trigger on the high p_T single muon and low p_T dimuon events.

4.4.5 Luminosity Monitor

The primary purpose of the luminosity monitor (LM) is to measure the integrated luminosity of the experiment at the collision point which is D0 in this case. It is also used to determine the z vertex of the interaction point and losses due to the beam halo. The LM, as shown in Fig. 4.9, consists of two arrays of plastic scintillation counters and photo multiplier tubes (PMTs) placed at $z = \pm 140$ cm and covers pseudorapidity range $2.7 < |\eta| < 4$. The LM detectors are located in front of the end calorimeter.

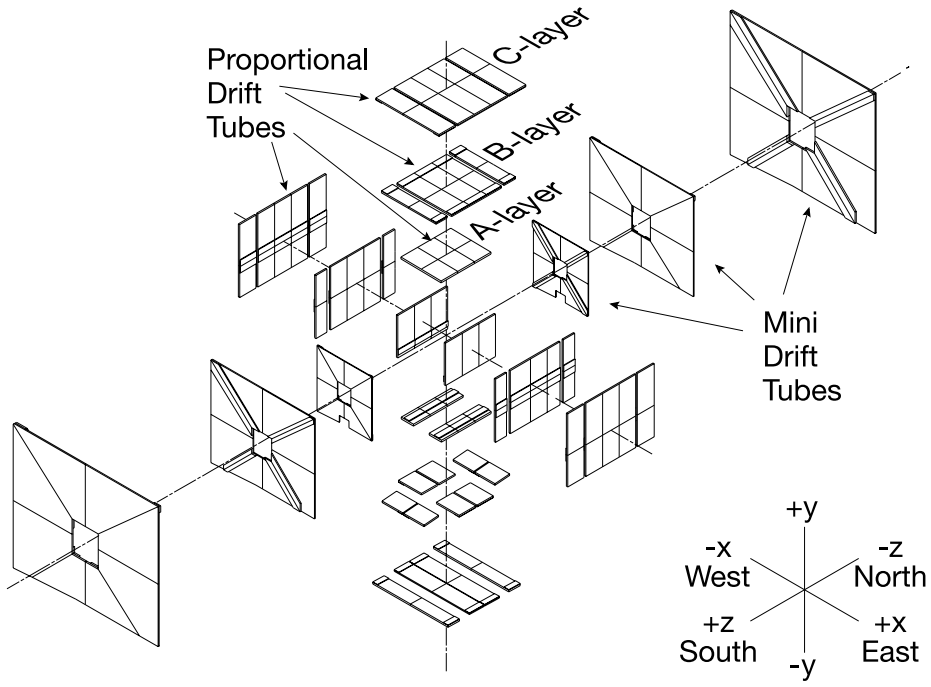

Figure 4.8: An enlarged view of the muon wire chamber.

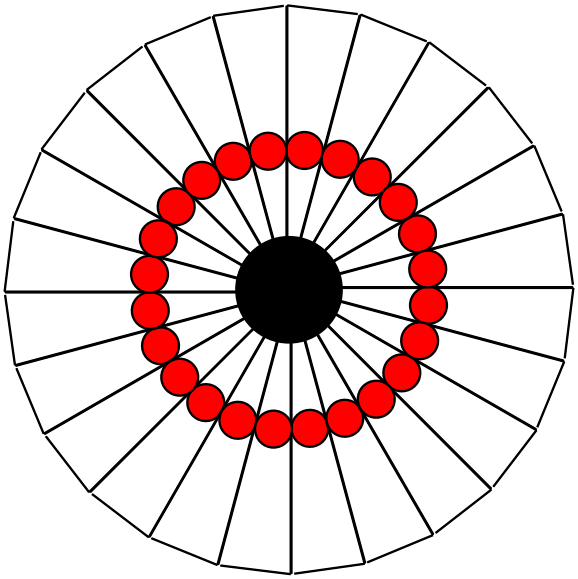

Figure 4.9: Geometry of the luminosity monitor detector and the location of photomultiplier tubes (red circles).

When particles hit the scintillating fibers, light signals are produced. These light signals are amplified by the PMTs and are then used to make trigger decisions. The difference in time of flight given by $z_{vtx} = \frac{c}{2}(t_- - t_+)$, where $t_\pm$ are the time measured by the north (+) and south (-) detectors, is used to determine the longitudinal position of collision.

The luminosity at D0 is measured using the formula $\mathcal{L} = \frac{f\bar{N}_{LM}}{\sigma_{LM}}$ where f denotes the beam crossing frequency and σ_{LM} is the effective cross section for the luminosity monitor that takes into account the detector efficiency and acceptance and $\bar{N}_{LM}$ is the average number of inelastic collisions per beam crossing. As number of collisions in an event can be greater than one therefore beam crossings with no collisions are counted and Poisson statistics is used to determine $\bar{N}_{LM}$.

4.5 Trigger and Data Acquisition System

With a bunch crossing every 396 ns at the Tevatron, the average event rate at D0 can be very large (a couple of million events every second). Furthermore, keeping in view the limitations on the time that it takes for the detector to be read out, the disk space to store the data and the time to

process the data to be analyzed later, it is not possible to record all the interactions occurring at the D0. Most of the events have low p_T objects and are therefore of little interest. The process during which, the decision of keeping or rejecting an events is made, is known as "triggering".

At D0 this is done using three levels of sophisticated combinations of hardware and software,

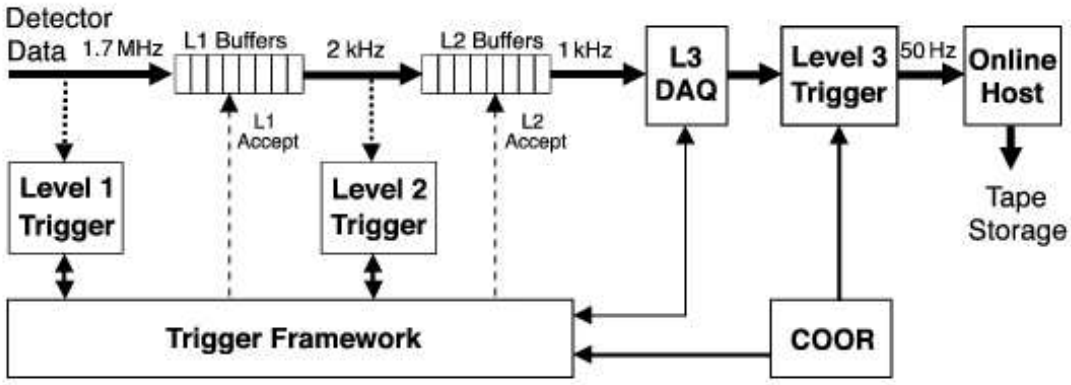

Figure 4.10: A schematic diagram describing the data flow at D0 at different trigger levels..

known as Level 1 (L1), Level 2 (L2) and Level 3 (L3). At each level the properties of an event are compared with a predefined set of criterion and the event is kept if it passes the specific requirements at all three levels.

The L1 trigger, which is a collection of specialized hardware, combines partial information from each sub-detector. The information includes the hit information in central tracker, energy deposition in calorimeter and hits from muon wire chambers. If the energy values in the event are above a minimum threshold or the hit information is acceptable, L1 issues an accept and the event is passed on to L2 for further processing. The L1 trigger has an accept rate of about 2 kHz.

Once an event has passed the requirements at L1, it is sent to the L2. L2 consists of two parts, hardware engines combined with microprocessors related to each sub-detector, and a global processor that makes decision on the basis of information received from each sub-detector. It is at the L2 where physics objects like electrons, jets and muons are constructed and their properties are compared with the requirements given in the trigger list. At the L2 the event rate is reduced to 1

kHz.

After the L2 has issued an accept, the event is sent to L3 data acquisition system, which is a collection of microprocessors. Many sophisticated algorithms are used to determine and improve the quality of reconstructed objects like jets, electrons, muons and tracks. The events rate at L3 is reduced to 50 Hz. Events which pass the requirements at L3 are recorded on tape for future offline reconstructions and data analysis.

Chapter 5

Object Identification and Event Reconstruction

The digitized data collected through the D0 data acquisition system needs to be reprocessed in order to identify physics objects in the event. The physics objects include electrons, muons, jets, tracks and missing transverse energy. Electrons and muons represent the leptons produced in an event and jets indicate the production of quarks. Quarks go through a procedure called hadronization and appear in the form of hadronic jets in the detector.
The process of reconstructing an event can be divided into three steps:

- Identification of the local deposition of energy, also called "hits", in the central tracker, calorimeter cells and muon scintillators and chambers.
- Combining information from adjacent hits into tracks in the tracker and into clusters in the calorimeter. A track found in the central tracker indicates that a charged particle has traversed through the detector.
- Combining the information from different sub-detectors into physics objects. For example a cluster in the electromagnetic part of the calorimeter along with a track matched in the central tracker indicates the presence of an electron in an event.

In this chapter an overview of the procedure to reconstruct the physics objects at D0 is presented.

5.1 Tracks

In the formation of tracks the first step is to form clusters using the accumulated charge in adjacent SMT strips and light from neighboring CFT fibers. The next step is to construct tracks out of the cluster information. Two different algorithms, the Alternate Algorithm (AA) and Histogram Track Finding (HTF) are used for this purpose. A detailed description about the pattern recognition and track fitting can be found in [47].

The AA tracking algorithm starts from three clusters in SMT that have p_T above a minimum threshold (180 MeV) and the distance of closest approach with respect to the beam spot less than 2.5 cm. The track is extrapolated to the next layer of SMT or CFT and the position where the track would have crossed the layer is calculated. If a hit is found near this location, it is added to the track and extrapolation to the next layer is continued and same procedure is repeated. At each layer, the value of χ^2 of the resulting track hypothesis is calculated and a hit is discarded if this value is larger than 16 [48, 49]. This process is continued unless the further addition does not improve the quality of the track.

The HTF algorithm [50] starts from the hits in the SMT and for the given (x,y) position of each hit calculates the curvature ρ, and trajectory angle ϕ for each track candidate. A two dimensional histogram is constructed from ρ and ϕ values. Since all hits from the same track refer to same point in ρ, ϕ parameter space, the bin content corresponding to particular ρ, ϕ value is incremented. The peak values in the histogram correspond to a good track candidate.

For either algorithm, Kalman filtering [51] is used to improve the track quality and perform a more refined fit. The track candidates from both algorithms are combined and duplicates are removed in order to produce a list of tracks, along with the χ^2 probability for each track.

5.1.1 Isolated Tracks

To find an isolated track, all reconstructed tracks with $p_T > 1.5$ GeV, CFT hits ≥ 8, rdca < 2 cm, and zdca < 5 cm are considered, where rdca is the distance of a track in the $r\phi$ direction from the primary vertex and and zdca is the distance in the z direction. For each candidate track, a loop is

performed over all other tracks to search for tracks satisfying the same quality criterion and lying in a hollow cone with $0.1 < \Delta R < 0.4$ around that track. A track is declared isolated if no such track is found in the hollow cone around the candidate track.

5.2 Primary Vertex

The collisions between protons and anti-protons take place at a point in space which is recognized by the tracks emerging out of it. Such a point in each event is referred to as the "primary vertex" (PV). It is important to identify a correct PV as all jets, electrons, muons and missing transverse energy ($\not\!\!E_T$) are reconstructed with respect to the PV. The PV reconstruction at D0 is done in two steps using the reconstructed tracks [52].

In the first step, tracks with $p_T > 0.5$ GeV and at least two (zero) SMT hits within (out of) the SMT acceptance[1] are grouped into clusters. A track that satisfies above mentioned selection criteria is added to the cluster if its distance from the cluster position along z direction is less than 2 cm. The position of the vertex is determined by fitting all selected tracks within each cluster into a common vertex. The tracks with the highest χ^2 contribution are removed until the total vertex χ^2 per degree of freedom is smaller than 10 [53].

In the second step, the position of the vertex calculated in previous step is used to determine the distance of closest approach of each track in the cluster. The quantity $\mathrm{dca}/\sigma_{\mathrm{dca}}$ (known as dca significance) is required to be smaller than 5. The tracks are then fitted to a common vertex using the adaptive vertex fitter algorithm [52], in which track errors are re-weighted according to their χ^2 contribution to the vertex by the function

$$w_i = \frac{1}{1 + e^{(\chi_i^2 - \chi_{\mathrm{cutoff}}^2)/2T}}$$

where χ_i^2 is the χ^2 contribution of the ith track to the vertex, χ_{cutoff}^2 is the distance where weight function drops to 0.5 and T is the parameter that controls the sharpness of the function. The distribution of weight function as a function of track χ^2 is shown in Fig. 5.1.

[1] The SMT fiducial region is defined in track η-z plane, as the region in which the fraction of tracks with at least 2 SMT hits is greater than zero.

In $p\bar{p}$ collisions, in addition to the hard scattering, there can be additional collisions due to the multiple interactions. The list of vertices created in previous step may have a hard scatter as well as a minimum bias (MB) vertex. Using the fact that tracks coming from a hard scatter vertex have larger p_T than the ones coming from MB interaction, the $\log_{10}(p_T)$ of tracks is used to calculate the probability that a track comes from a MB vertex. The vertex with the minimum probability is selected as the PV.

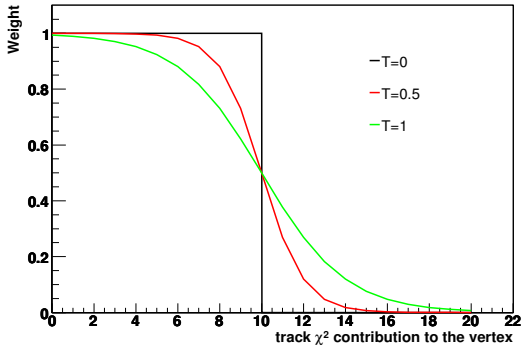

Figure 5.1: Weight assigned to a track as a function of track χ^2 contribution to the vertex for different T values. In the adaptive fitting algorithm, all tracks contribute to the fit when T >0.

5.3 Electron and Photon Identification

Electrons and photons are identified in the calorimeter with the help of showers they create via bremsstrahlung and photon conversion. The depth of the electromagnetic part of the calorimeter is designed to make sure that the electron or photon comes to a complete stop. In the beginning, the identification of electrons and photons is grouped together into the identification of electromagnetic (EM) objects and at the final stage the EM objects for which a matching track can be found in the central tracker are referred to as electrons while those without tracks are categorized as photons.

The process of identification of EM objects starts with clustering, which groups together adjacent cells in the calorimeter, by forming a cone of radius $\Delta R = 0.2$ around a cell with highest energy. Every time a new cell is added to the cluster, the center of the cluster is recalculated. The fraction

of the total energy of an EM cluster deposited in the EM layers of the calorimeter is required to be greater than 90%. Another variable, called *isolation*, is based on the fact that the EM showers are narrow and an EM object deposits most of its energy in a tight cone. The isolation variable, defined as

$$f_{\text{iso}} = \frac{E_{\text{tot}}(R < 0.4) - E_{\text{EM}}(R < 0.2)}{E_{\text{EM}}(R < 0.2)}, \tag{5.1}$$

is required to be less than 0.15, where E_{EM} is the energy deposited in the electromagnetic layers of the calorimeter and E_{tot} is the total energy of the cluster.

Furthermore a tool constructed from seven (eight) variables is used to distinguish between the shower shapes of electromagnetic and hadronic objects. The inverse of the covariance matrix (referred to as H-Matrix7(8)) is constructed from the following variables:

- The energy fraction in the four electromagnetic layers.
- Total energy of the EM cluster which includes the energy in the preshower and fine-hadronic layers of the calorimeter.
- The position of the PV.
- The widths of the showers in the third EM layer of the calorimeter in $r - \phi$ and z. The H-Matrix7 which does not consider the shower shape in z direction, is used for EM object identification in the central part of the calorimeter while H-Matrix8 is used in the end caps.

The H-Matrix is trained against the simulation of electrons coming from W and Z bosons decays. A χ^2 variable is calculated using H-Matrix and the probability or the likelihood of a calorimeter cluster to be coming from an EM object is calculated. The smaller values of χ^2 correspond to more electron-like EM objects.

5.4 Muon Identification

Muons are identified using the combined hit information from muon wire chambers and scintillators. A minimum of two wire chamber hits are required to make a segment. Matching scintillator

hits can be added to the segments if they overlap in η with the segment. The absolute value of $|\mathrm{nseg}| = 1, 2, 3$ indicates whether a muon has hits in A-layer only, in BC-layers only, or both A- and BC-layers respectively[2]. The isolated muons used in this analysis should satisfy following criteria:

- There should be at least two wire chamber hits in the A-layer and two hits in the BC-layers. Additionally the hits should have a matching scintillator hit.
- The energy deposited in the calorimeter in a hollow cone of radius $0.2 < \Delta R < 0.4$ around the muon direction should be smaller than 2.5 GeV.
- The sum of the p_T of all charged tracks other than the muon in a cone of radius 0.5 around the muon direction should be less than 2.5 GeV.

5.5 Jet Identification

Strongly interacting particles, quarks and gluons, produced in $p\bar{p}$ collisions hadronize and appear in the form of hadronic jets in the calorimeter. The reconstruction of jets allows the measurement of the position (in $\eta - \phi$ space) as well as the energy of the initial quarks and gluons.

Jets at D0 are reconstructed using the mid-point cone algorithm [54]. The procedure starts with clustering of calorimeter energies deposited in the towers with size $\Delta\eta \times \Delta\phi = 0.1 \times 0.1$. Preclusters are formed around the "seed towers" with $E_T > 0.5$ GeV within a cone of radius $\Delta R = 0.3$ around each seed. Preclusters with $E_T > 1$ GeV are retained. Using all the preclusters within a cone of radius $\Delta R = 0.5$, jet η and ϕ directions and energies are estimated using

$$\eta = \frac{\sum_i E_T^i \eta^i}{\sum_i E_T^i}, \tag{5.2}$$

$$\phi = \frac{\sum_i E_T^i \phi^i}{\sum_i E_T^i}, \tag{5.3}$$

$$E_T = \sum_i E_T^i = \sum_i E_i \sin\theta_i, \tag{5.4}$$

[2] A negative value is assigned to a muon which is identified only in the muon system and positive value is assigned if muons are matched to a track in the central tracking system

where i denotes a precluster and θ is the polar angle with respect to the proton beam direction. Every time a new precluster is added to the cone, the direction and energy of the jet is recalculated. This step is repeated until a stable axis is achieved. The resulting cone is saved as a proto-jet. If the distance between two proto-jets with a cone of radius R is larger than R but smaller than $2R$, a new jet axis is formed at the midpoint between the two and used as a precluster. If two jets share energy, they are merged if the shared energy is more than half of the energy of the lower-energy jet. Jets with $E_T < 6$ GeV are removed.

After the preliminary selection, additional quality criteria are applied to jets in order to remove jets due to the calorimeter noise and EM showering. These are described below [55].

- The fraction of jet energy deposited in the EM calorimeter layers is required to be between 0.05 and 0.95. The values of the EM fraction smaller than 0.05 are due to calorimeter noise whereas values greater than 0.95 indicate the presence of an EM object. The requirement on EM fraction has been optimized for different η regions as described in [55].

- The number of calorimeter towers that contain 90% of the jet energy is required to be greater than one. A value of one indicates the presence of an EM object or a hot cell due to calorimeter noise.

- The ratio of the energies of the highest and next-to-highest energetic tower is required to be less than 10.

- Due to the presence of noise in the coarse hadronic part of the calorimeter, the fraction of jet energy deposited in this sector is required to be less than 0.4. This requirement depends on the detector η of the jet and more details can be found in [55].

- The ratio of the jet energy measured by the L1 calorimeter trigger to the reconstructed energy of the jet has to be between 0.2 and 0.5 depending on the η region in which jet is reconstructed.

5.5.1 Jet Energy Scale Correction

In order to map out the energy of a jet measured in the calorimeter back to the energy of the parton produced in the $p\bar{p}$ collisions, a number of corrections need to be applied. These corrections are referred to as jet energy scale (JES) corrections. A detailed description of the procedure and corrections can be found in [56]. An overview is presented here.

- A correction for average energy deposition needs to be applied to correct for the energy that does not originate from the hard scatterer. This energy may be due to multiple parton interaction, energy pile-up from previous beam crossings and underlying events that correspond to the remnants of the interacting hadrons. These are referred to as "off-set" energy corrections.

- The calorimeter response to the energy deposition can be different in different regions due to the non uniformities in the geometry of the calorimeter. The "non-linearity" corrections as a function of jet η and energy are applied to correct for this effect.

- Due to the finite size of the cone, some of the energy may not lie within the jet. Corrections applied to take into account this affect are called "showering corrections".

- A muon found in the jet indicates the presence of a semi-leptonic decay of a b or c quark. Since the muon deposits very little energy in the calorimeter, the energy of the jet needs to be corrected for the presence of muon and a neutrino associated with it. There corrections are called "semi-leptonic" corrections.

The above mentioned corrections are applied to the jets both in data and MC simulation.
There are additional corrections that need to be applied to MC jets in order to correct for the differences between data and MC in the jet resolution, jet identification and reconstruction efficiencies and possible difference between data and MC JES, all in a consistent way. The procedure smears the jets in MC, recalibrate them and removes the jets from an events that have $p_T < 15$ GeV and is referred to as "jet shifting, smearing and removing (JSSR)" [57]. The corrections are derived from

the photon + jets and Z + jets events in real data and simulations using the quantity, p_T imbalance, defined as

$$\Delta S \equiv \frac{p_T^{\rm jet} - p_T^{\gamma/Z}}{p_T^{\gamma/Z}}. \tag{5.5}$$

The difference $D = \langle \Delta S \rangle_{\rm data} - \langle \Delta S \rangle_{\rm MC}$ provides the desired relative jet energy scale and is used to bring the jets in data and MC at the same level as far as the energy measurement is concerned.

5.6 Missing Transverse Energy

The colliding partons inside the proton and anti-proton carry a fraction of the momentum of the parent hadron which mostly lies along the $|z|$ direction, while there is very little momentum in the xy-plane. The net momentum in the plane transverse to the beam direction can therefore be assumed to be zero. A net imbalance in the transverse energy deposited in the calorimeter is known as "missing transverse energy" or missing E_T and is denoted as $\not\!\!E_T$.

Missing E_T is calculated using all cells in the calorimeter with positive energy . First the x and y components of the visible energy are calculated using

$$E_{\rm vis}^{\rm x,y} = \sum_{\rm cells} E_i^{\rm x,y}. \tag{5.6}$$

The missing energy components are taken to be the negative of the quantities determined above i.e.

$$\not\!\!E_T^{\rm x} = -E_{\rm vis}^{\rm x} \; ; \; \not\!\!E_T^{\rm y} = -E_{\rm vis}^{\rm y}. \tag{5.7}$$

The resultant $\not\!\!E_T$ is then given by

$$\not\!\!E_T = \sqrt{(\not\!\!E_T^{\rm x})^2 + (\not\!\!E_T^{\rm y})^2}. \tag{5.8}$$

Since a muon produced in the event will not deposit its energy in the calorimeter, the $\not\!\!E_T$ should be corrected for the presence of muon. Other important corrections applied to the $\not\!\!E_T$ are the JES and JSSR corrections, since they change the energy of the jet which in turn affects the calculations of $\not\!\!E_T$ in the event.

I

Chapter 6

Data and Simulated Samples

This chapter describes the details of how MC samples for background and signal estimation are generated and reconstructed. The details of data sample along with the trigger requirements used to collect the data are also presented.

6.1 Simulated Samples

In order to be able to extract results from what is observed in real data collected in $p\bar{p}$ collisions, we need to compare the observed results with the expectations determined from a particular model. For this purpose simulated samples are used that are described in detail below.
The complete description of simulated events requires the following steps to be filled in

- Generation.
- Simulation.
- Reconstruction.

6.1.1 Generation of Events

The computational methods based on repeated generation of pseudo-random numbers to compute some results are known as Monte Carlo (MC) programs. The methods define a particular set of domain of relevant parameters and generate random events to perform computations. A larger

fraction of the MC samples used to evaluate the expected contributions are generated using ALPGEN v2.05 [58] interfaced with PYTHIA v6.323 [59]. ALPGEN is a leading order generator for hard multiparton processes in hadron collisions while PYTHIA is used to incorporate the showering effects. By showering one means to take into account the effect that a parton in initial or final state have enough energy to radiate off a gluon. The gluon produces a quark and an anti-quark pair which are reconstructed as jets later on. In $p\bar{p}$ collisions only partons inside a proton or anti-proton interact. These partons carry a certain fraction of the momentum of the proton or anti-proton. The probability of finding a parton inside proton with a certain momentum fraction is described by the parton distribution functions (PDFs). In the simulated samples the PDF set CTEQ6L1 [60, 61] are used.

In the first step of generation, the required parton-level configuration for a given hard-parton multiplicity is generated using ALPGEN. The partons are generated with the p_T above a certain threshold, and the angular separation between two partons is required to be larger than a minimum separation. In the next step the generated events are fed in PYTHIA generator, which performs the jet showering. These processed events, before hadronization, are passed through a step that creates jets defined by a minimum transverse energy and a particular cone size. The next step includes matching the reconstructed jets with the generated hard partons. This procedure is known as MLM matching. Each hard parton is said to be matched to a jet if ΔR between jet and parton is smaller than the radius of the cone that was used to form the jet. If the number of jets found in the event is exactly equal to the number of hard partons and all jets are matched to generated hard partons, the sample is named as "exclusive" sample. If on the other hand the number of jets is larger than the number of hard partons, and the unmatched jet is softer than all matched jets, the composing sample is called an "inclusive" sample. In the analysis both exclusive and inclusive samples are used.

6.1.2 Simulation

At the D0, the full simulation [62] of generated events is done using computer programes called D0Gstar [63] and D0Sim [64]. D0Gstar is a GEANT [65] based full simulation of the Run II D0 detector response and is used to determine how much energy is deposited in the active areas of the detector. D0Sim does the electronics simulation. The effects of the pileup and additional minimum bias interactions that occur in the same bunch crossing are incorporated by overlaying the simulated events with the real data events recorded with unbiased beam crossings.

6.1.3 Reconstruction

The reconstruction procedure takes the simulated events as input and reconstructs all physics objects like electrons, muons, jets, PV and $\not\!\!E_T$ exactly in the same way as in real data. This is done using the package called D0Reco [66]. The events are now at a stage where they can be analyzed and predicted results can be compared with the observation in the data.

6.2 SM Background Samples

The $\tilde{t}_1$ signal has a topology of events with two jets and missing transverse energy. Other processes having the same event topology can mimic the signal. These processes are described below.

- **Vector bosons ($W^{\pm}$, Z^o) production in association with jets**. These processes arise when along with a vector boson production, a parton in the initial state emits a gluon, which afterwards creates a quark anti-quark pair to be reconstructed as two jets. If the charged leptons coming from the $W^{\pm}$ or Z^o boson decays are not reconstructed, the event will have only jets and $\not\!\!E_T$ in the final state. The MC samples for these processes are generated with ALPGEN (for generation of bosons and jets) interfaced with PYTHIA (for showering and hadronization). The samples include the following decay modes of $W^{\pm}$ and Z^o bosons.

  $W(\rightarrow \ell\nu)$ + jets, where $\ell = e, \mu, \tau$ and jets include only the light flavors i.e. u, d, s, g.

  $W(\rightarrow \ell\nu) + b\bar{b}$.

$W(\rightarrow \ell\nu) + c\bar{c}$.

$Z(\rightarrow \ell\bar{\ell})$+jets, where $\ell\bar{\ell} = e^+e^-,\ \mu^+\mu^-,\ \tau^+\tau^-,\ \nu\bar{\nu}$.

$Z(\rightarrow \ell\bar{\ell}) + b\bar{b}$.

$Z(\rightarrow \ell\bar{\ell}) + c\bar{c}$.

Feynman diagrams for these processes are shown in Fig. 6.1. MC samples for these processes are generated separately for each jet multiplicity bin as explained in Sec. 6.1.1. Table 6.1 and 6.2 show the leading order (LO) cross sections calculated using ALPGEN, the ratio of the cross section at next to leading order (NLO) to that at LO (also known as K factor) using MCFM [67], and the generated luminosity of each sample. The samples for $W^{\pm}$ bosons are generated inclusively for all leptonic decay modes while those for Z bosons are generated separately for each leptonic decay mode.

- **Diboson production**. The diboson samples are simulated with PYTHIA and include production of WW, WZ and ZZ pairs. In the WW sample when one W boson decays hadronically and other leptonically and the lepton in the event is not identified, it will look exactly like a signal event having only jets and $\not\!\!E_T$ in the final state. In the WZ sample, when W boson decays hadronically and Z boson decays into neutrinos, the signature will mimic the signal. In the ZZ samples, when one Z boson decays into hadrons and other into neutrinos, it will exactly look like a signal event. Feynman diagrams for these processes are shown in Fig. 6.2 while the generated samples, cross sections, K factors and luminosity for each sample are shown in Table 6.3.

- **Top pair production**. Samples of top pair production are also simulated with ALPGEN interfaced with PYTHIA. The top quark decays into a b quark and a W boson almost 100% of the time. Below are three different topologies depending on whether both W bosons decay hadronically, leptonicaly or one decays into leptons and other into hadrons.

  $t\bar{t} \rightarrow b\bar{b}$ + jets.

  $t\bar{t} \rightarrow b\bar{b}\ \ell\nu\ \ell\nu$.

$t\bar{t} \rightarrow b\bar{b}\,\ell\nu$ + jets.

Feynman diagrams for these processes are shown in Fig. 6.3. Whereas Table 6.4 shows the generated samples, cross sections, K factors and the luminosity for each sample.

- **Single top production**. A single top quark produced in s or t channel can contribute to backgrounds for $\tilde{t}_1$ search. COMPHEP [68] was used to generate simulated samples for single top processes. Feynman diagrams for these processes are shown in Fig. 6.4 and the generated samples, cross sections, K factors and luminosity for each sample are shown in Table 6.5.

6.3 Data Sample

The data used in this analysis were collected with the D0 detector during Run IIa (April 2003 to February 2006) of Tevatron and corresponds to approximately 1.2 fb^{-1} of luminosity. To have reasonable size, data were skimmed using the definition for 'NP' skim, which basically requires that the event must have fired one of the two triggers, MHT30_3CJT5 or JT1_ACO_MHT_HT. This skim contains about 58 million events. The MHT30_3CJT5 and JT1_ACO_MHT_HT triggers are specifically designed to study jets and $\not\!\!E_T$ topologies [69]. The analyzed data were collected using different versions of trigger list. MHT30_3CJT5 trigger was used to collect data from April 2003 to June 2004 with trigger list versions v11 and v12. The conditions imposed at different levels of trigger system are described below.

- **Level 1**: CJT(3,5), which means that there should be at least three calorimeter trigger towers with energy larger than 5 GeV.
- **Level 2**: $\not\!\!H_T > 20$ GeV. The $\not\!\!H_T$ is defined as the vector sum of the p_T of all jets i.e. $\not\!\!H_T = |\sum_{\text{jets}} \vec{p}_T|$.
- **Level 3**: $\not\!\!H_T > 30$ GeV.

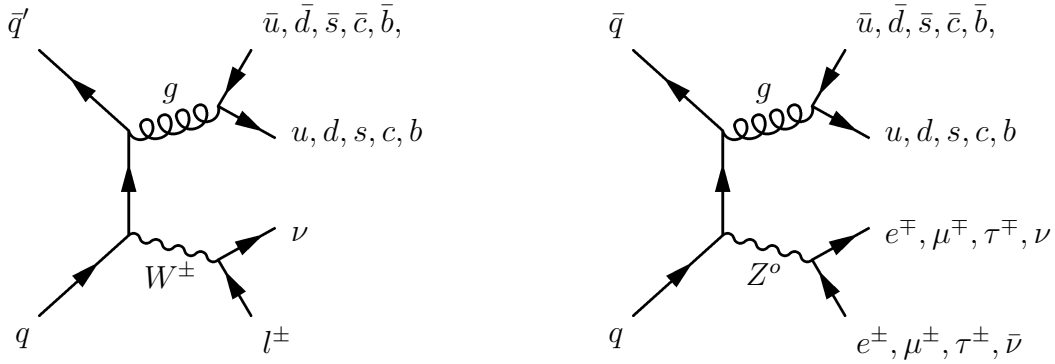

Figure 6.1: Feynman diagrams for W, Z bosons +jets background processes.

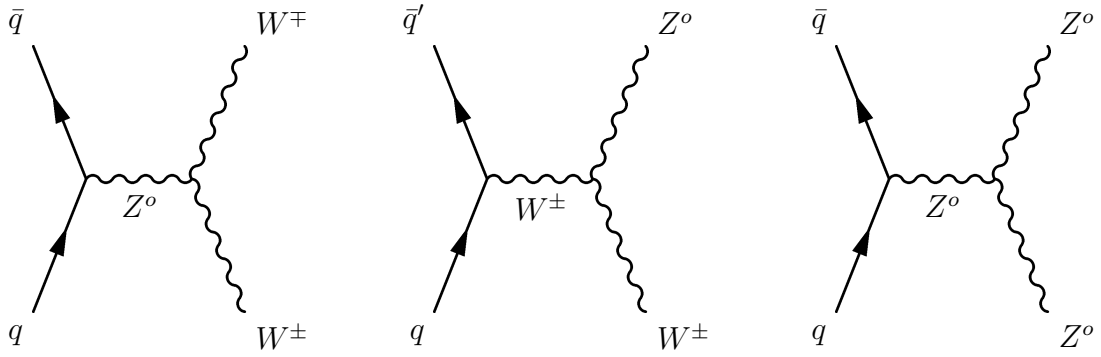

Figure 6.2: Feynman diagrams for diboson production.

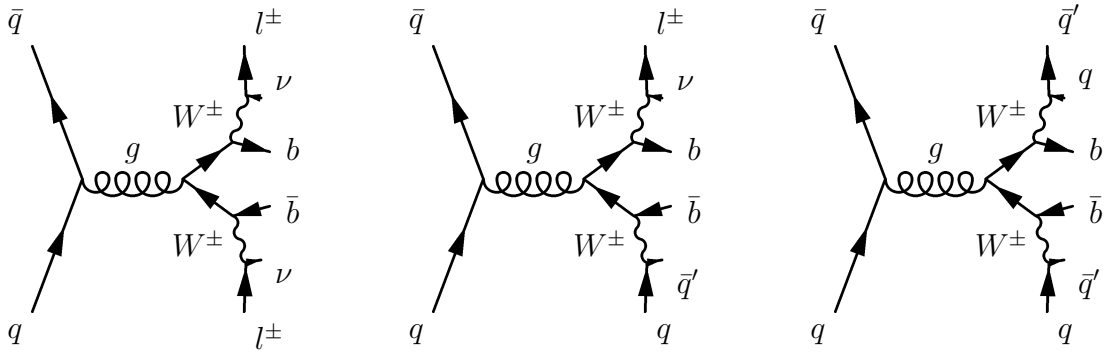

Figure 6.3: Feynman diagrams for top pair production along with the all leptonic, lepton+jets and all hadronic decay modes of W bososn.

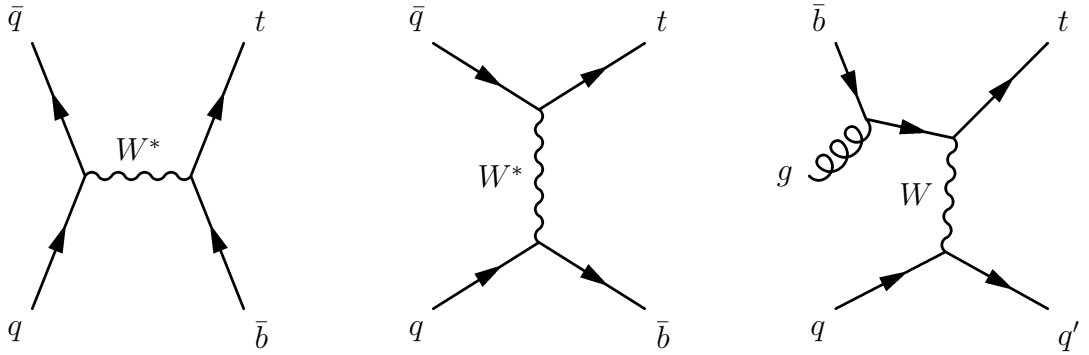

Figure 6.4: Feynman diagrams for single top production in s and t channels.

SM Process	σ_{LO} [pb]	k factor	Luminosity [pb^{-1}]
Z (e^+e^-) + 0 lp exclusive	139.2	1.23	6104
Z (e^+e^-) + 1 lp exclusive	41.6	1.23	4248
Z (e^+e^-) + 2 lp exclusive	9.7	1.23	8580
Z (e^+e^-) + 3 lp inclusive	3.2	1.23	24156
Z (e^+e^-) + $b\bar{b}$ + 0 lp exclusive	0.9	1.35	255857
Z (e^+e^-) + $b\bar{b}$ + 1 lp exclusive	0.4	1.35	119345
Z (e^+e^-) + $b\bar{b}$ + 2 lp inclusive	0.2	1.35	103510
Z (e^+e^-) + $c\bar{c}$ + 0 lp exclusive	3.1	1.35	15242
Z (e^+e^-) + $c\bar{c}$ + 1 lp exclusive	1.1	1.35	39000
Z (e^+e^-) + $c\bar{c}$ + 2 lp inclusive	0.6	1.35	36535
Z ($\mu^+\mu^-$) + 0 lp exclusive	139.2	1.23	7073
Z ($\mu^+\mu^-$) + 1 lp exclusive	41.6	1.23	4752
Z ($\mu^+\mu^-$) + 2 lp exclusive	9.7	1.23	9643
Z ($\mu^+\mu^-$) + 3 lp inclusive	3.2	1.23	27022
Z ($\mu^+\mu^-$) + $b\bar{b}$ + 0 lp exclusive	0.9	1.35	269649
Z ($\mu^+\mu^-$) + $b\bar{b}$ + 1 lp exclusive	0.4	1.35	133478
Z ($\mu^+\mu^-$) + $b\bar{b}$ + 2 lp inclusive	0.2	1.35	102986
Z ($\mu^+\mu^-$) + $c\bar{c}$ + 0 lp exclusive	3.1	1.35	15450
Z ($\mu^+\mu^-$) + $c\bar{c}$ + 1 lp exclusive	1.1	1.35	40354
Z ($\mu^+\mu^-$) + $c\bar{c}$ + 2 lp inclusive	0.6	1.35	39520
Z ($\nu\bar{\nu}$) + 0 lp exclusive	816.0	1.23	906
Z ($\nu\bar{\nu}$) + 1 lp exclusive	243.0	1.23	5054
Z ($\nu\bar{\nu}$) + 2 lp exclusive	59.6	1.23	4058
Z ($\nu\bar{\nu}$) + 3 lp exclusive	14.3	1.23	5337
Z ($\nu\bar{\nu}$) + 4 lp exclusive	3.2	1.23	28709
Z ($\nu\bar{\nu}$) + 5 lp inclusive	0.8	1.23	93895
Z ($\nu\bar{\nu}$) + $b\bar{b}$ + 0 lp exclusive	5.8	1.35	32869
Z ($\nu\bar{\nu}$) + $b\bar{b}$ + 1 lp exclusive	2.1	1.35	42024
Z ($\nu\bar{\nu}$) + $b\bar{b}$ + 2 lp inclusive	0.8	1.35	107838
Z ($\nu\bar{\nu}$) + $c\bar{c}$ + 0 lp exclusive	17.3	1.35	9831
Z ($\nu\bar{\nu}$) + $c\bar{c}$ + 1 lp exclusive	6.3	1.35	14125
Z ($\nu\bar{\nu}$) + $c\bar{c}$ + 2 lp inclusive	1.6	1.35	55668
Z ($\tau^+\tau^-$) + 0 lp exclusive	139.2	1.23	6234
Z ($\tau^+\tau^-$) + 1 lp exclusive	41.6	1.23	4640
Z ($\tau^+\tau^-$) + 2 lp exclusive	9.7	1.23	18349
Z ($\tau^+\tau^-$) + 3 lp inclusive	3.2	1.23	24329
Z ($\tau^+\tau^-$) + $b\bar{b}$ + 0 lp exclusive	0.9	1.35	93952
Z ($\tau^+\tau^-$) + $b\bar{b}$ + 1 lp exclusive	0.4	1.35	506628
Z ($\tau^+\tau^-$) + $b\bar{b}$ + 2 lp inclusive	0.2	1.35	413676
Z ($\tau^+\tau^-$) + $c\bar{c}$ + 0 lp exclusive	3.1	1.35	12883
Z ($\tau^+\tau^-$) + $c\bar{c}$ + 1 lp exclusive	1.1	1.35	41029
Z ($\tau^+\tau^-$) + $c\bar{c}$ + 2 lp inclusive	0.6	1.35	35474

Table 6.1: Leading order cross sections, K-factors and generated luminosities of MC samples for processes involving Z bosons and jet production. In the table, lp stands for light parton which include a jet having u, d, c, s quark or a gluon inside it.

SM Process	σ [pb]	k factor	Luminosity [pb^{-1}]
W ($\ell\nu$) + 0 lp exclusive	4605.0	1.4	490
W ($\ell\nu$) + 1 lp exclusive	1274.0	1.4	2162
W ($\ell\nu$) + 2 lp exclusive	303.0	1.4	5161
W ($\ell\nu$) + 3 lp exclusive	72.5	1.4	10883
W ($\ell\nu$) + 4 lp exclusive	16.4	1.4	47470
W ($\ell\nu$) + 5 lp inclusive	2.2	1.4	26593
W ($\ell\nu$) + $b\bar{b}$ + 0 lp exclusive	19.2	2.1	38517
W ($\ell\nu$) + $b\bar{b}$ + 1 lp exclusive	8.0	2.1	32785
W ($\ell\nu$) + $b\bar{b}$ + 2 lp exclusive	2.7	2.1	64198
W ($\ell\nu$) + $b\bar{b}$ + 3 lp inclusive	1.8	2.1	91951
W ($\ell\nu$) + $c\bar{c}$ + 0 lp exclusive	71.8	2.1	6705
W ($\ell\nu$) + $c\bar{c}$ + 1 lp exclusive	29.7	2.1	11326
W ($\ell\nu$) + $c\bar{c}$ + 2 lp exclusive	9.5	2.1	34894
W ($\ell\nu$) + $c\bar{c}$ + 3 lp inclusive	4.5	2.1	82721

Table 6.2: Leading order cross sections, K-factors and generated luminosities of MC samples for processes involving W bosons and jet production. In the table, lp stands for light parton which include a jet having u, d, c, s quark or a gluon inside it.

SM Process	σ [pb]	k factor	Luminosity [pb^{-1}]
WW	11.5	1	40474
WZ	3.7	1	23649
ZZ	1.6	1	61203

Table 6.3: Leading order cross sections, K-factors and generated luminosities of MC samples for processes involving diboson production.

SM Process	σ [pb]	k factor	Luminosity [pb^{-1}]
$t\bar{t}$ ($\ell\nu$ jj) + 0 lp exclusive	1.30	1.33	354218
$t\bar{t}$ ($\ell\nu$ jj) + 1 lp exclusive	0.54	1.33	975824
$t\bar{t}$ ($\ell\nu$ jj) + 2 lp inclusive	0.40	1.33	1070960
$t\bar{t}$ ($\ell\nu$ $\ell\nu$) + 0 lp exclusive	0.32	1.33	1299600
$t\bar{t}$ ($\ell\nu$ $\ell\nu$) + 1 lp exclusive	0.14	1.33	2802200
$t\bar{t}$ ($\ell\nu$ $\ell\nu$) + 2 lp inclusive	0.10	1.33	4752420

Table 6.4: Leading order cross sections, K-factors and generated luminosities of MC samples for processes involving top pair production. In the table, lp stands for light parton which include a jet having u, d, c, s quark or a gluon inside it.

SM Process	σ [pb]	k factor	Luminosity [pb^{-1}]
tb alljet	0.675	1	137379
tb $(e\nu)$ bb	0.115	1	1228640
tb $(\mu\nu)$ bb	0.115	1	1096030
tb $(\tau\nu)$ bb	0.115	1	1178490
tqb all jet	1.621	1	465154
tqb $(e\nu)$ bqb	0.259	1	533788
tqb $(\mu\nu)$ bqb	0.259	1	513290
tqb $(\tau\nu)$ bqb	0.259	1	86803

Table 6.5: Leading order cross section, K-factor and generated luminosity of each MC sample for processes involving single top production. Different samples correspond to different decay modes of W boson that comes from top quark decay.

Trigger List	Trigger	Del. [pb^{-1}]	Rec. [pb^{-1}]	Good [pb^{-1}]
v11	MHT30_3CJT5	79.3	71.1	62.5
v12	MHT30_3CJT5	277.1	249.9	226.8
v13	JT1_ACO_MHT_HT	464.0	425.5	373.3
v14	JT1_ACO_MHT_HT	416.8	388.8	332.5

Table 6.6: For different trigger list version, details of delivered and recorded luminosities. The values corresponding to "Good" are after removing bad quality data.

In v13 of the trigger list, MHT30_3CJT5 was replaced by JT1_ACO_MHT_HT. Below are the requirements for this trigger at L1, L2, and L3.

- **Level 1**: Three calorimeter trigger towers with $E_T > 5$ GeV.
- **Level 2**: $\not\!\!E_T > 20$ GeV and the two jets with highest E_T values are required to be separated in ϕ by $0 < \phi(j_1, j_2) < 168.75°$ i.e. they are not back to back.
- **Level 3**: There should be at least two jets, each with $E_T > 9$ GeV and angle separating the two leading jets should be between 0 and $170°$. The $\not\!\!H_T$ must be above 30 GeV and $H_T > 50$ GeV. H_T is defined as the scalar sum of the p_T of all jets that have $E_T > 9$ GeV i.e. $H_T = \sum_{\text{jets}} |\vec{p}_T|$.

In July 2005, due to the expected high luminosity, a few modifications were incorporated in the requirements of JT1_ACO_MHT_HT trigger. At L1 an additional requirement was made that three calorimeter trigger towers should have $E_T > 4$ GeV for $|\eta| < 2.6$. The requirements at L2 were left unchanged, while at L3 a new filter was added in order to reduce the rate, at which data are recorded, and the QCD background. The additional L3 condition required the separation between any jet and $\not\!\!H_T$ to be larger than $25°$ and less than $180°$.

The recorded data may contain bad quality data due to the failure of any of the subsystems. Before analyzing the data, for each run, the response of each sub-detector system is required to be well

defined. A good normalizable data set is defined after removing all bad quality data. In this analysis, all data are checked not only on run by run but also on event by event basis to remove any events in which $\not\!\!E_T$ can be an artifact of noise in the calorimeter or any other part of the detector. The details of the luminosity delivered to D0 by Tevatron, the luminosity recorded by D0 and the luminosity of good data set for different trigger list versions are given in Table 6.6.

Since the data analyzed in this search was collected using particular triggers, therefore before comparing any results in data with the prediction calculated from MC, we need to fold in the trigger effects in MC in order to remove any biases seen in data. For this purpose a trigger parametrization, derived from data, was used [70]. The parametrization is derived using simulations at L1, which basically tells the probability that a jet may fire a certain number of trigger towers with given threshold. Offline reconstructed jets were used to simulate L2 and L3 conditions. The overall trigger efficiency for different signal samples ranges between 41% - 58% before applying any analysis requirements, in agreement with the expectations of the design of the trigger [69].

6.4 Simulated Samples for $\tilde{t}_1$ Signal

In the mass region of interest probed in this analysis, $\tilde{t}_1$ is allowed to decay only into a charm quark and a neutralino. Signal samples for this process were generated using PYTHIA v6.323 with CTEQ6L1 parton density functions. The only parameters allowed to vary were $\tilde{t}_1$ and $\tilde{\chi}_1^0$ masses while other parameters were fixed in the MSSM by the requirement, $\tan\beta = 25$. Masses of squarks other than $\tilde{t}_1$ were set to $M_{\tilde{q}}$= 1000 GeV. The Higgsino mass μ was taken to be 1000 GeV and the $\tilde{t}_1$ mixing parameter was set to 0.6. The practical impact of these parameter setting was simply to "turn off" all other $\tilde{t}_1$ decay channels except $\tilde{t}_1 \rightarrow c\tilde{\chi}_1^0$. The full detector simulation was performed using d0gstar, d0sim and d0reco as in the case of background MC samples. Data events recorded with unbiased beam crosses were overlaid to incorporate the effects of multiple interactions.

Figure 6.5 shows the generated samples in $\tilde{t}_1 - \tilde{\chi}_1^0$ mass plane while Table 6.7 shows the generated luminosity for each sample used in this analysis.

$m_{\tilde{t}_1}$ [GeV]	$m_{\tilde{\chi}_1^0}$ [GeV]	Lumi. [pb^{-1}]	$m_{\tilde{t}_1}$ [GeV]	$m_{\tilde{\chi}_1^0}$ [GeV]	Lumi. [pb^{-1}]	$m_{\tilde{t}_1}$ [GeV]	$m_{\tilde{\chi}_1^0}$ [GeV]	Lumi. [pb^{-1}]
95	45	470	135	50	1686	145	80	4910
95	50	342	135	60	3525	145	90	4919
95	55	512	135	65	3379	145	100	4901
95	75	426	135	70	3372	150	50	6566
100	45	650	135	75	2611	150	60	6003
100	55	680	135	80	3694	150	70	6838
100	60	595	135	85	3532	150	80	6291
100	70	595	135	90	3529	150	90	6857
110	50	1059	140	50	4554	150	100	6866
110	60	962	140	55	4363	155	55	8304
110	65	821	140	60	4369	155	75	8313
110	75	768	140	70	4550	155	85	7938
120	50	1807	140	75	4369	155	95	5850
120	60	1727	140	80	4174	160	65	9179
120	65	1414	140	85	4559	160	70	10002
120	75	1726	140	90	437	160	75	10003
130	50	2971	145	50	5595	160	80	10015
130	60	2972	145	60	5384	160	85	9168
130	65	2844	145	65	4908	165	55	12076
130	70	2600	145	70	5367	165	75	9577
130	80	2842	145	75	4920	165	95	11582

Table 6.7: Signal MC samples and corresponding generated luminosities, for different $\tilde{t}_1^0$ and $\tilde{\chi}_1^0$ masses, used in this analysis.

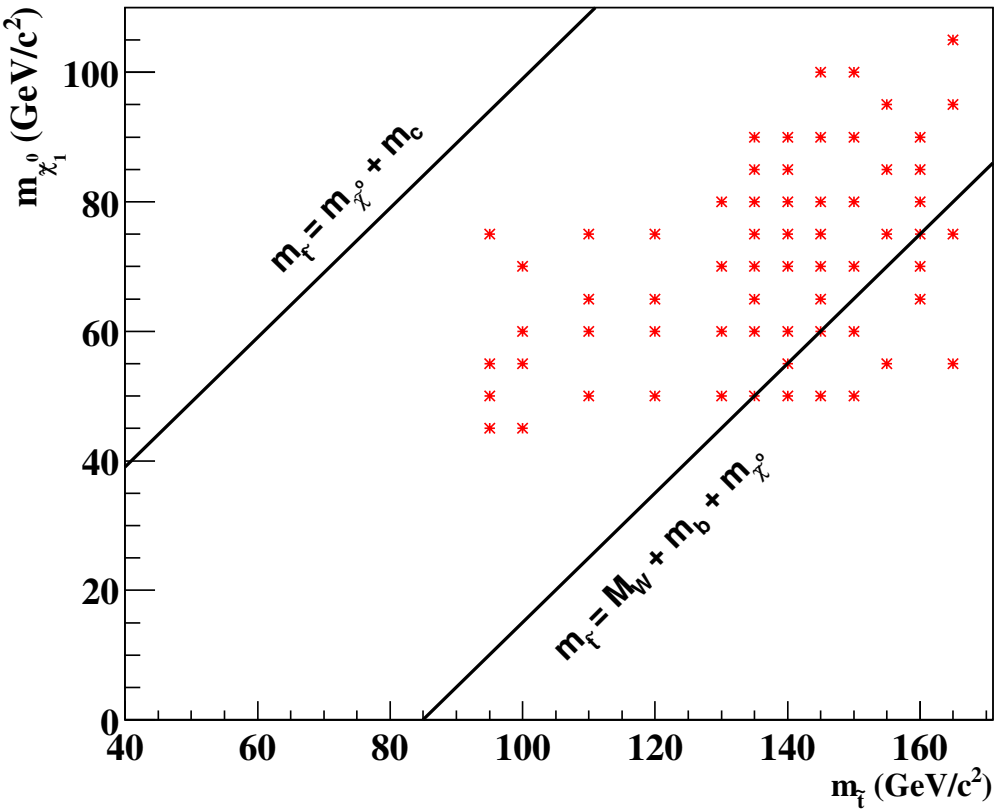

Figure 6.5: Simulated signal samples for different $\tilde{t}_1$ and neutralino masses used in the analysis.

Chapter 7

$Z/\gamma^*(\rightarrow e^+e^-)$ + jets Study for Background Normalization in $\tilde{t}_1$ Search

7.1 Introduction

The analysis presented in this thesis is a search for supersymmetric top quark production via the process $p\bar{p} \rightarrow \tilde{t}_1\bar{\tilde{t}}_1$. This produces a final state with two charm jets and $\not\!\!E_T$. The result, based on the full 1.2 fb $^{-1}$ Run IIa dataset, improves upon the 0.3 fb $^{-1}$ D0 publication [39] both through higher statistics and a use of a new method to reduce the systematic errors associated with the dominant vector boson +jets ("V+jets") backgrounds. The new method essentially amounts to normalizing the ("V+jets") contributions to a control sample of $Z/\gamma^*(\rightarrow e^+e^-)$ + jets events collected over the same data taking period.

SM V+jets processes dominate the backgrounds in $\tilde{t}_1$ search. Consider the particular process $p\bar{p} \rightarrow V + J$, with $V \rightarrow \ell\ell'$ a leptonic decay of the V, where ℓ, ℓ' can be charged leptons or neutrinos, and J a particular configuration of jets. Abbreviate this as $V\,(\ell\ell') + J$; with $J = lp\,(n)$, $J = c\bar{c}\,(n)$, and $J = b\bar{b}\,(n)$ denoting n light parton jets, n jets from a $c\bar{c}$ pair plus light partons, or n jets from a $b\bar{b}$ pair plus light partons, respectively. Single charm production via the $W + c+$ light parton final state falls in the category $J = lp\,(n)$ (i.e., the charm quark is treated as a light quark for this process); and the single heavy flavor processes Wb, Zc, and Zb are not included.

The most straightforward expression for the predicted contribution of a $V\,(\ell\ell') + J$ final state from

a given vector boson p_T to the search, $N^{\rm PRE}_{V(\ell\ell')+J}$, is then

$$N^{\rm PRE}_{V(\ell\ell')+J} = \mathcal{L}\ \sigma_{V(\ell\ell')+J}\ \epsilon_{V(\ell\ell')+J}, \tag{7.1}$$

with $\mathcal{L}$ the luminosity, $\sigma_{V(\ell\ell')+J}$ the cross section for $V\,(\ell\ell') + J$ in a particular vector boson p_T bin, and $\epsilon_{V(\ell\ell')+J}$ the acceptance$\times$efficiency for $V\,(\ell\ell') + J$ to pass the $\tilde{t}_1$ analysis cuts. A contribution estimated this way will be defined to be *absolutely normalized*. The technical issues with absolute normalization are the three factors that make up the prediction. Of these, the efficiency $\epsilon_{V(\ell\ell')+J}$ can be computed from full MC simulations augmented by usual D0 data-to-MC corrections. Typical acceptance$\times$efficiency uncertainties are on the order of a few percent. From work by the D0 luminosity group, $\mathcal{L}$ is known to 6.1%. The cross section $\sigma_{V(\ell\ell')+J}$ is the least known of the factors. ALPGEN is currently the best tool that can be used to estimate contributions to specific final states, but ALPGEN only provides leading order cross section estimates. Unmodified ALPGEN cross sections will be denoted $\sigma^{\rm ALP,O}_{V(\ell\ell')+J}$. Getting ALPGEN predictions to agree with data requires at least two corrections:

- Multiplication by K factor. The K factors are assumed to be independent of n, the light parton final multiplicity, but are allowed to be different for $V = W$ or Z, and for the presence of $c\bar{c}$ or $b\bar{b}$ in the final state. The factors K_V apply to $V\,(\ell\ell') + lp\,(n)$, and the factors K'_V apply to $V\,(\ell\ell') + c\bar{c}\,(n)$ and $V\,(\ell\ell') + b\bar{b}\,(n)$. The nominal values currently used for ALPGEN in D0 are $K_Z = 1.23$, $K'_Z = 1.35$, $K_W = 1.40$, and $K'_W = 2.10$. These $K-$factor have not been well-measured, and estimates for their uncertainties are likely ad-hoc.

- Adjusting the vector boson p_T distribution. ALPGEN cannot completely describe the p_T spectrum of Z bosons for $p_T \lesssim 40$ GeV which will be discussed in detail in this chapter.

The procedure adopted to handle the limitations of ALPGEN is to use $Z/\gamma^*(\rightarrow ee)$+jets data to develop a re-weighting function for ALPGEN that forces the Z p_T distribution to agree between MC and data. This re-weighting is constructed to preserve the normalization of the total cross section;

the p_T-re-weighted cross sections will be designated by the replacement $\sigma^{\mathrm{ALP,O}}_{V(\ell\ell')+J} \rightarrow \sigma^{\mathrm{ALP}}_{V(\ell\ell')+J}$. The number of observed $Z/\gamma^*(\rightarrow ee)+$ jets events is then employed to force the normalization of ALPGEN to agree with data, at least for this channel, in each jet multiplicity bin. Other $V+$jets contributions are then normalized to $Z/\gamma^*(\rightarrow ee)+$jets. The combined re-weighting will be referred to as the $Z/\gamma^*(\rightarrow ee)+$*jets normalization*. Ideally this procedure replaces the combined luminosity and ALPGEN cross section uncertainties on $\mathcal{L}\sigma_{V(\ell\ell')+J}$ with the statistical error on the number of $Z/\gamma^*(\rightarrow ee)+$jets in the data.

7.2 $Z/\gamma^*(\rightarrow e^+e^-)$ + jets

7.2.1 Data Sample

The data used for this study were collected with the D0 detector during the same data taking period as used for $\tilde{t}_1$ search. The particular skim used was 2EMhighpt. No trigger was specified in selecting events, creating a "Super-OR" of triggers. The trigger efficiency for high p_T dielectron events is expected to be very close to 100% [71]. An unprescaled[1] trigger JT125TT was used to determine the luminosity of the dataset. The normlizabale dataset after removing the bad quality data corresponds to an integrated luminosity of 1067 ± 65 pb^{-1}.

7.2.2 MC Samples

In order to compare the observed spectrum of different kinematical variables with the predicted spectrum, the MC samples for $Z/\gamma^*(\rightarrow e^+e^-)$+jets given in Table 6.1 were used.

7.2.3 Event Selection

In order to reconstruct a Z boson, events are required to have at least two electrons where electrons are identified using the criteria described in Sec. 5.3. The most energetic and the second most energetic electrons are required to have

- $p_T > 15$ GeV.

[1] Unprescaled means that the particular trigger is used to collect data at all luminosities.

- isolation < 0.20.
- Likelihood > 0.20.
- EMF > 0.90.
- $|\eta_{\rm det}| < 1$ (CC) or $|\eta_{\rm det}| < 2.5$ (EC).

where $|\eta_{\rm det}|$ is the jet pseudorapidity calculated using the assumption that the jet originates from the detector center. The invariant mass of the two electrons[2] is required to be between 65 and 115 GeV. This region of mass is later referred to as "Z peak". The MC contribution is estimated by normalizing the MC samples to the inclusive[3] number of events in the Z peak in data. The weight assigned to each MC sample is

$$w^{\rm MC}_{Z+n} = \frac{N^{\rm data}_{Z}}{N^{\rm MC}_{Z+n}} \times \frac{\sigma^{\rm ALP}_{Z+n}}{\sum_{k\geq 0}\sigma^{\rm ALP}_{Z+k}} \times \frac{\epsilon_{Z+n}}{\epsilon_{Z+X}}, \tag{7.2}$$

where $N^{\rm data}_{Z+{\rm n}}$ is the number of Z events found in data under the Z peak which is 83722. $N^{\rm MC}_{Z+n}$ is the number of simulated $Z/\gamma^*(\rightarrow e^+e^-) + n$ light parton jets events; $\sigma^{\rm ALP}_{Z+n}$ is the cross section predicted by ALPGEN for $Z/\gamma^*(\rightarrow e^+e^-) + n$ light parton jets as shown in Table 6.1. ϵ_{Z+n} and ϵ_{Z+X} are the corresponding detection efficiencies of observing a Z boson with n exclusive light partons or inclusive respectively. The inclusive efficiency for reconstructing Z is computed from MC by weighting over different multiplicity samples and is given by

$$\epsilon_{Z+{\rm X}} = \frac{\sum_{k\geq 0}\epsilon_{Z+{\rm k}}\,\sigma^{\rm ALP}_{Z+{\rm k}}}{\sum_{k\geq 0}\sigma^{\rm ALP}_{Z+{\rm k}}}. \tag{7.3}$$

The distribution of dielectron invariant mass is shown in Fig. 7.1 while the p_T spectrum of Z boson is shown in Fig. 7.2 for $0-30$ GeV range, while the full range on log scale in shown in Fig. 7.3.

[2]The invariant mass of two electrons that have energies $E^{(1)}$ and $E^{(2)}$ and momentum components $p_x^{(1)}, p_x^{(2)}, p_y^{(1)}, p_y^{(2)}, p_z^{(1)}, p_z^{(2)}$ is defined as

$$M^{ee}_{\rm inv} = \sqrt{E^2 - \mathbf{p^2}}$$

where $E = E^{(1)} + E^{(2)}$ and $\mathbf{p^2} = p_x^2 + p_y^2 + p_z^2$ with $p_i = p_i^{(1)} + p_i^{(2)}$ with $i = x, y, z$.

[3]By inclusive one means that there is no requirement on the minimum number of jets present in the event.

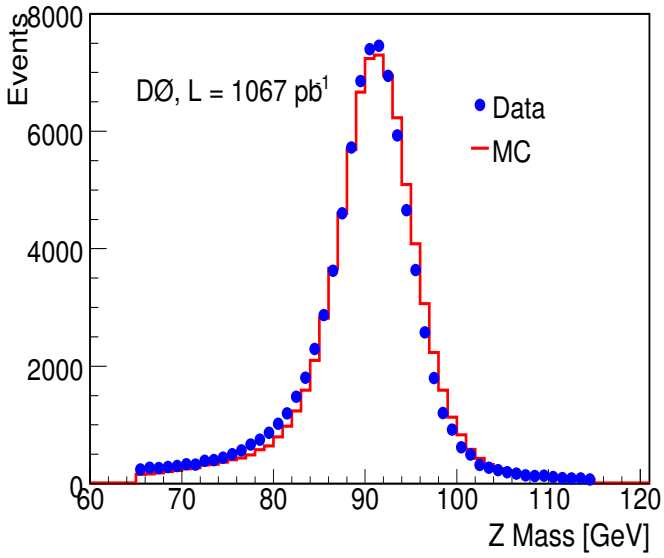

Figure 7.1: Distributions for dielectron invariant mass for inclusive sample.

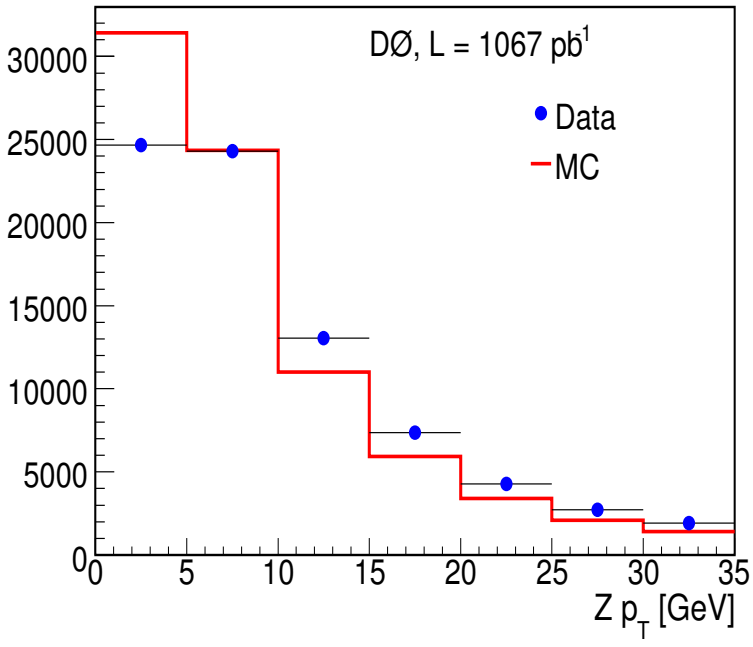

Figure 7.2: Distributions for p_T spectrum of Z boson for inclusive sample on linear scale from $0 - 30$ GeV.

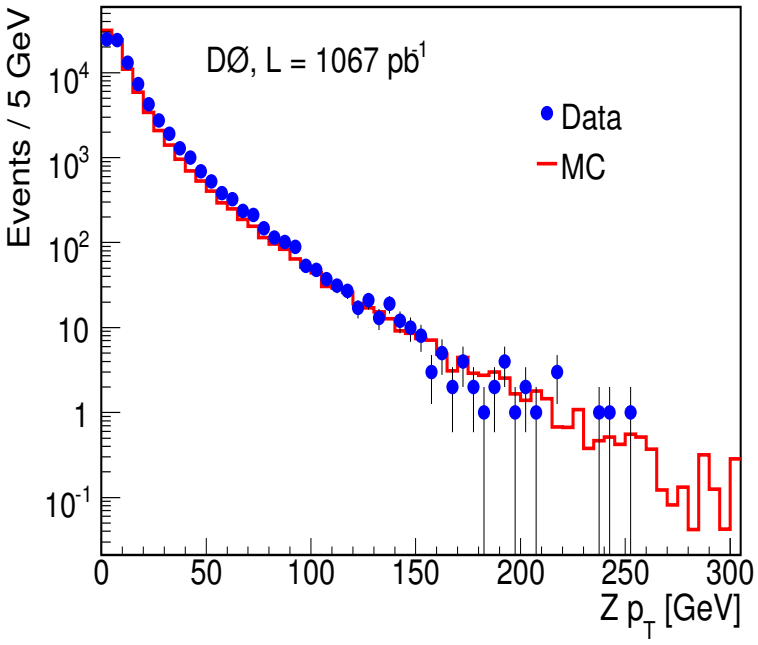

Figure 7.3: Distributions for p_T spectrum of Z boson for inclusive sample on log scale from $0 - 300$ GeV.

7.2.4 Z p_T Spectrum

It can be seen from Fig. 7.2 that the p_T spectrum of Z boson predicted by ALPGEN does not agree with the observed spectrum in data, particularly in the low p_T region. This effect is ascribed to multiple soft gluon radiation at low energies. There have been several techniques provided by theorists to include higher order corrections. These are called "re-summation" techniques. Among the many re-summation techniques, the CSS (Collins, Soper and Sterman) formalism [72] provides the best agreement with the experimental data. This technique was further developed by C. Balazs and C.P. Yuan by adding the effects of multiple soft gluon radiation on the distributions of leptons coming from the decay of Z bosons. The results were implemented into an event generator called RESBOS [73].

Using the electron decay mode of Z bosons, D0 has measured [74] the p_T spectrum of Z boson and compared it with the events generated with RESBOS. A good agreement is seen between the observed and predicted spectrum as shown in Fig. 7.4.

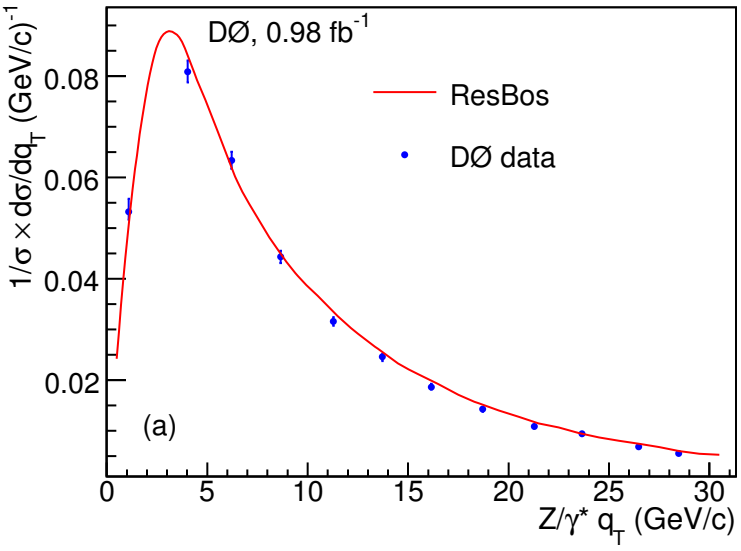

Figure 7.4: The normalized differential cross section as a function of Z boson p_T for inclusive sample. The points are the data and solid curve is the RESBOS prediction.

The effect of soft gluon radiation is not taken into account by the ALPGEN generator. Since all of the W and Z + jets samples to determine background for $\tilde{t}_1$ search were generated with ALPGEN and not RESBOS, we need to come up with a technique to fix the p_T of Z boson. This is an important variable and determines the kinematics of jets in events where Z boson is produced is association with jets. One such process is $Z(\rightarrow \nu\bar{\nu})$ + jets. In this process we need to extract all information from the kinematics of jets. This process turns out to be the second largest as well as irreducible background for $\tilde{t}_1$ search. A reweighting function is therefore derived in order to correct the Z boson p_T spectrum as described in next section.

7.2.5 Z Boson p_T Reweighting

In order to be able to match the p_T spectrum of Z boson predicted by ALPGEN with the one observed in data, the predicted spectrum was reweighted using a function determined from the ratio of Z boson p_T in data to that in prediction. In order to be able to apply this reweighting function to the $\tilde{t}_1$ search analysis, the reweighting function was derived not from the inclusive sample but from a sample that has a Z boson and exactly two jets with $p_T > 15$ GeV and $|\eta_{\rm det}| < 2.5$. In $\tilde{t}_1$ search exactly two jets with $p_T > 40, 20$ GeV and $|\eta_{\rm det}| < 1.5$ were required but

requirements in electron + jets channel are kept loose in order to have sufficient statistics. The jets were required to be well separated from electrons using the condition ΔR (jet, electron) > 0.5. The ratio of the Z boson p_T in data to that in prediction parametrized as a function of Z boson p_T is shown in Fig. 7.5. The parametrization shown in Fig. 7.5 was applied to the $Z/\gamma^*(\rightarrow ee) + 2$ jets sample and it was verified that all of the kinematical variables applicable to $\tilde{t}_1$ search were well described between data and MC. Some of the variables are shown in Figs. 7.6, 7.7 and 7.8. In all plots there is good agreement between data and MC. The same parametrization was carried over to the $\tilde{t}_1$ search analysis.

It is important to mention that in the $\tilde{t}_1$ search analysis, rather tighter cuts were imposed on the jets. It was made sure by applying the reweighting function derived above to a sample of $Z/\gamma^*(\rightarrow ee) + 2$ jets events with same cuts on jets as used in the $\tilde{t}_1$ search analysis and a good agreement between the predicted and observed p_T spectrum of Z boson was found. There were 458 events observed in a data set of $Z/\gamma^*(\rightarrow ee) + 2$ jets with ($p_T(j_1) > 40$ GeV, $p_T(j_2) > 20$ GeV, $|\eta|_{\rm det} < 1.5$). The 5% statistical uncertainty of this dataset was assigned to all background samples normalized using V+jets normalization in $\tilde{t}_1$ search.

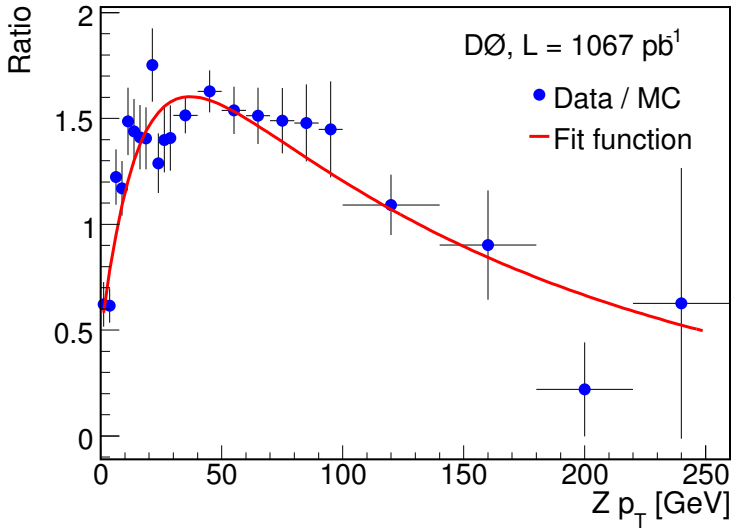

Figure 7.5: Distribution for the ratio of Z boson p_T in data to that in ALPGEN prediction as a function of Z boson p_T. Red line shows the fit function used to parametrize the ratio given by $f(p_T, a, b, c, d, g) = \left[a + b \times \left\{1 + \text{Erf}\left(\frac{p_T - c}{\sqrt{2}d}\right)\right\}\right] \times e^{-g\, p_T}$.

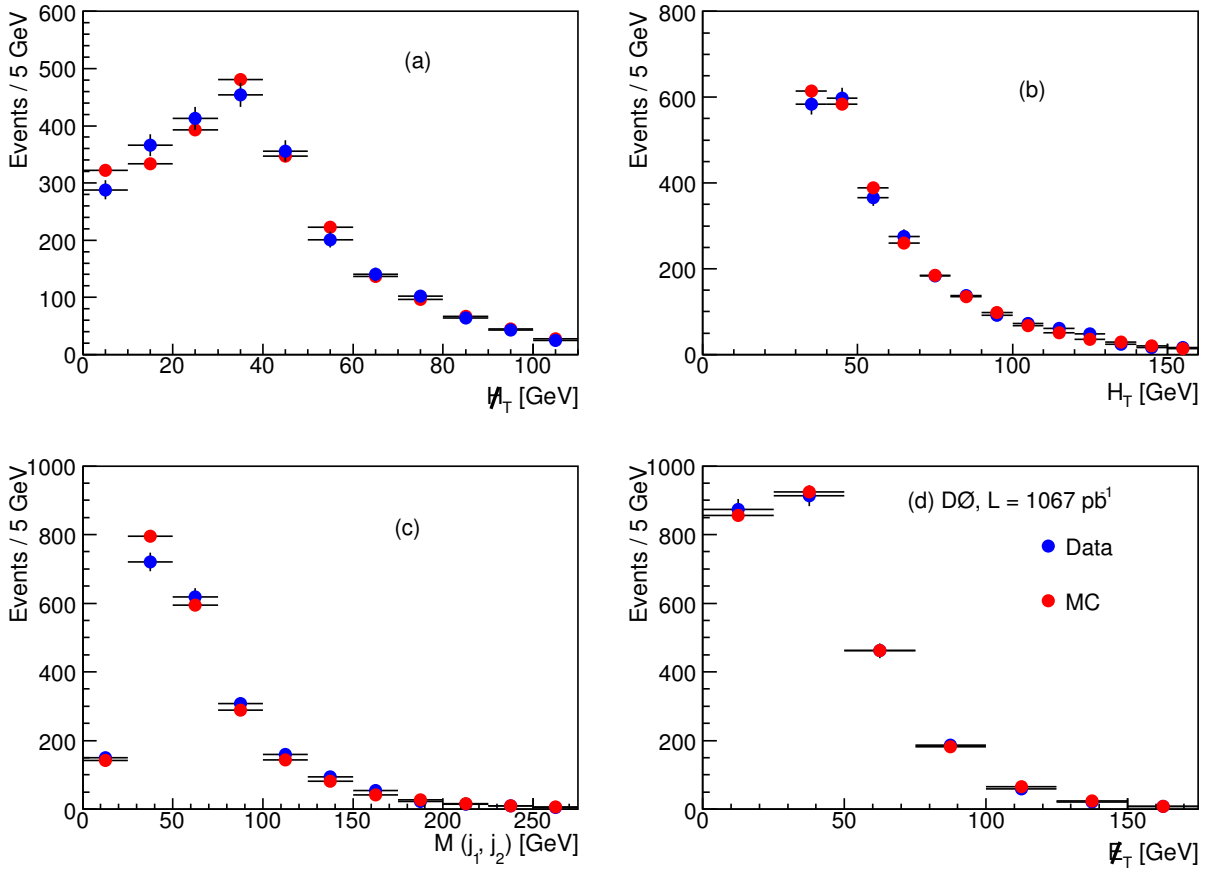

Figure 7.6: Distributions of $\not\!\!H_T$ (a), H_T (b), invariant mass of two jets (c) and $\not\!\!E_T$ (d), after applying Z boson p_T reweighting in the $Z/\gamma^*(\rightarrow e^+e^-) + 2$ jets sample.

7.3 QCD Background

In order to estimate QCD background in $Z/\gamma^*(\rightarrow e^+e^-)$ + jets events, the approximately exponential shape of the QCD background is determined from data by inverting the electron likelihood cut. The dielectron invariant mass in MC is fitted with a Breit-Wigner function convolved with a Gaussian to determine the total number of Z events. The Drell-Yan (DY) contribution, where an e^+e^- pair is produced by an off shell photon, is estimated by fitting the same mass peak with an exponential. The ratio of the number of DY to Z+DY events is determined from this fit. It is assumed that the ratio of DY to Z+DY in data is the same as in MC. Assuming this ratio, the

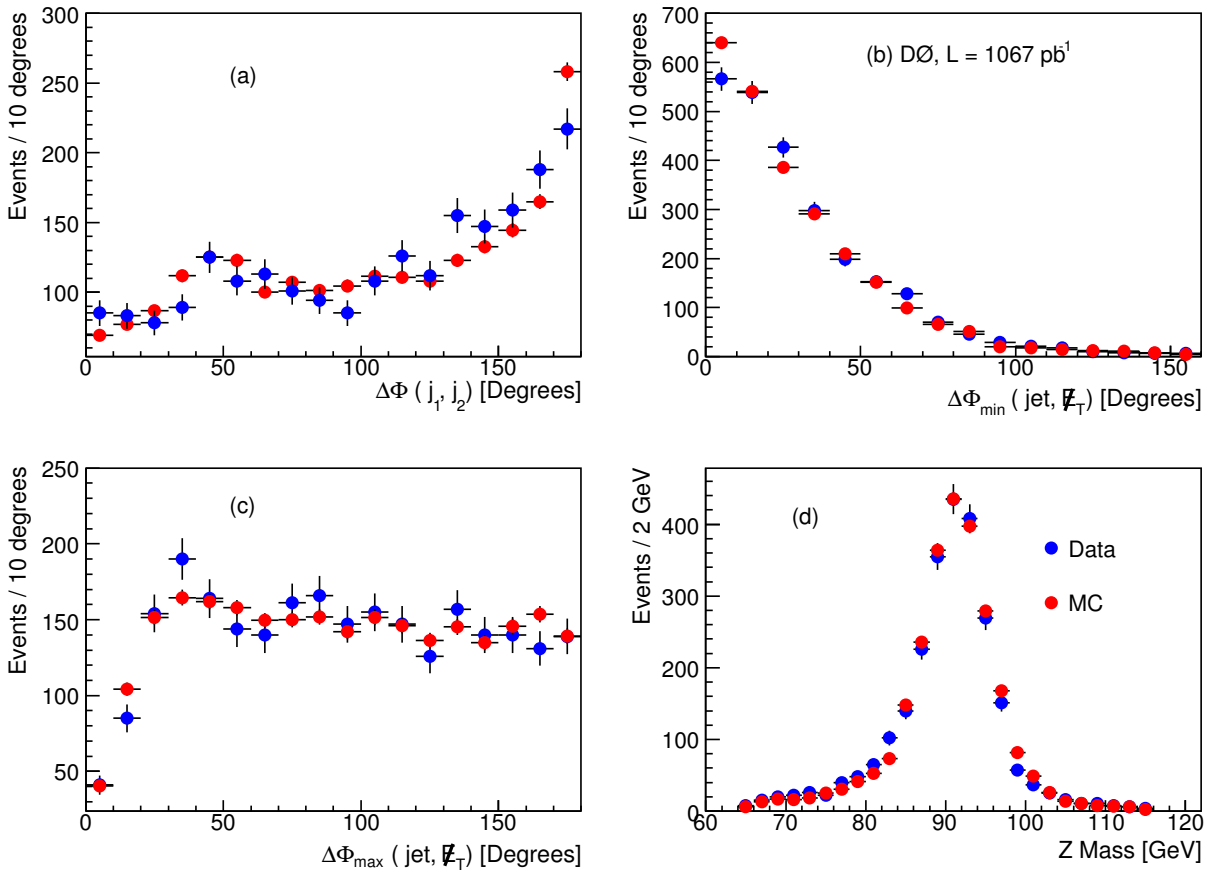

Figure 7.7: Distributions of angle between two jets (a), minimum angle between a jet and $\not\!\!E_T$ direction (b), maximum angle between a jet and $\not\!\!E_T$ direction (c) and invariant mass of two electrons (d), after applying Z boson p_T reweighting in the $Z/\gamma^*(\rightarrow e^+e^-) + 2$ jets sample.

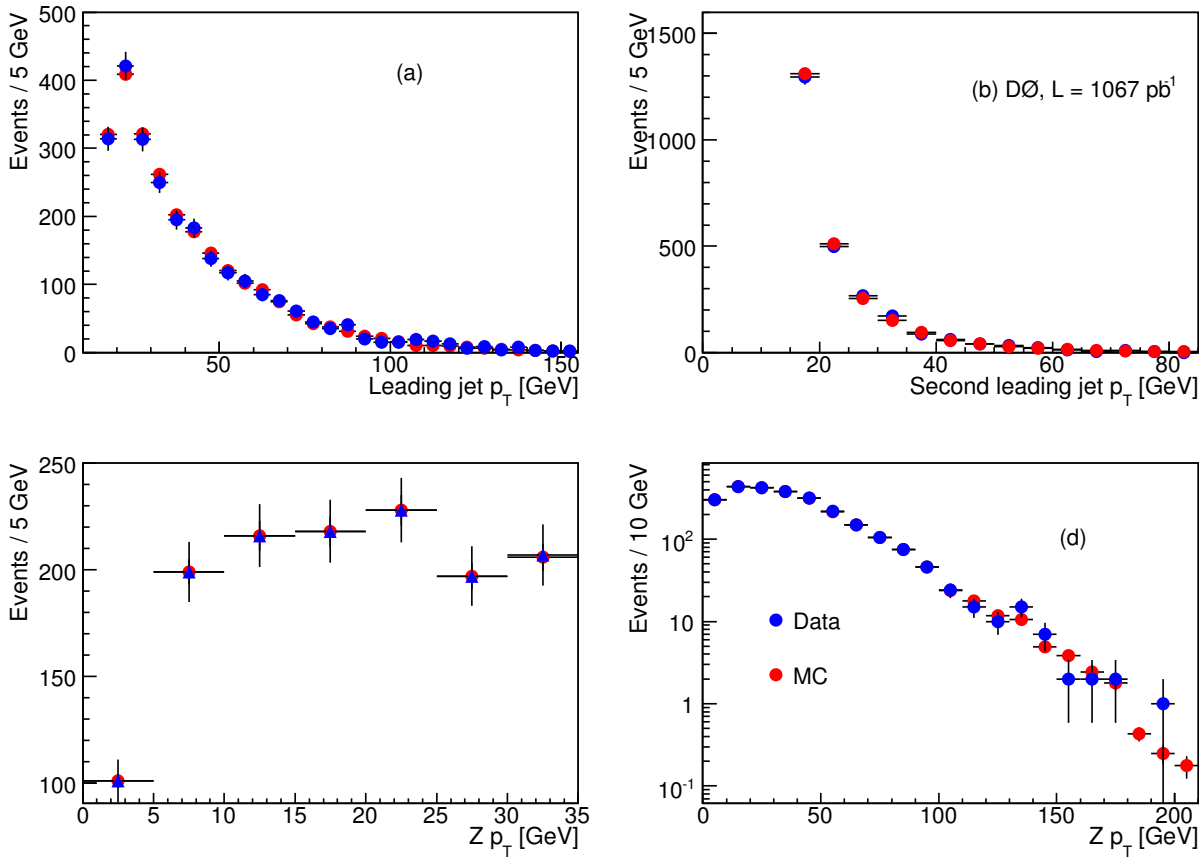

Figure 7.8: Distributions of leading jet p_T (a), second leading jet p_T (b), p_T of Z boson from $0-30$ GeV on linear scale (c) and p_T of Z boson from $0-200$ GeV on log scale (d), after applying Z boson p_T reweighting in the $Z/\gamma^*(\rightarrow e^+e^-)+2$ jets sample.

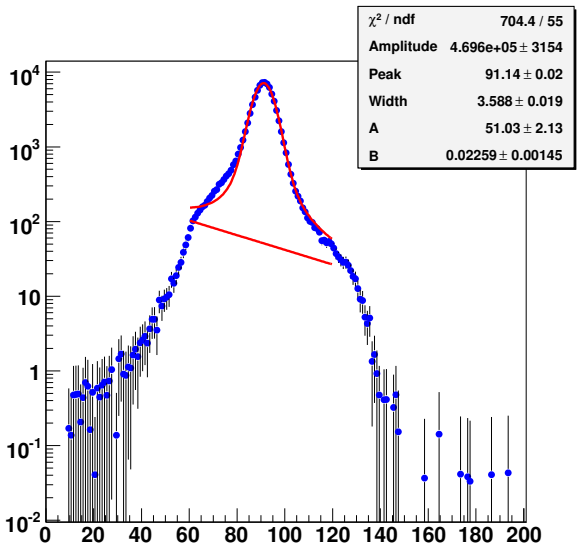

Figure 7.9: Dielectron mass fit in MC.

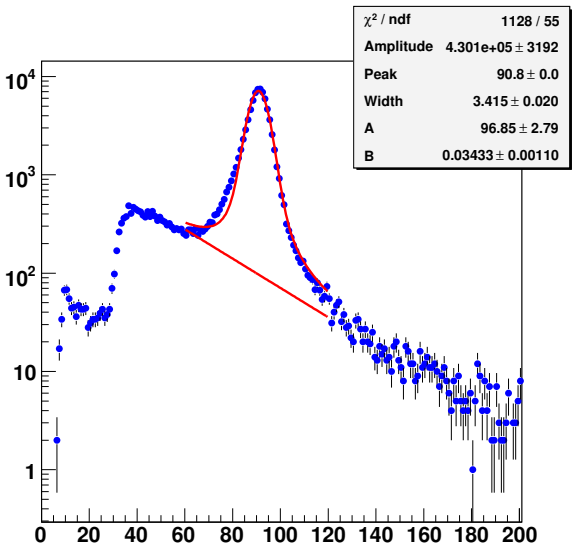

Figure 7.10: Dielectron mass fit in data.

dielectron mass in the data is fitted with a Breit-Wigner function convolved with Gaussian to determine the total number of Z events. The QCD+DY contribution is estimated by fitting the same mass peak with an exponential, and the ratio of DY+QCD/DY+QCD+Z is determined. The fit range is taken to be between 60 GeV and 120 GeV. The plots for the dielectron mass fit in MC and data are shown in Figs. 7.9 and 7.10, respectively. As we have

$$\mathrm{R(MC)} = \frac{\mathrm{N(DY)}}{\mathrm{N(Z+DY)}}, \tag{7.4}$$

$$\mathrm{N(exp)} = \mathrm{N(DY)} + \mathrm{N(QCD)\ in\ data}, \tag{7.5}$$

and we can also write

$$\frac{\mathrm{N(DY)}}{\mathrm{R(MC)}} = \mathrm{N(total)} - \mathrm{N(QCD)}.$$

From here the number of QCD events are calculated. The total QCD contribution comes out to be 3820 ± 114 (stat) $\pm$ 506 (sys) in a sample of 83722 events. The additional systematic uncertainty on the QCD background estimation is assigned to account for the relatively poor quality of the fit in the Z peak.

7.4 W Boson p_T Reweighting

The largest background in the $\tilde{t}_1$ search in jets plus $\not\!\!E_T$ channel is the production of the W bosons in association with jets where W bosons in allowed to decay leptonically via $W \rightarrow \ell\nu$. The presence of a neutrino in the final state makes the measurement of the W boson p_T spectrum difficult. It is important to get the kinematics of W boson right in order to be able to predict the W + jets background prediction correct. This was achieved by applying a reweighting function as was done for Z boson. In order to reweight W boson p_T, the reweighting function derived for Z boson shown in Fig. 7.5 was corrected by two factors:

- The ratio of $\frac{1}{\sigma}\frac{d\sigma(W)}{dp_T}$ to $\frac{1}{\sigma}\frac{d\sigma(Z)}{dp_T}$ at NLO [75]. This ratio along with the fit function is shown in Fig. 7.11.

- The ratio of $\frac{1}{\sigma}\frac{d\sigma(Z)}{dp_T}$ to $\frac{1}{\sigma}\frac{d\sigma(W)}{dp_T}$ predicted by ALPGEN at the generator level. This ratio along with the fit function is shown in Fig. 7.12.

The final expression used for reweighting the W boson p_T is taken to be the product of three functions shown in Figs. 7.5, 7.11 and 7.12 and is given by

$$\frac{Z/\gamma^{*\text{data}}(\rightarrow e^+e^-)+2j}{Z/\gamma^{*\text{ALPGEN}}(\rightarrow e^+e^-)+2j} \times \frac{\left[\frac{1}{\sigma}\frac{d\sigma(W)^{NLO}}{dp_T}\right]}{\left[\frac{1}{\sigma}\frac{d\sigma(Z)^{NLO}}{dp_T}\right]} \times \frac{\left[\frac{1}{\sigma}\frac{d\sigma(Z)^{\text{ALPGEN}}}{dp_T}\right]}{\left[\frac{1}{\sigma}\frac{d\sigma(W)^{\text{ALPGEN}}}{dp_T}\right]}. \tag{7.6}$$

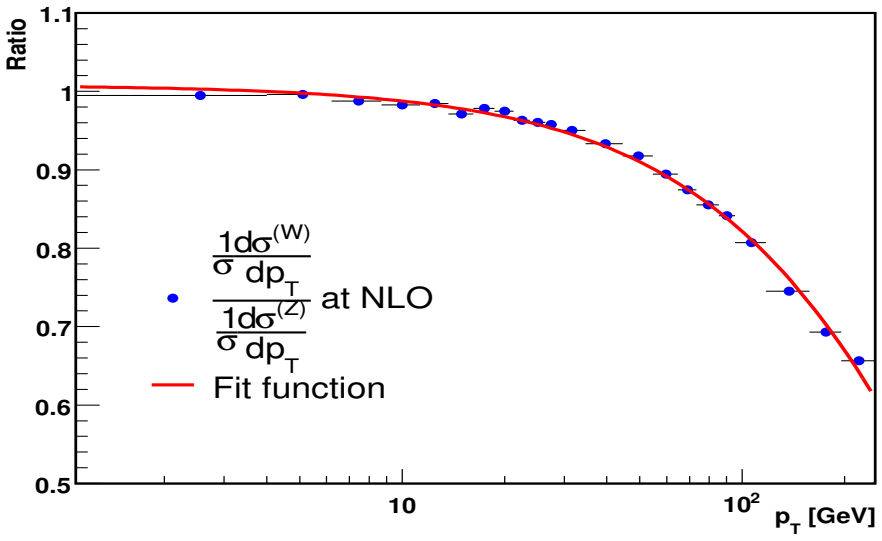

Figure 7.11: The ratio of the normalized cross sections for W and Z/γ^* production at NLO. The fit function given by $f(p_T) = Ae^{-Bp_T}$ is also shown.

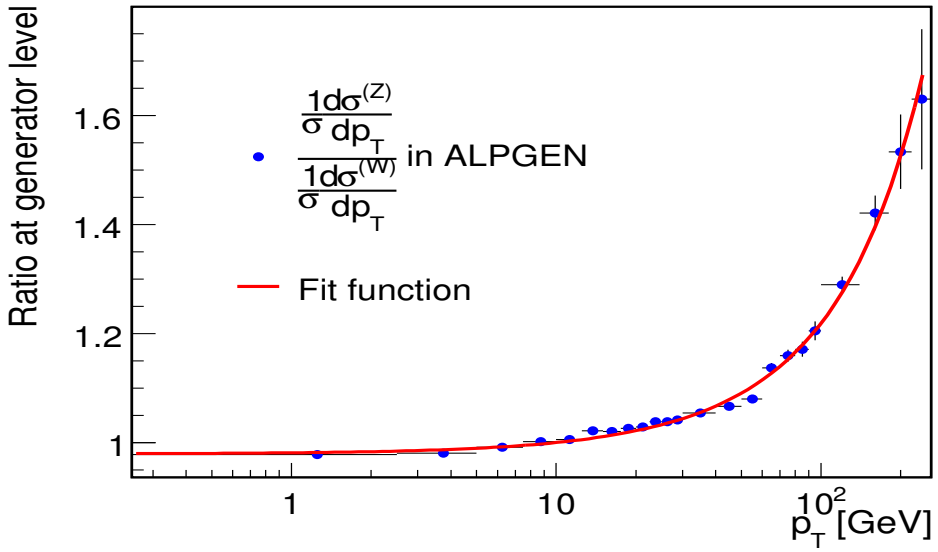

Figure 7.12: The ratio of the normalized cross sections for Z/γ^* and W production at generator level predicted by ALPGEN. The fit function given by $f(p_T) = A + Bp_T + Cp_T^2$ is also shown.

Chapter 8

$\tilde{t}_1 \rightarrow c\tilde{\chi}_1^0$ Analysis

This chapter describes the strategy and the selection criteria to search for $\tilde{t}_1$. The search involves three steps which include,

- selection of events on the basis of kinematical cuts.
- heavy flavor tagging.
- optimization of kinematical variables depending on the masses of $\tilde{t}_1$ and $\tilde{\chi}_1^0$.

Before describing the details of the selection criteria, the specifics of data set used and the background normalization procedures are described.

8.1 Data Sample

The $\tilde{t}_1$ search begins with a data set of 52 million events collected with the three-level trigger system at D0 and corresponds to 1.2 fb^{-1} of luminosity as described in Sec. 6.3. The selection criteria are applied at the preselection level in order to reduce the data set to a manageable size. Table 8.1 shows the cuts applied at the preselection level and the number of events after each selection. The data quality requirement includes removing the events with calorimeter noise and the events in which any other part of the detector including calorimeter, central tracker and muon system exhibited a bad response.

Cuts applied	Events
NP skim	58×10^6
Data quality and trigger (MHT30_3CJT5, JT1_ACO_MHT_HT)	20×10^6
At least one primary vertex, z (pv) < 60 cm, ≥ 2 jets with $p_T > 15$ GeV	17×10^6
$\not{E}_T > 40$ GeV	1.5×10^6

Table 8.1: At preselection level, selection cuts applied and the number of data events.

8.2 Background Normalization

8.2.1 V+Jets Background Normalization

The $Z/\gamma^*(\rightarrow e^+e^-)$+jets data is effectively introduced by replacing the luminosity with two-jet $Z/\gamma^*(\rightarrow e^+e^-)$ data, denoted by $N^{\rm data}_{Z/\gamma^*(ee)+2}$. This sample is chosen because in the end the $\tilde{t}_1$ search employs a cut on the numbers of jets exactly equal to two. We can write the luminosity in terms of number of events as

$$\mathcal{L} = \frac{N^{\rm data}_{Z/\gamma^*(ee)+2}}{K_Z \sigma^{ALP}_{Z(ee)+lp(2)} \hat{\epsilon}_{Z(ee)+lp(2)} + K'_Z \left(\sigma^{ALP}_{Z(ee)+c\bar{c}(2)} \hat{\epsilon}_{Z(ee)+c\bar{c}(2)} + \sigma^{ALP}_{Z(ee)+b\bar{b}(2)} \hat{\epsilon}_{Z(ee)+b\bar{b}(2)} \right)}.$$

Here $\hat{\epsilon}_{Z/\gamma^*(ee)+2}$, $\hat{\epsilon}_{Z/\gamma^*(ee)+c\bar{c}(2)}$, and $\hat{\epsilon}_{Z/\gamma^*(ee)+b\bar{b}(2)}$ are the acceptance$\times$ efficiency factors for detecting $Z/\gamma^*(\rightarrow e^+e^-)$+two jets. Note the "ˆ" to distinguish these factors from those used in the $\tilde{t}_1$ search. Eq. 7.1 then becomes

$$N^{\rm PRE}_{V(\ell\ell')+J} = N^{\rm data}_{Z(ee)+2} \times \frac{K_V \sigma^{ALP}_{V(\ell\ell')+J} \epsilon_{V(\ell\ell')+J}}{K_Z \sigma^{ALP}_{Z(ee)+lp(2)} \hat{\epsilon}_{Z(ee)+lp(2)} + K'_Z \left(\sigma^{ALP}_{Z(ee)+c\bar{c}(2)} \hat{\epsilon}_{Z(ee)+c\bar{c}(2)} + \sigma^{ALP}_{Z(ee)+b\bar{b}(2)} \hat{\epsilon}_{Z(ee)+b\bar{b}(2)} \right)}.$$

To force agreement in the data from a sample that consists of $N^{MC}_{V(\ell\ell')+J}$ simulated events, each MC event must be assigned a weight $w^{MC}_{V(\ell\ell')+J} = \frac{N^{\rm PRE}_{V(\ell\ell')+J}}{N^{MC}_{V(\ell\ell')+J}}$:

$$w^{MC}_{V(\ell\ell')+J} = \frac{N^{\rm data}_{Z(ee)+2}}{N^{MC}_{V(\ell\ell')+J}} \times \frac{K_V \sigma^{ALP}_{V(\ell\ell')+J} \epsilon_{V(\ell\ell')+J}}{K_Z \sigma^{ALP}_{Z(ee)+lp(2)} \hat{\epsilon}_{Z(ee)+lp(2)} + K'_Z \left(\sigma^{ALP}_{Z(ee)+c\bar{c}(2)} \hat{\epsilon}_{Z(ee)+c\bar{c}(2)} + \sigma^{ALP}_{Z(ee)+b\bar{b}(2)} \hat{\epsilon}_{Z(ee)+b\bar{b}(2)} \right)}. \quad (8.1)$$

To keep the expression simpler, Eq. 8.1 can be rewritten as

$$w^{MC}_{V(\ell\ell')+J} = f' \frac{N^{\rm data}_{Z(ee)+2}}{N^{MC}_{V(\ell\ell')+J}} \frac{K_V \sigma^{ALP}_{V(\ell\ell')+J}}{K_Z \sigma^{ALP}_{Z(ee)+lp(2)}} \frac{\epsilon_{V(\ell\ell')+J}}{\hat{\epsilon}_{Z(ee)+lp(2)}}, \tag{8.2}$$

with f' a correction for heavy flavor production in the normalization sample,

$$f' = \frac{K_Z \sigma^{ALP}_{Z(ee)+lp(2)} \hat{\epsilon}_{Z(ee)+lp(2)}}{K_Z \sigma^{ALP}_{Z(ee)+lp(2)} \hat{\epsilon}_{Z(ee)+lp(2)} + K'_Z \left(\sigma^{ALP}_{Z(ee)+c\bar{c}(2)} \hat{\epsilon}_{Z(ee)+c\bar{c}(2)} + \sigma^{ALP}_{Z(ee)+b\bar{b}(2)} \hat{\epsilon}_{Z(ee)+b\bar{b}(2)} \right)},$$

estimated to be $f' = 0.97 \pm 0.02$, with the uncertainty obtained by varying the heavy flavor K-factors by 50% from their nominal values.

Expressions for specific final states, as well as small corrections for electroweak effects and the luminosity difference between the NP skim and the $Z/\gamma^*(\rightarrow e^+e^-)$+jets normalization sample are described in the next section. We note here some general features of the $Z/\gamma^*(\rightarrow e^+e^-)$+jets normalization that can be inferred from Eq. 8.2

- ALPGEN cross sections and their K factors only appear as ratios. Cross section ratios are typically better known than absolute cross sections.

- The most reliably estimated background sources should be from Z decays with light parton jets, where the cross sections and K factors cancel. Next should be W decays with light partons, where one must trust that ALPGEN gets the ratio of W to Z cross sections right after application of the K factor, followed by W and Z plus heavy flavor jets.

- Normalizing to the $Z/\gamma^*(\rightarrow e^+e^-)+2$ jets sample, at least partially cancels the dependence of the background calculations on jet-related quantities like efficiency, energy scale, and resolution.

8.2.2 Normalization of $Z(\rightarrow \nu\bar{\nu})+$ Jets Events

The weight assigned to $Z(\rightarrow \nu\bar{\nu})$ + jets events is

$$w^{Z(\nu\bar{\nu})+n}_{MC} = f \times f' \times f'' \times \frac{N^{\rm data}_{Z(ee)+2}}{N^{MC}_{Z(\nu\bar{\nu})+n}} \times \frac{\sigma^{ALP}_{Z(\nu\bar{\nu})+n}}{\sigma^{ALP}_{Z(ee)+lp(2)}} \times \frac{\epsilon_{Z(\nu\bar{\nu})+n}}{\hat{\epsilon}_{Z(ee)+lp(2)}}.$$

where the factor f accommodates the absence of γ^* contribution to $Z(\rightarrow \nu\bar{\nu})+$ jets but the number of $Z/\gamma^*(ee)$ events determined from data include this contribution. For Z mass between 60 GeV and 130 GeV, the factor f is [76];

$$f \equiv \frac{\sigma(p\bar{p} \rightarrow Z) \times B(Z \rightarrow \ell\ell)}{\sigma(p\bar{p} \rightarrow Z/\gamma^*) \times B(Z/\gamma^* \rightarrow \ell\ell)} = 0.98178 \pm 0.00068.$$

The justification of having f' in the equation was described in Sec. 8.2.1. The factor f'' represents the differences in the luminosities of two data sets used. The $Z/\gamma^*(\rightarrow e^+e^-)$ events were determined from a data set that corresponds to a luminosity of 1067 pb^{-1} while the luminosity of the NP skim used in $\tilde{t}_1$ search is 995 pb^{-1}. Therefore

$$f'' \equiv \frac{995}{1067} = 0.93 \pm 0.01,$$

with most of the luminosity error canceling in the ratio. Following the same prescription we can write weight assigned to different $Z+$ jets samples.

$$w_{MC}^{Z(\nu\bar{\nu})+b\bar{b}+n} = f \times f'' \times \frac{N^{\rm data}_{Z(ee)+2}}{N^{MC}_{Z(\nu\bar{\nu})+b\bar{b}+n}} \times \frac{K'_Z \sigma^{ALP}_{Z(\nu\bar{\nu})+b\bar{b}+n}}{K_Z \sigma^{ALP}_{Z(ee)+lp(2)}} \times \frac{\epsilon_{Z(\nu\bar{\nu})+b\bar{b}+n}}{\hat{\epsilon}_{Z(ee)+lp(2)}}.$$

$$w_{MC}^{Z(\nu\bar{\nu})+c\bar{c}+n} = f \times f'' \times \frac{N^{\rm data}_{Z(ee)+2}}{N^{MC}_{Z(\nu\bar{\nu})+c\bar{c}+n}} \times \frac{K'_Z \sigma^{ALP}_{Z(\nu\bar{\nu})+c\bar{c}+n}}{K_Z \sigma^{ALP}_{Z(ee)+lp(2)}} \times \frac{\epsilon_{Z(\nu\bar{\nu})+c\bar{c}+n}}{\hat{\epsilon}_{Z(ee)+lp(2)}}.$$

$$w_{MC}^{Z(\mu\mu,\tau\tau)+n} = f' \times f'' \times \frac{N^{\rm data}_{Z(ee)+2}}{N^{MC}_{Z(\mu\mu,\tau\tau)+n}} \times \frac{\sigma^{ALP}_{Z(\mu\mu,\tau\tau)+n}}{\sigma^{ALP}_{Z(ee)+lp(2)}} \times \frac{\epsilon_{Z(\mu\mu,\tau\tau)+n}}{\hat{\epsilon}_{Z(ee)+lp(2)}}.$$

$$w_{MC}^{Z(\mu\mu,\tau\tau)+b\bar{b}+n} = f'' \times \frac{N^{\rm data}_{Z(ee)+2}}{N^{MC}_{Z(\mu\mu,\tau\tau)+b\bar{b}+n}} \times \frac{K'_Z \sigma^{ALP}_{Z(\mu\mu,\tau\tau)+b\bar{b}+n}}{K_Z \sigma^{ALP}_{Z(ee)+lp(2)}} \times \frac{\epsilon_{Z(\mu\mu,\tau\tau)+b\bar{b}+n}}{\hat{\epsilon}_{Z(ee)+lp(2)}}.$$

$$w_{MC}^{Z(\mu\mu,\tau\tau)+c\bar{c}+n} = f'' \times \frac{N^{\rm data}_{Z(ee)+2}}{N^{MC}_{Z(\mu\mu,\tau\tau)+c\bar{c}+n}} \times \frac{K'_Z \sigma^{ALP}_{Z(\mu\mu,\tau\tau)+c\bar{c}+n}}{K_Z \sigma^{ALP}_{Z(ee)+lp(2)}} \times \frac{\epsilon_{Z(\mu\mu,\tau\tau)+c\bar{c}+n}}{\hat{\epsilon}_{Z(ee)+lp(2)}}.$$

This is important to mention that last two equations do not have factors f and f' for the following reasons. There can be γ^* contributions to $\mu^+\mu^-$ and $\tau^+\tau^-$ final states. Furthermore the processes in last two equations have both light and heavy flavor jets in the final state therefore there is no need to correct by the factor f'.

8.2.3 Normalization of $W(\rightarrow \ell\nu)+$ Jets Events

Following the same procedure we can write the weight to be applied to $W(\rightarrow \ell\nu)+$ + jets sample as

$$w_{MC}^{W(\ell\nu)+n} = f \times f' \times f'' \times \frac{N^{\text{data}}_{Z(ee)+2}}{N^{MC}_{W(\ell\nu)+n}} \times \frac{K_W\ \sigma^{ALP}_{W(\ell\nu)+n}}{K_Z \sigma^{ALP}_{Z(ee)+lp(2)}} \times \frac{\epsilon_{W(\ell\nu)+n}}{\hat{\epsilon}_{Z(ee)+lp(2)}} \times \alpha.$$

$$w_{MC}^{W(\ell\nu)+b\bar{b}+n} = f \times f'' \times \frac{N^{\text{data}}_{Z(ee)+2}}{N^{MC}_{W(\ell\nu)+b\bar{b}+n}} \times \frac{K'_W\ \sigma^{ALP}_{W(\ell\nu)+b\bar{b}+n}}{K_Z \sigma^{ALP}_{Z(ee)+lp(2)}} \times \frac{\epsilon_{W(\ell\nu)+b\bar{b}+n}}{\hat{\epsilon}_{Z(ee)+lp(2)}} \times \alpha.$$

$$w_{MC}^{W(\ell\nu)+c\bar{c}+n} = f \times f'' \times \frac{N^{\text{data}}_{Z(ee)+2}}{N^{MC}_{W(\ell\nu)+c\bar{c}+n}} \times \frac{K'_W\ \sigma^{ALP}_{W(\ell\nu)+c\bar{c}+n}}{K_Z \sigma^{ALP}_{Z(ee)+lp(2)}} \times \frac{\epsilon_{W(\ell\nu)+c\bar{c}+n}}{\hat{\epsilon}_{Z(ee)+lp(2)}} \times \alpha.$$

In all of the above equations $K_Z = 1.23$, $K'_Z = 1.35$, $K_W = 1.4$, $K'_W = 1.4 \times 1.5$ and where

$$\alpha = \frac{\left[\frac{1}{\sigma}\frac{d\sigma(W)^{\text{NLO}}}{dp_T}\right]}{\left[\frac{1}{\sigma}\frac{d\sigma(Z)^{\text{NLO}}}{dp_T}\right]} \times \frac{\left[\frac{1}{\sigma}\frac{d\sigma(Z)^{\text{ALPGEN}}}{dp_T}\right]}{\left[\frac{1}{\sigma}\frac{d\sigma(W)^{\text{ALPGEN}}}{dp_T}\right]},$$

as described in Eq. 7.6 is the product of the ratio of the normalized cross sections for W and Z bosons production at NLO [75] and predicted by ALPGEN, respectively.

8.2.4 Normalization of $t\bar{t}$, Diboson and Single Top Backgrounds

Due to the small contributions of $t\bar{t}$, dibosons and single top background, the standard method which involves using the luminosity and cross sections was used to normalize these background. For these processes NLO cross sections were computed with MCFM 5.1 [67].

8.3 Kinematical Selection

The data set for the $\tilde{t}_1$ search is reduced to a sample of 2288 potential $\tilde{t}_1\bar{\tilde{t}}_1$ candidates, by applying the 15 selection criteria denoted by $\mathbf{C1} - \mathbf{C15}$ and summarized in Table 8.2. The main motivation for **C1** is to reduce the multijet background. Requirements **C2** to **C7** help in reducing the $W(\rightarrow \ell\nu)+$ jets and multijet backgrounds. The variable $|\eta_{\text{det}}|$ in **C5** and **C7** is the jet pseudorapidity

calculated using the assumption that the jet originates from the detector center. The condition on the charged particle fraction (CPF) in **C8** requires that at least 85% of the jets' charged particle transverse momenta be associated with tracks originating from the PV. This track confirmation requirement removes events with spurious $\not\!\!E_T$ due to the choice of an incorrect PV. $\mathbf{C9-C11}$ are applied to reject $W(\rightarrow \ell\nu)+$ jets background with isolated leptons from W boson decay where isolated electron, muon and track are defined in Chap. 5. The requirement on isolated tracks helps suppress backgrounds with τ leptons where the τ decays hadronically.

Remaining instrumental background is removed using a quantity defined by the angular separation between jets and the $\not\!\!E_T$ of the event, $D = \Delta\phi_{\rm max} - \Delta\phi_{\rm min}$, where $\Delta\phi_{\rm max}$ ($\Delta\phi_{\rm min}$) is the largest (smallest) azimuthal separation between a jet and $\not\!\!E_T$; and an asymmetry variable defined as $A = (\not\!\!E_T - \not\!\!H_T) \,/\, (\not\!\!E_T + \not\!\!H_T)$. The requirement on the variable D is applied because in the multijet (QCD) events jets tend to align along the $\not\!\!E_T$ direction while the variable A is sensitive to the amount of energy deposited in the calorimeter that was not clustered into jets. The distribution of A as shown in Fig. 8.1(a) peaks toward negative values for QCD events for the following reason: the $\not\!\!H_T$ of the event is calculated only from the jets with $p_T > 15$ GeV, while softer jets (arising from QCD effects) also contribute to the calculation of $\not\!\!E_T$. Figure 8.1 shows that both of these variables are very effective in eliminating multijet background. The requirements applied on these two variables are given by **C12** and **C13**. The cumulative signal efficiencies for different selection criteria for a sample with $m_{\tilde{t}_1} = 150$ GeV and $m_{\tilde{\chi}_1^0} = 70$ GeV are also shown in Table 8.2.

8.4 Background Estimation

8.4.1 SM Background

The background contributed by different SM processes are estimated using simulated MC samples after applying the selection cuts given in Table 8.2. The V+jets background contributions are normalized to data using the procedure described in Sec. 8.2.1 while diboson, $t\bar{t}$ and single top contributions were normalized to data using absolute luminosity and cross sections. Detailed

Selection	Events left	Signal eff. (%)
Initial cuts	1.5×10^6	55.9
C1: exactly two jets	464477	29.5
C2: $\not\!\!H_T > 40$ GeV	440161	27.5
C3: $\Delta\phi\ (\mathrm{jet}_1, \mathrm{jet}_2) < 165^\circ$	278505	26.5
C4: jet-1 $p_T > 40$ GeV	216382	24.7
C5: jet-1 $\lvert\eta_{\mathrm{det}}\rvert < 1.5$	113591	24.6
C6: jet-2 $p_T > 20$ GeV	80987	22.0
C7: jet-2 $\lvert\eta_{\mathrm{det}}\rvert < 1.5$	62910	20.1
C8: jet-1 jet-2 CPF > 0.85	49140	19.8
C9: no isolated track with $p_T > 5$ GeV	23832	13.4
C10: no isolated electron with $p_T > 10$ GeV	23194	13.3
C11: no isolated muon with $p_T > 10$ GeV	23081	13.3
C12: $\Delta\phi_{\mathrm{max}} - \Delta\phi_{\mathrm{min}} < 120^\circ$	9753	12.6
C13: $A > -0.05$	3733	12.0
C14: $\Delta\phi\ (\mathrm{jet}, \not\!\!E_T) > 50^\circ$	3375	11.6
C15: $\not\!\!E_T > 60$ GeV	2288	10.0

Table 8.2: Numbers of data events and the signal efficiencies for $m_{\tilde{t}_1} = 150$ and $m_{\tilde{\chi}_1^0} = 70$ GeV after each event selection.

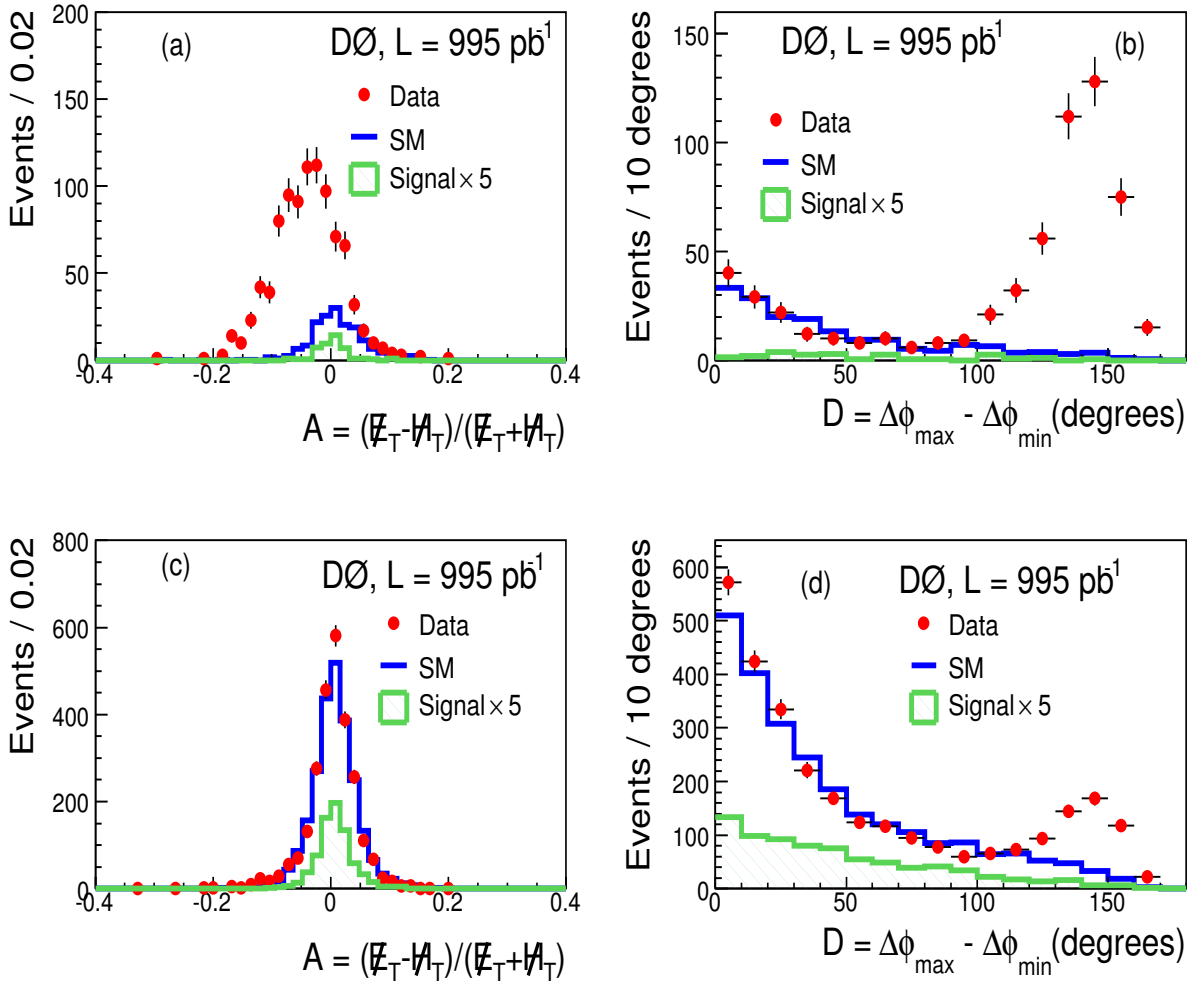

Figure 8.1: Distributions of the asymmetry $A = \not\!\!E_T - \not\!\!H_T / \not\!\!E_T + \not\!\!H_T$ with the cut on $\Delta\phi_{\max} - \Delta\phi_{\min}$ inverted (a) and applied (c). Distributions of $\Delta\phi_{\max} - \Delta\phi_{\min}$ with the cut on A inverted (b) and applied (d) for data (points with error bars), for SM backgrounds (histogram), and for a signal with $m_{\tilde{t}} = 150$ GeV and $m_{\tilde{\chi}_1^0} = 70$ GeV (hatched histogram). In all plots the signal contribution has been scaled by five and $\not\!\!E_T > 60$ GeV is required. The excess in data at $A = 0$ is consistent with the systematic uncertainties on the predicted background.

contributions from different SM sources are given in Table 8.3. One can see from Table 8.3 that the dominant background is V+jets. Diboson contribution is not negligible for the following reasons:

- In the WW sample, when one W decays into hadrons and other into leptons, with the lepton in the event escaping detection, this will look exactly like a signal event.
- In the WZ sample, an event with W decaying into hadrons and Z decaying into neutrinos will have the same topology as signal events.
- In the ZZ sample, when one Z decays into neutrinos and the other into hadrons, the event topology exactly mimics that of the signal. The case where hadronically decaying Z goes into a $c\bar{c}$ pair contributes an irreducible background to this search.

The requirement of exactly two jets suppresses $t\bar{t}$ contribution which always has more than two jets in final state. At this stage the background contributions from SM sources comes out to be $2274 \pm 14^{+316}_{-319}$ in a data sample of 2288 events.

A cross check was also performed by calculating the number of expected events using absolute luminosity and cross section normalization. The number of predicted events using absolute luminosity is $2371 \pm 15^{+547}_{-549}$. The two normalizations agree, keeping in view 6.1% uncertainty on the luminosity determination. The important point is that the systematic uncertainty due to the absolute normalization is a factor of two higher than that for V+jets normalization.

Two of the kinematical variables, which include the distributions of the transverse momentum of leading and second leading jets at this stage of the analysis are shown in Figs. 8.2 and 8.3. The distributions observed in data are well produced by MC prediction.

8.4.2 Multijet Background

The multijet background mostly arises from pure QCD processes. These processes are hard to simulate due to the calculational difficulties in non-perturbative QCD model. Therefore it is a

SM process	Number of events
$W\ (\rightarrow \ell\nu)$+jets	1017.2 ± 10.1
$Z\ (\rightarrow \nu\bar{\nu})$+ jets	807.4 ± 9.0
$W\ (\rightarrow \ell\nu) + c\bar{c}$	150.7 ± 2.9
$Z\ (\rightarrow \nu\bar{\nu}) + c\bar{c}$	96.8 ± 1.7
$W\ (\rightarrow \ell\nu) + b\bar{b}$	64.3 ± 1.0
$Z\ (\rightarrow \nu\bar{\nu}) + b\bar{b}$	54.7 ± 0.7
WW	25.6 ± 0.4
WZ	18.1 ± 0.5
ZZ	18.3 ± 0.3
Single top	9.1 ± 0.1
$Z\ (\rightarrow \tau\tau)$+jets	4.9 ± 0.3
$t\bar{t} \rightarrow \ell\nu\ \ell\nu\ b\bar{b}$	2.2 ± 0.02
$t\bar{t} \rightarrow l\nu\ b\bar{b}$ jj	2.1 ± 0.1
$Z\ (\rightarrow \mu\mu)$+jets	1.4 ± 0.1
$Z\ (\rightarrow \tau\tau) + c\bar{c}$	0.9 ± 0.1
$Z\ (\rightarrow \tau\tau) + b\bar{b}$	0.3 ± 0.02
$Z\ (\rightarrow \mu\mu) + c\bar{c}$	0.2 ± 0.01
$Z\ (\rightarrow \mu\mu) + b\bar{b}$	0.1 ± 0.01
Total	$2274.3 \pm 14.0\ ^{+316.9}_{-319.2}$
QCD	$9.1 \pm 8.5 \pm 3.4$
Data	2288

Table 8.3: Numbers of predicted background and observed data events before applying heavy flavor tagging with background normalized to number of Z events in data. First errors on total background and QCD events are statistical and second are systematic.

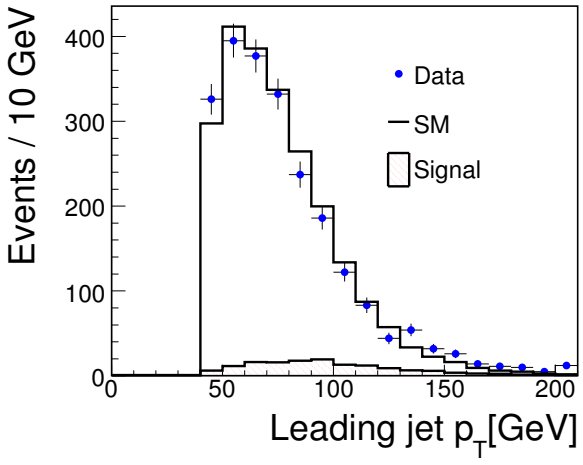

Figure 8.2: Distributions of the leading jet p_T after applying all analysis selection criteria for data (points with error bars), for SM backgrounds (histogram), and for a signal with $m_{\tilde{t}} = 150$ GeV and $m_{\tilde{\chi}_1^0} = 70$ GeV (hatched histogram).

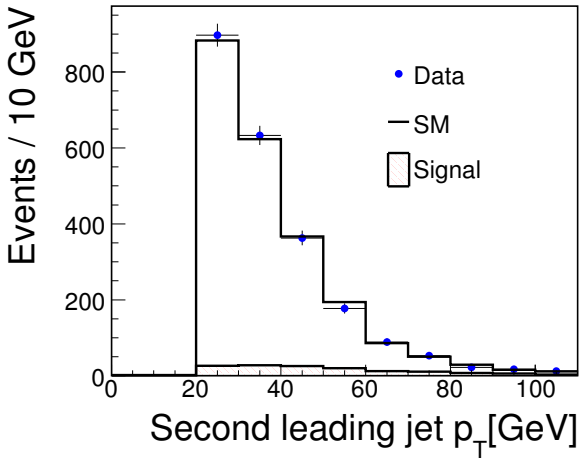

Figure 8.3: Distributions of the second leading jet p_T after applying all analysis selection criteria for data (points with error bars), for SM backgrounds (histogram), and for a signal with $m_{\tilde{t}} = 150$ GeV and $m_{\tilde{\chi}_1^0} = 70$ GeV (hatched histogram).

reasonable choice to estimate multijet background directly from the data.

The estimation of multijet background includes following steps:

- apply all analysis cuts given in Table 8.2 except that on $\not\!\!E_T$. The distribution of $\not\!\!E_T$ at this stage of the analysis is shown in Fig. 8.4. The excess at small values of $\not\!\!E_T$ is attributed to the QCD effects.

- subtract SM background contributions (estimated using the MC samples) from the data.

- fit the background subtracted $\not\!\!E_T$ distribution in the control region defined as $40 < \not\!\!E_T < 60$ GeV.

- extrapolate the contribution estimated from the control region to the signal region which is defined as $\not\!\!E_T > 60$ GeV region.

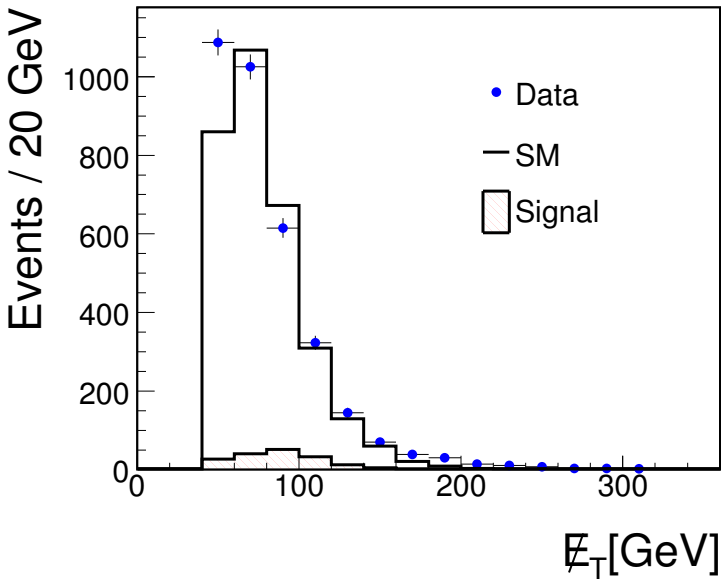

Figure 8.4: Distributions of the $\not\!\!E_T$ after applying all analysis cuts except one on $\not\!\!E_T$ for data (points with error bars), for SM backgrounds (histogram), and for a signal with $m_{\tilde{t}} = 150$ GeV and $m_{\tilde{\chi}_1^0} = 70$ GeV (hatched histogram).

To estimate the QCD background, the background subtracted $\not\!\!E_T$ distribution is fitted using two different fit functions that are given by

$$f(\not\!\!E_T) = N\frac{Ae^{-\left(\sqrt{A\not\!\!E_T} - \sqrt{A\not\!\!E_T{}^{\rm cut}}\right)}}{2\left(1+\sqrt{A\not\!\!E_T{}^{\rm cut}}\right)} \tag{8.3}$$

$$g(\not\!\!E_T) = N'\frac{(B+1)}{500^{B+1} - \not\!\!E_{T\,\rm cut}{}^{B+1}}\not\!\!E_T{}^{B} \tag{8.4}$$

where N and N' denote the number of QCD events beyond the value of $\not\!\!E_T{}^{\rm cut}$ which is taken to be 60 GeV. The values of N and N' as determined from the exponential and power law fits are 7.4 ± 6.9 and 10.8 ± 9.1, respectively. The fitted distributions of background subtracted $\not\!\!E_T$ distributions are shown in Figs. 8.5 and 8.6. The average of the two contributions is taken as an estimate of the QCD background before applying heavy flavor tagging and optimization of final selection criteria. The difference of the two contributions accounts for the systematic uncertainty on the QCD background determination. The final number of events contributed by the QCD background is $9.1 \pm 8.5 \pm 3.4$.

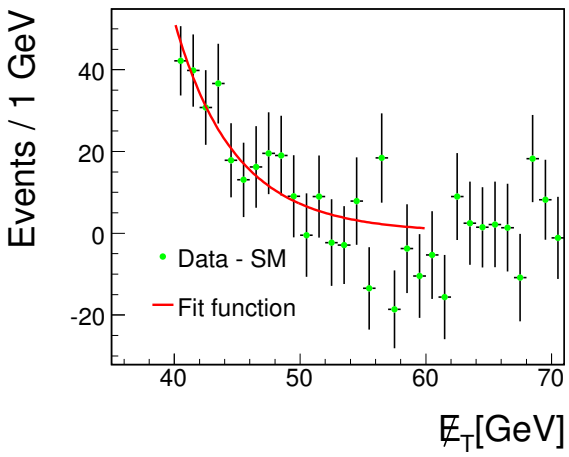

Figure 8.5: Exponential fit to $\not\!\!E_T$ distribution after subtracting SM background from the data.

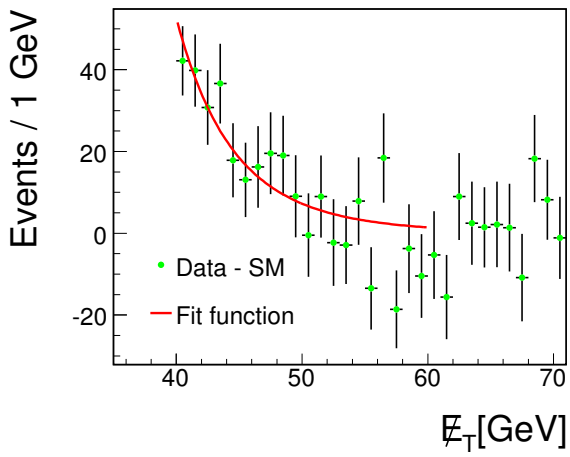

Figure 8.6: Power law fit to $\not\!\!E_T$ distribution after subtracting SM background from the data.

8.5 Heavy Flavor Tagging

The final state produced by $\tilde{t}_1$ decay has two jets that contain a charm quark inside them. In order to be able to distinguish between signal and background events an attempt is made to identify the flavor of the jets in the final state which is also referred to as heavy flavor (HF) tagging. The identification (or tagging) of a HF jet in the final state is done in two steps. In first steps, among all the jets a subset of jets known as "taggable jets" are selected. In the second step among the taggable jets different flavors of jets, light jets (jets with u, d, c, s quarks or gluon in them) and heavy flavors (jets with b or c quark inside them) are separated. The selection of taggable jets, and the details of the taggability study are discussed in next few sections.

8.5.1 Taggable Jets

A jet must be taggable to have a chance of being tagged. For a jet to be taggable it should have at least two tracks with at least one SMT hit. One track must have $p_T > 1$ GeV and all others with $p_T > 0.5$ GeV. The distance of the closest approach of tracks in xy-plane and along z-axis should be less than 0.2 cm and 0.4 cm, respectively, where all distances are measured with respect to the position of the PV.

8.5.2 Taggability

The taggability defined per jet is determined from data and is given by the relation

$$\text{Taggability } (p_T, \eta) = \frac{\#\text{ taggable jets in } (p_T, \eta) \text{ bin}}{\#\text{ jets in } (p_T, \eta) \text{ bin}}. \tag{8.5}$$

Due to the tracking inefficiencies in data, the taggability is not expected to be the same in data and MC. Therefore a parametrization of taggability is determined from data and applied to the MC in order to bring both at the same level. In order to study the taggability, the jets plus $\not\!\!E_T$ data set is used with the following requirement imposed:

- at least one PV.
- z(pv) < 60 cm.
- $\not\!\!E_T > 40$ GeV.
- $\not\!\!H_T > 40$ GeV.
- exactly two jets with $p_T > 15$ GeV.
- $\Delta\phi$ (jet1, jet2) $< 165°$.
- CPF > 0.85.
- veto on isolated tracks, electrons and muons.
- $\Delta\phi_{\text{max}} - \Delta\phi_{\text{min}} < 120°$.

After imposing these requirements, a two dimensional distribution of the taggability observed in data as a function of z of the primary vertex and the detector η of the jet is shown in Fig. 8.7. The symmetric structure in the central part of the detector and the asymmetry in the forward region corresponds to the geometry of the silicon tracker as shown in Fig. 4.4. A track is symmetrically reconstructed in η if the z of the primary vertex lies within ± 40 cm of the detector center. This region corresponds to the boundary where the barrel coverage ends. If the z position of the

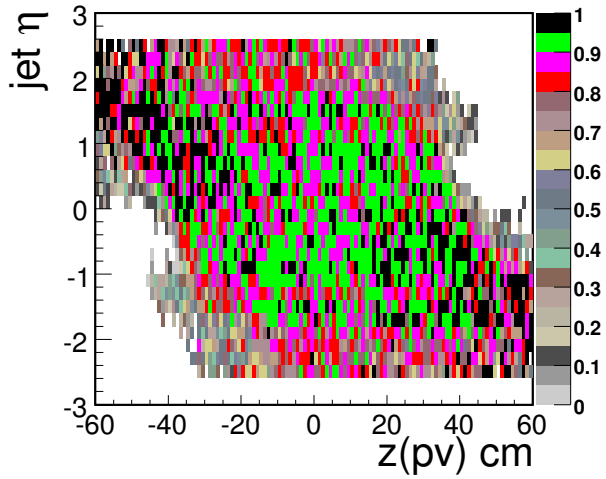

Figure 8.7: Two dimensional distribution of the taggability observed in data. The horizontal axis is the z position of the primary vertex while vertical axis in the detector η of the jet.

primary vertex lies outside this region the tracks having positive η will be reconstructed using hits found in the disks located at negative z position and vice versa. For this reason taggability is not only parametrized as functions of p_T and detector η of the jets but also a two dimensional parametrization, which takes into account the sign correlation between the detector η of the jet and the z position of the primary vertex, is used in order to correct for the taggability difference between data and MC.

The parametrization of taggability as functions of p_T and detector η of the jet are shown in Figs. 8.8 and 8.9. Figure 8.10 shows the distribution of the taggability observed in data as a function of the product of the detector η of the jet and sign of the z position of the primary vertex. The different distributions correspond to the six different regions along the z axis. It is obvious that most of the reconstructed tracks lie within the central part of the detector and for these tracks $z(\mathrm{pv}) \leq \pm 40$ cm. Figure 8.11 shows the two dimensional parametrization of taggability obtained by interpolating between the six fit functions as shown in Fig. 8.10. One can see that the taggability observed in data as shown in Fig. 8.7 is well reproduced by the parametrization. In the analysis at least one jet was required to be taggable and the parameterizations shown in Figs. 8.8, 8.9 and 8.11 were applied to the MC.

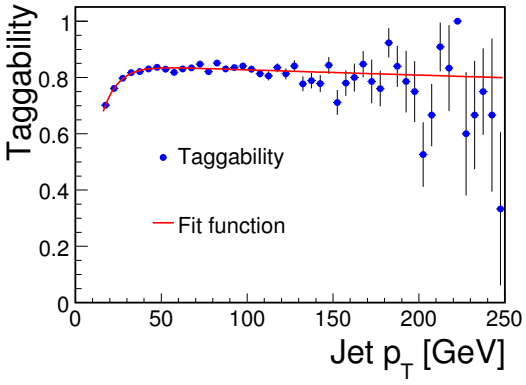

Figure 8.8: Taggability as a function of the p_T of the jet observed in data. The fit function used to parametrize the distribution is also shown.

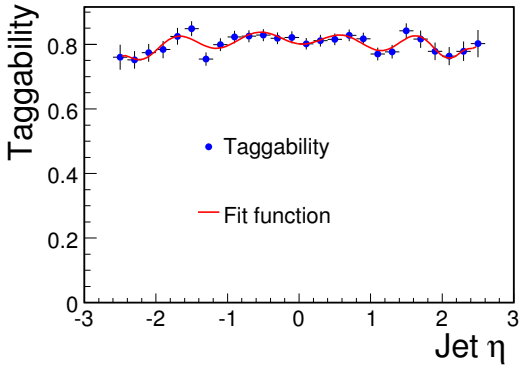

Figure 8.9: Taggability as a function of the detector η of the jet observed in data. The fit function used to parametrize the distribution is also shown.

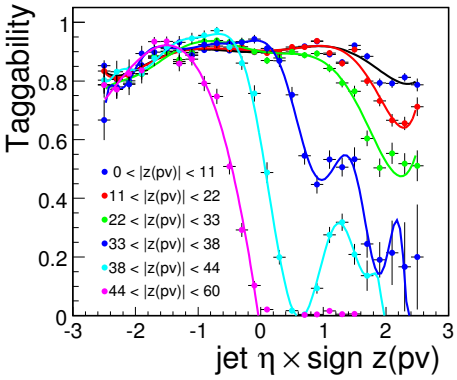

Figure 8.10: Taggability as a function of the product of the detector η of the jet and sign z(pv) divided into six regions according to the z position of the primary vertex. The fit function are also shown.

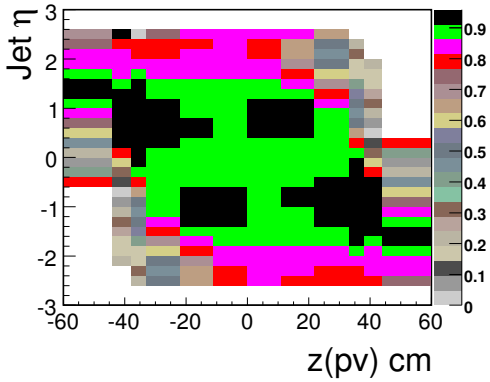

Figure 8.11: Taggability parametrization obtained by interpolating between six fit functions shown in Fig. 8.10.

8.5.3 Flavor Corrections for Taggability

The parametrization for taggability, to be applied to MC, is derived from data which mostly consists of light flavor jets. In order to be able to apply this parametrization to the MC samples that have b, c and τ jets, an additional correction factor needs to be folded in. For this purpose $Z(\rightarrow b\bar{b})$, $Z(\rightarrow c\bar{c})$, $Z(\rightarrow q\bar{q})$ and $Z(\rightarrow \tau^{+}\tau^{-})$ samples are used. The events are required to fulfill following selection criteria.

- at least one PV.
- $z(\text{pv}) < 60$ cm.
- at least two jets with $p_T > 15$ GeV.
- CPF > 0.85.

The requirements are kept loose in order to have sufficient statistics in MC. The taggability observed in these samples as functions of p_T and η_{det} of the jet are shown in top plots of Figs. 8.12 and 8.13. It can be seen from these plots that b, c and light jets have approximately the same taggability but the rate is different for τ jets. This happens due to the fact that 85% of the τ decays are one- prong via $\tau^{-} \rightarrow \pi^{-}\nu_{\tau}$ leaving one track in a jet. Therefore τ jets are less likely to pass the requirements of being taggable (at least two tracks). The taggailty flavor correction factor for each flavor of the jet was determined by taking the ratio of taggability in the particular sample to that in light jet sample. These ratios as function of p_T and η_{det} of the jet along with the parametrizations are shown in the bottom plots of Figs. 8.12 and 8.13.

8.5.4 Neural Network Tagging

The flavor of the jet in the final state is identified using a neural network (NN) tagging algorithm [77]. NN tagging algorithm combines the information from following three tagging algorithms and was optimized on MC.

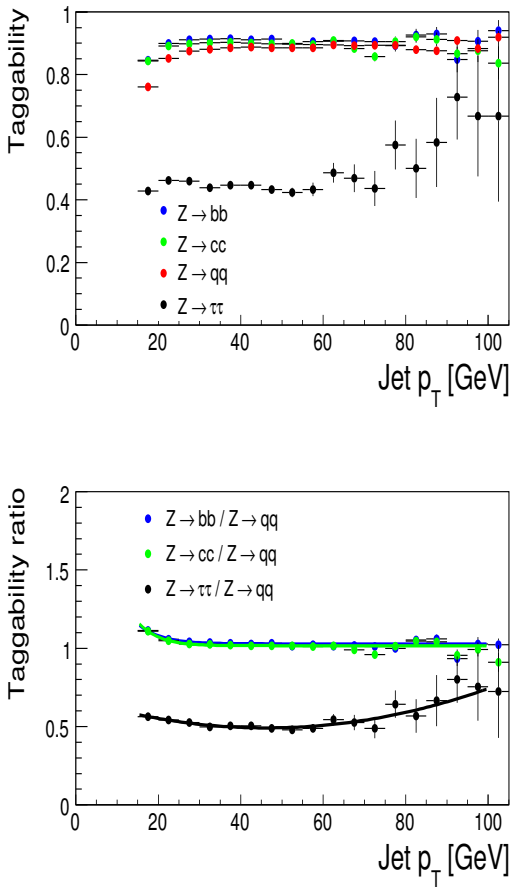

Figure 8.12: Top: Taggability as a function of the p_T of the jet for $Z(\rightarrow b\bar{b})$, $Z(\rightarrow c\bar{c})$, $Z(\rightarrow q\bar{q})$ and $Z(\rightarrow \tau^+\tau^-)$ MC samples. Bottom: The corresponding taggability ratios with respect to the light jet sample along with the fit functions.

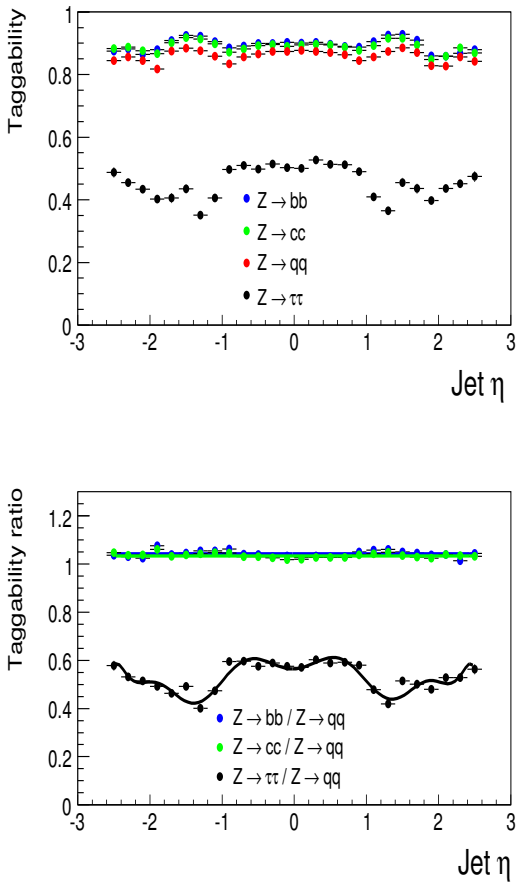

Figure 8.13: Top: Taggability as a function of the $\eta_{\rm det}$ of the jet for $Z(\rightarrow b\bar{b})$, $Z(\rightarrow c\bar{c})$, $Z(\rightarrow q\bar{q})$ and $Z(\rightarrow \tau^+\tau^-)$ MC samples. Bottom: The corresponding taggability ratios with respect to the light jet sample along with the fit functions.

- Jet lifetime probability (JLIP) [78]. This tagger converts information from the impact parameter of the tracks identified in a jet into a probability that all tracks originate from the PV, where the impact parameter is the distance of the closest approach to the interaction point in a plane perpendicular to the beam axis. This probability peaks towards zero for jets with b or c quark inside them while the distribution is expected to be flat for light jets.

- Secondary-vertex tagger (SVT) [79]. This tagger identifies the presence of vertices that are significantly displaced from the PV and associated with a jet. The presence of such vertices indicates the decays of the long-lived B and C hadrons whose lifetimes are $\tau = 1.671 \pm 0.018$ ps and 0.50 ± 0.01 ps, respectively.

- Counting signed impact parameter (CSIP) [80]. This tagger makes use of the number of tracks with large positive impact parameter significance, where the significance is defined as the ratio of the impact parameter to its uncertainty. The positive or negative sign of the impact parameter is assigned depending on whether a track crosses the jet axis in front of or behind the primary interaction point as shown in Fig. 8.14 [81]. In MC the distribution of impact parameter significance shows a bias towards positive values for heavy flavor jets while it is symmetric around zero for light jets .

The result of this combination is a NN output as shown in Fig. 8.15. In general the requirements in the NN tagging algorithm are optimized for b tagging ($\epsilon_b \approx 73\%$). In this analysis the requirement on the NN output is kept relatively loose is order to keep the efficiency for detection of charm jets high ($\epsilon_c \approx 30\%$). The NN output is required to be larger than 0.2. A trade-off is that the probability for a light parton jet to be mistakenly tagged in the central part of the calorimeter for the required NN output is $\approx 6\%$.

The jets are directly tagged in data which in turn means getting a number that can either be one or zero depending on whether or not a jet is tagged. On the other hand, in MC each jet is assigned a certain probability of being tagged depending on the p_T and η_{det} of the jet. The probabilities assigned to jets in MC are called "Tag Rate Functions" (TRF). TRFs properly take into account

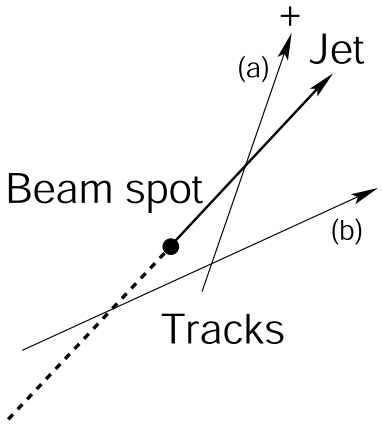

Figure 8.14: Definition of the signed impact parameter. The impact parameter is taken to be positive if the track crosses the jet axis ahead of the beam position (a). The impact parameter is negative if the track crosses the jet axis behind the beam position (b).

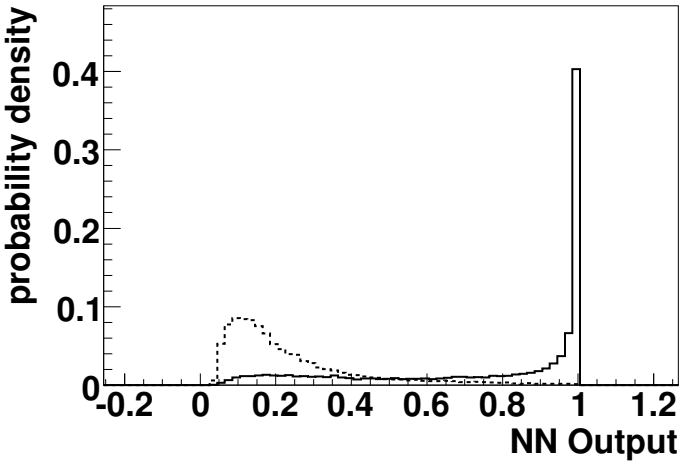

Figure 8.15: The NN output for the light jet QCD MC (dashed line) compared to the QCD $b\bar{b}$ MC (solid line). Both histograms are normalized to 1.

the difference in different reconstruction efficiencies between data and MC, in particular tracking efficiency which is overestimated in MC. The efficiencies of tagging b, c, τ and light jets in $Z(\rightarrow b\bar{b})$, $Z(\rightarrow c\bar{c})$, $Z(\rightarrow q\bar{q})$ and $Z(\rightarrow \tau^+\tau^-)$ samples as functions of p_T and $\eta_{\rm det}$ of the jet are shown in top plots in Figs. 8.16 and 8.17, where tagging efficiency is defined as

$$\text{Tagging efficiency } (p_T, \eta) = \frac{\#\text{ tagged jets in } (p_T, \eta) \text{ bin}}{\#\text{ taggable jets in } (p_T, \eta) \text{ bin}}. \tag{8.6}$$

The rate at which b jets are tagged is close to 80% while c and light jets are tagged at a rate of $\approx 30\%$ and 6%, respectvely. The official TRFs are available only for b, c and light jets. The TRFs for c jets are derived by scaling the measured b tagging efficiency in data by the b-to-c tagging efficiency ratio observed in MC.

As can be seen from Figs. 8.16 and 8.17 that the τ jets are tagged as often as c jets. Therefore same tagging probabilities as for c jets were used for τ jets. The additional correction taken to be the ratio of the tagging efficiency of τ jets to that for c jets was applied to τ jets to correct for any possible differences. The parameterizations of this ratio as functions of p_T and η_{det} of the jet are shown in bottom plot of Figs. 8.16 and 8.17.

In the analysis, at least one jet was required to be tagged where the probability of having at least one tag in an event that has more than one HF jets is calculated as

$$P^{\text{tag}}_{\text{event}}(N \geq 1) = 1 - \Pi_{i=1}^{N_{\text{jets}}} \left(1 - P_{\text{jet}(\alpha_i)}(p_{T_i}, \eta_i)\right), \tag{8.7}$$

where $P_{\text{jet}(\alpha_i)}(p_{T_i}, \eta_i)$ is the probability of i^{th} jet of flavor α to be tagged for a given p_{T_i} and η_i.

8.6 Optimization of Kinematical Variables

After applying the selection criteria shown in Table 8.2 and requiring the HF tagging, the final step of $\tilde{t}_1$ search analysis is the optimization of kinematical variables. A two jet system projected on the plane transverse to the beam direction can be described by three variables [82]. For optimization, these variables were chosen to be H_T , $\not\!\!E_T$, $S = \Delta\phi_{\text{max}} + \Delta\phi_{\text{min}}$. The distributions of these variables after applying kinematical cuts as described in Sec. 8.3 and requiring the HF tagging are shown in Figs. 8.18 - 8.20. During the process of optimization, the value of H_T is varied in steps of 20 GeV from 60 GeV - 140 GeV, the value of $\not\!\!E_T$ is varied in steps of 10 GeV from 60 GeV - 100 GeV, while the value of S is varied from $240^\circ - 320^\circ$ in steps of 20°. For H_T and $\not\!\!E_T$, the selection retained events above the cut value while for S, events below the cut value were selected.

For all $\tilde{t}_1$ and $\tilde{\chi}^0_1$ mass combinations shown in Table 6.7, all sets of cuts on the variables described

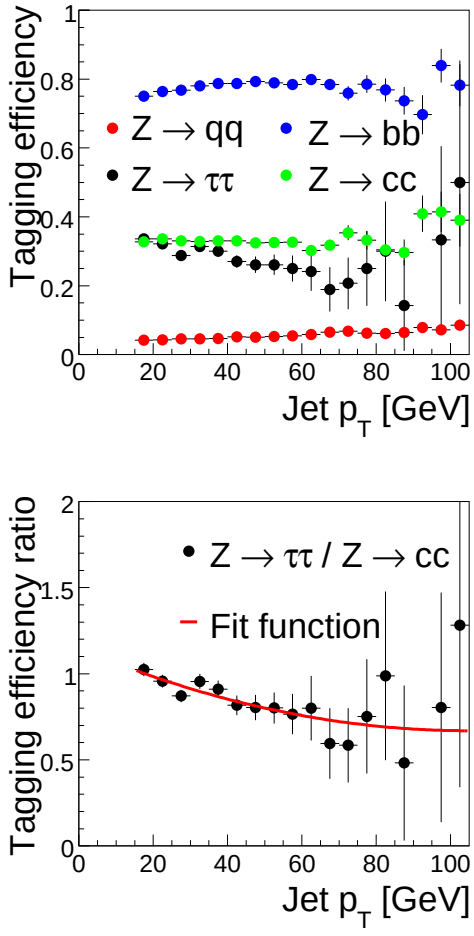

Figure 8.16: Top: Distributions for tagging efficiencies as a function of the p_T of the jet for $Z(\rightarrow b\bar{b})$, $Z(\rightarrow c\bar{c})$, $Z(\rightarrow q\bar{q})$ and $Z(\rightarrow \tau^+\tau^-)$ MC samples. Bottom: The distribution of the ratio of the tagging efficiency for τ jets to that for c jets along with the parametrization.

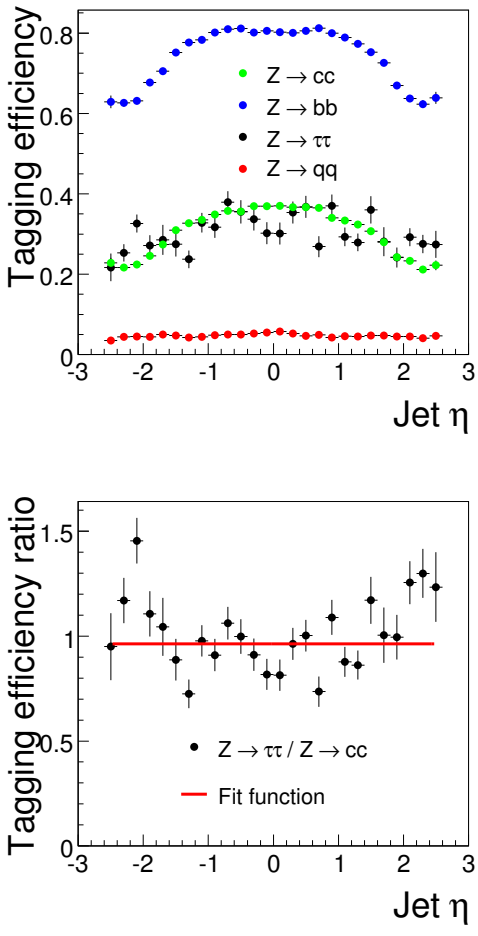

Figure 8.17: Top: Distributions for tagging efficiencies as a function of the η_{det} of the jet for $Z(\rightarrow b\bar{b})$, $Z(\rightarrow c\bar{c})$, $Z(\rightarrow q\bar{q})$ and $Z(\rightarrow \tau^+\tau^-)$ MC samples. Bottom: The distribution of the ratio of the tagging efficiency for τ jets to that for c jets along with the parametrization.

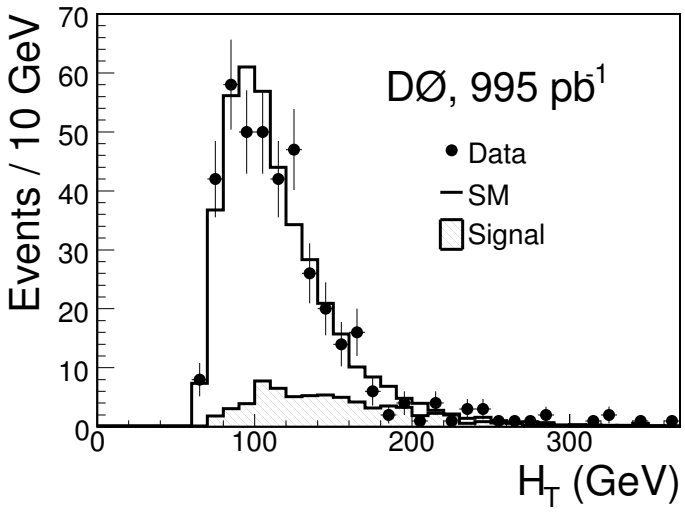

Figure 8.18: Distributions of the H_T after applying the kinematical cuts and requiring HF tagging for data (points with error bars), for SM backgrounds (histogram), and for a signal with $m_{\tilde{t}} = 150$ GeV and $m_{\tilde{\chi}_1^0} = 70$ GeV (hatched histogram).

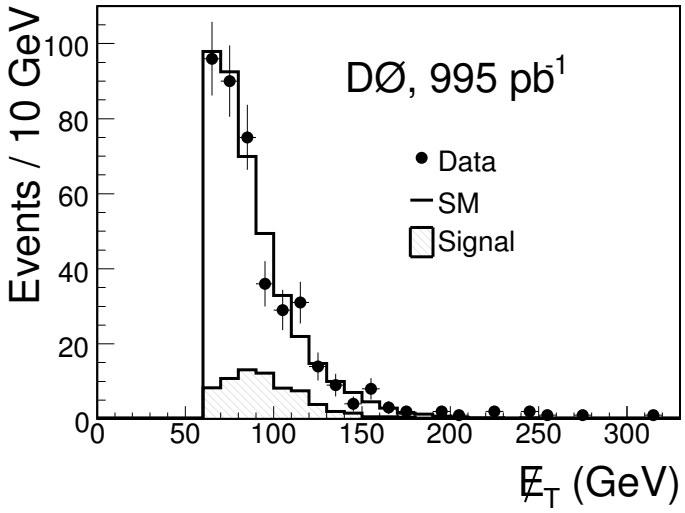

Figure 8.19: Distributions of the $\not\!\!E_T$ after applying the kinematical cuts and requiring HF tagging for data (points with error bars), for SM backgrounds (histogram), and for a signal with $m_{\tilde{t}} = 150$ GeV and $m_{\tilde{\chi}_1^0} = 70$ GeV (hatched histogram).

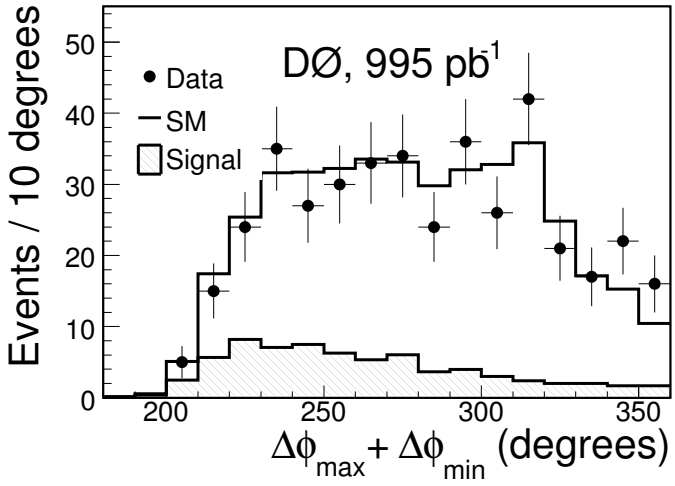

Figure 8.20: Distributions of S after applying the kinematical cuts and requiring HF tagging for data (points with error bars), for SM backgrounds (histogram), and for a signal with $m_{\tilde{t}} = 150$ GeV and $m_{\tilde{\chi}_1^0} = 70$ GeV (hatched histogram).

above are tested[1]. Using the number of events observed in data and expected from background and signal MC, the requirements on the variables are optimized by maximizing the lower limit on the $\tilde{\chi}_1^0$ mass for a given $\tilde{t}_1$ mass. The details of the limit calculation method are described in App. A. For each set of cuts the expected signal confidence level ($\langle CL_s \rangle$), using the hypothesis that only background were present, was computed with TLIMIT [83, 84] with the systematic uncertainties on the background and signal expectations (to be discussed later) taken into account. The correlation in the systematic uncertainties between signal and background were properly taken into account. For a given $\tilde{t}_1$ mass the expected lower limit on the $\tilde{\chi}_1^0$ mass was determined as the $\tilde{\chi}_1^0$ mass for which $\langle CL_s \rangle = 0.05$ by interpolating across all the $\tilde{\chi}_1^0$ masses tested. The set of selection criteria leading to the largest expected lower limit on the $\tilde{\chi}_1^0$ mass was selected as the optimum choice for the $\tilde{t}_1$ mass considered. In this procedure the lower value of the $\tilde{t}_1$ pair production cross section was used which is obtained by subtracting the uncertainties due to the scale and PDF choices from the nominal cross section. The expected and observed limits for $m_{\tilde{t}} = 150$ GeV as a function of $m_{\tilde{\chi}_1^0}$ is shown in Fig. 8.21.

[1]For a set of three variables where each variable can have five different values the set of cuts include 125 permutations.

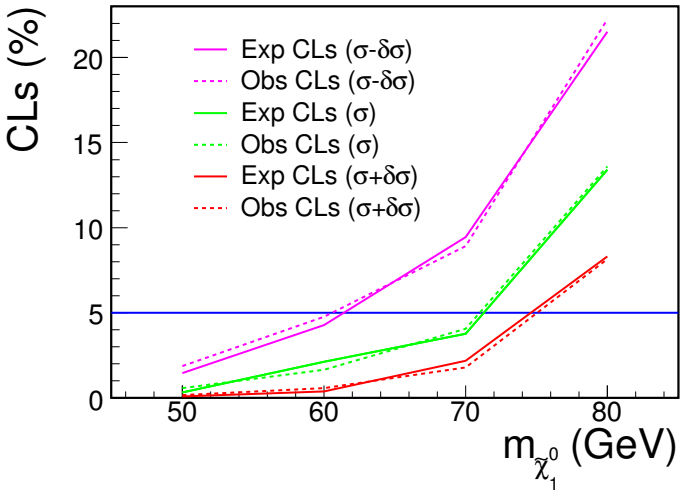

Figure 8.21: For $m_{\tilde{t}} = 150$ GeV, the evolutions of expected and observed CLs as a function of $m_{\tilde{\chi}_1^0}$ for lower, nominal and upper values of theoretical $\tilde{t}_1$ pair production cross section. The upper (lower) values of cross section are obtained by adding (subtracting) the theoretical uncertainty ($\approx 20\%$) to the nominal cross section.

The optimized values of the selection criteria for different $\tilde{t}_1$ masses along with the observed events in data and expected background events are shown in Table 8.4. The signal efficiencies for three signal mass points along with the number of expected signal events are shown in Table 8.5. The nominal theoretical $\tilde{t}_1$ pair production cross section at the 95% C.L. are also shown. The values for which σ_{UL} is larger than σ_{nom} are not excluded by this analysis. The background composition from different SM processes, along with the observed number of events in data, for three optimized selection criteria are shown in Table 8.6, 8.7 and 8.8. In all cases the data is well described by MC prediction and no significant excess is observed. Therefore the lower limits at the 95% C.L. are set on $\tilde{t}_1$ and $\tilde{\chi}_1^0$ masses. The control plots showing the different kinematical distributions after requiring the selection criteria optimized for $m_{\tilde{t}_1} = 150 - 160$ GeV are shown in Figs. B.1-B.4 in Appendix B. No contamination from multijet processes remains at this point therefore it was ignored in the limit setting procedure.

$m_{\tilde{t}_1}$	H_T	S	Observed	Predicted
$95 - 130$	> 100	< 260	83	$86.9 \pm 1.1^{+12.8}_{-13.0}$
$135 - 145$	> 140	< 300	57	$59.1 \pm 0.8^{+8.5}_{-8.8}$
$150 - 160$	> 140	< 320	66	$66.3 \pm 0.9^{+9.6}_{-10.0}$

Table 8.4: Optimized values of requirements, numbers of observed data and predicted background events. A requirement of $\not\!\!E_T > 70$ GeV was chosen in all cases. The values of $m_{\tilde{t}}$ and H_T are in GeV while those for S are in degrees.

$(m_{\tilde{t}_1}, m_{\tilde{\chi}^0_1})$	Efficiency	Expected Signal	$\sigma_{\rm nom}$	$\sigma_{\rm UL}$
GeV	%	Events	pb	pb
$(130, 55)$	1.5	$51.9 \pm 2.7^{+7.2}_{-7.1}$	3.44	2.41
$(140, 80)$	0.9	$19.6 \pm 0.8^{+2.8}_{-2.5}$	2.24	2.87
$(150, 70)$	2.1	$30.8 \pm 1.2^{+4.2}_{-3.7}$	1.49	1.42

Table 8.5: For three $\tilde{t}_1$ and $\tilde{\chi}^0_1$ mass combinations: signal efficiencies and the numbers of signal events expected. The first errors are statistical and second systematic. The nominal (NLO) signal cross section and upper limit at the 95% C.L. are also shown.

MC Samples	Number of events
$W(\rightarrow \ell\nu) + \text{jets}$	31.4 ± 0.8
$W(\rightarrow \ell\nu) + \text{HF}(b\bar{b}, c\bar{c})$	19.8 ± 0.6
$Z(\rightarrow \nu\bar{\nu}) + \text{jets}$	18.3 ± 0.5
$Z(\rightarrow \nu\bar{\nu}) + \text{HF}(b\bar{b}, c\bar{c})$	11.0 ± 0.1
Single top	2.3 ± 0.03
Dibosons	2.2 ± 0.2
$t\bar{t}$	1.6 ± 0.03
$Z(\rightarrow \ell\ell\ (\ell = e, \mu, \tau)) + \text{jets}$	0.2 ± 0.01
$Z(\rightarrow \ell\ell) + \text{HF}(b\bar{b}, c\bar{c})$	0.1 ± 0.01
Total BKG	86.9 ± 1.1
Data	83

Table 8.6: Numbers of expected background and observed data events after HF tagging optimization of selection criteria for $\tilde{t}_1$ masses between 95 GeV and 130 GeV. Errors are statistical only.

MC Samples	Number of events
$W(\rightarrow \ell\nu) + \text{jets}$	18.8 ± 0.7
$Z(\rightarrow \nu\bar{\nu}) + \text{jets}$	13.7 ± 0.4
$W(\rightarrow \ell\nu) + \text{HF}(b\bar{b}, c\bar{c})$	11.5 ± 0.2
$Z(\rightarrow \nu\bar{\nu}) + \text{HF}(b\bar{b}, c\bar{c})$	9.7 ± 0.1
Single top	1.9 ± 0.03
Dibosons	1.7 ± 0.1
$t\bar{t}$	1.6 ± 0.001
$Z(\rightarrow \ell\ell(\ell = e, \mu, \tau)) + \text{jets}$	0.1 ± 0.001
$Z(\rightarrow \ell\ell) + \text{HF}(b\bar{b}, c\bar{c})$	0.1 ± 0.001
Total BKG	59.1 ± 0.8
Data	57

Table 8.7: Numbers of expected background and observed data events after HF tagging and optimization of selection criteria for $\tilde{t}_1$ masses between 135 GeV and 145 GeV. Errors are statistical only.

MC Samples	Number of events
$W(\rightarrow \ell\nu) + \text{jets}$	20.0 ± 0.7
$Z(\rightarrow \nu\bar{\nu}) + \text{jets}$	15.8 ± 0.5
$W(\rightarrow \ell\nu) + \text{HF}(b\bar{b}, c\bar{c})$	12.3 ± 0.2
$Z(\rightarrow \nu\bar{\nu}) + \text{HF}(b\bar{b}, c\bar{c})$	11.6 ± 0.1
Dibosons	2.7 ± 0.2
Single top	2.0 ± 0.03
$t\bar{t}$	1.7 ± 0.001
$Z(\rightarrow \ell\ell(\ell = e, \mu, \tau)) + \text{jets}$	0.1 ± 0.001
$Z(\rightarrow \ell\ell) + \text{HF}(b\bar{b}, c\bar{c})$	0.1 ± 0.001
Total BKG	66.3 ± 0.9
Data	66

Table 8.8: Numbers of expected background and observed data events after HF tagging and optimization of selection criteria for $\tilde{t}_1$ masses between 150 GeV and 165 GeV. Errors are statistical only.

8.7 Systematic Uncertainties

Systematic uncertainties were evaluated separately for each optimization criteria, for background and all combinations of $\tilde{t}_1$ and $\tilde{\chi}_1^0$ masses. The sources of systematic uncertainties include

- Jet resolution.
- Jet energy scale.
- Jet reconstruction efficiency.
- Background normalization.
- Trigger efficiency.
- Data/MC scale factors
- Taggability.

- Tag rate function.
- PDF.
- Two jets cut.
- W boson p_T reweighting.

JES uncertainties are determined by varying the jet energies by $\pm 1\sigma$ of the error on the JES correction factor. This variation is propagated to all other variables used in the analysis that depend on the jet p_T e.g. $\not\!\!E_T$,$\not\!\!H_T$, H_T etc. The uncertainties on the jet resolution, identification and reconstruction efficiencies were evaluated by varying the efficiencies within their errors.

The normalization uncertainty on the background includes the 5% uncertainty coming from the $Z/\gamma^*(\rightarrow e^+e^-)+2$ jets statistics normalization on all samples normalized to Z events, an assumed 50% uncertainty on hevay flavor contribution, 8% uncertainty on the $t\bar{t}$ cross section, 6% uncertainty on diboson cross sections, 15% uncertainty on single top cross section and 6.1% uncertainty due to luminosity on the $t\bar{t}$, diboson and single top samples, which were estimated through absolute luminosity normalization.

The uncertainty on different scale factors applied to correct for differences between data and MC are determined by varying the appropriate parameters within their uncertainties. These scale factors include corrections for difference in; data quality requirement in data and MC[2], luminosity profile of real data and that of overlaid sample in MC, isolated electron, muon, track rejection efficiencies, the efficiency of requirement on the charged particle fraction of the jet. Uncertainties due to the taggability parametrization were evaluated by changing the fit parameter by their errors while the uncertainty due to tag rate function was evaluated by varying the tag rate function by $\pm 1\sigma$.

The uncertainty on the signal acceptance due to PDF choice was computed using 40 PDF sets for

[2]The simulated MC samples are overlaid with real data to incorporate the multiple interaction effects. Therefore the data quality in MC samples is required not to be compromised due to any bad quality overlaid data sample.

CTEQ6.1M, where upward and downward errors are given by

$$\delta\sigma^{\rm up}_{\rm PDF} = \frac{\sqrt{\sum_{xx=0}^{xx=40} |\sigma(\text{CTEQ6.1M.xx}) - \sigma(\text{CTEQ6.1M})|^2}}{\sigma(\text{CTEQ6.1M})}.$$

for $\sigma(\text{CTEQ6.1M.xx}) > \sigma(\text{CTEQ6.1M})$, and

$$\delta\sigma^{\rm down}_{\rm PDF} = -\frac{\sqrt{\sum_{xx=0}^{xx=40} |\sigma(\text{CTEQ6.1M.xx}) - \sigma(\text{CTEQ6.1M})|^2}}{\sigma(\text{CTEQ6.1M})}.$$

for $\sigma(\text{CTEQ6.1M.xx}) < \sigma(\text{CTEQ6.1M})$. The PDF uncertainty on the signal production cross section is explicitly taken into account in the limit setting process. Due to the background normalization procedure, the PDF uncertainties are expected to be canceled out to a large extent as all cross sections appear in the ratio. The remaining effect was evaluated using CTEQ6.1M PDF and a 4% systematic uncertainty was assigned on the background estimation due to the PDF choice.

Systematic uncertainties due to "exactly two jets" requirement are evaluated separately for signal and background. In order to find out the effect of this cut on background, ALPGEN $Z(\rightarrow e^+e^-)$ + jets events are compared with data. The p_T spectrum of first three jets after applying exactly the same cuts on jets as in $\tilde{t}_1$ analysis, and after applying Z p_T re-weighting, are shown in Fig. 8.22. From the bottom plot in Fig. 8.22 it can be inferred that the third jet p_T spectrum is well described by ALPGEN. The statistical uncertainty of the first bin, which shows the largest discrepancy, is taken as the uncertainty in the number of events removed by two jet requirement. For background, the error due to this requirement is $< 1\%$.

Since the third jet in the background sample is a "hard" jet generated in the primary interaction, this effect ($< 1\%$) cannot be applied to the signal sample. The signal is generated with PYTHIA and has two leading jets coming from the hard process from $\tilde{t}_1\bar{\tilde{t}}_1$ pair production. Any jet beyond the first two is added by PYTHIA though ISR/FSR. In order to estimate how well PYTHIA is able to model these ISR/FSR jets, the inclusive $Z/\gamma^*(\rightarrow e^+e^-)$ events simulated with PYTHIA are compared to data. The distribution of the leading jet, an ISR/FSR jet by construction, p_T is shown in Fig. 8.23. One can conclude from the plot that the effect of applying the two jets cut will result in minor overestimation of the efficiency for this cut as PYTHIA slightly underestimates the number

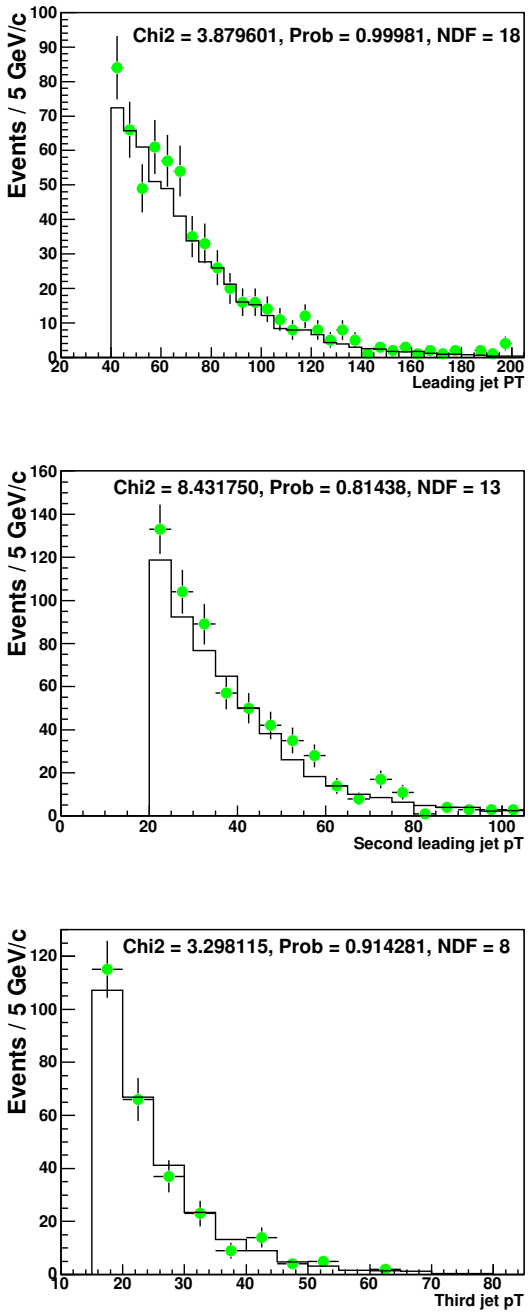

Figure 8.22: Distributions for leading, second leading and third leading jet p_T in $Z/\gamma^*(\rightarrow ee)+ \geq 2$ jets events generated with ALPGEN. Points are data and solid histogram is MC.

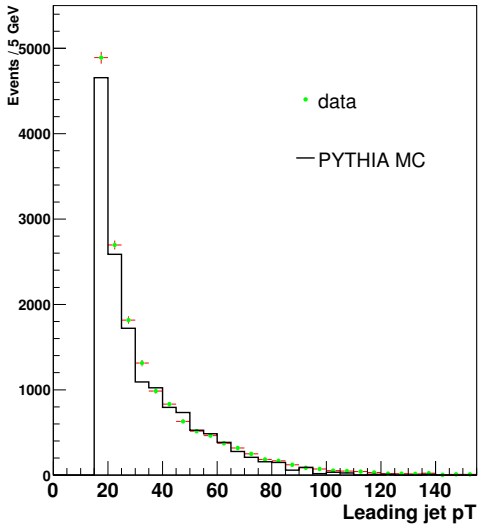

Figure 8.23: Distribution for leading jet p_T in $Z/\gamma^*(\rightarrow ee)+ \geq 1$ jet events generated with PYTHIA.

of leading jets at low p_T. The error on this correction determined form the statistics is $\pm 1.5\%$. The difference in the $W(\rightarrow \ell\nu)$+jets background estimation obtained using two values of $\alpha(p_T)$ was taken as the systematic uncertainty due to W boson p_T reweighting. In one case the value of $\alpha(p_T)$ was taken to be the product of fit functions shown in Figs. 7.11 and 7.12. While in second case $\alpha(p_T)$ was set equal to 1.[3] The systematic uncertainty turns out to be 3%. Details of the systematic uncertainties for background and one signal sample with $m_{\tilde{t}_1} = 150$ GeV and $m_{\tilde{\chi}^0} = 70$ GeV are given in Table 8.9.

[3] In other words it means applying the same reweighting to samples with W and Z bosons.

Source	SM background	Signal
Jet energy	$+1.7\%$	$+2\%$
scale	-2.5%	-4%
Jet resolution	$\pm 1\%$	$\pm 1\%$
Jet reconstruction	$\pm 0.8\%$	$\pm 0.1\%$
and identification		
Trigger	$\pm 6\%$	$\pm 6\%$
Scale factor	$\pm 5\%$	$\pm 5\%$
Normalization	$\pm 10\%$	–
Luminosity	–	$\pm 6.1\%$
HF tagging	$\pm 4.1\%$	$\pm 3.5\%$
PDF choice	$\pm 4\%$	$+8.7\%$
	–	-5.5%
Two jet cut	$\pm 0.9\%$	1.5%
W boson p_T	$\pm 3\%$	–
reweighting		

Table 8.9: Breakdown of systematic uncertainties on the SM background and for a signal point with $m_{\tilde{t}_1} = 150$ GeV and $m_{\tilde{\chi}_1^0} = 70$ GeV.

Chapter 9

Results and Conclusion

This thesis presents an analysis of a search for $\tilde{t}_1$ pair production in jets plus $\not\!\!E_T$ channel. The search uses 1 fb^{-1} of data collected during the Run IIa of the Tevatron. The $\tilde{t}_1$ is taken to be the next to the lightest supersymmetric particle and is assumed to decay into a charm quark and a neutralino at one-loop level with 100% branching fraction. After the final optimization the event yield in data is consistent with the expectations from known SM processes. As a result the lower limits are set on the $\tilde{t}$ and $\tilde{\chi}_1^0$ masses at the 95% C.L.

It is important to note that the current search significantly improves the exclusion contour in the $\tilde{t}_1$–$\tilde{\chi}_1^0$ mass plane over the previous search carried out by the D0 collaboration using 360 pb^{-1} of data [39]. This improvement arise due to the following reasons.

- Increase in luminosity by a factor of three, from 360 pb^{-1} to 995 pb^{-1}.
- Reduction in the MC statistical uncertainty from 17% to 2%.
- Reduction in the jet energy scale uncertainties on the final background estimation and expected signal events. This is due to the better understanding of the scale factors, their corelations, and errors on these factors. These factors are used to correct the jet energies measured by the calorimeter to the particle level. The jet energy scale errors are reduced from 13% to 3%.
- Reduction in the uncertainty on V+jets background normalization. The 5% statistical uncertainty of the $Z/\gamma^*(\rightarrow ee)+2$ jets sample was used to replace the 16% combined uncertainty

on the theoretical cross section and on the luminosity determination.

The largest $\tilde{t}_1$ mass excluded by this analysis is 155 GeV, for a neutralino mass of 70 GeV at the 95% C.L. With the theoretical uncertainty on the $\tilde{t}_1$ pair production cross section taken into account the largest limit on $\tilde{t}_1$ mass is 150 GeV for $m_{\tilde{\chi}_1^0} = 65$ GeV. The exclusion contour in $\tilde{t} - \tilde{\chi}_1^0$ mass plane is shown in Fig. 9.1. The observed (expected) limits is shown in solid (dashed) green line. The yellow band corresponds to the theoretical uncertainty on the $\tilde{t}_1$ pair prosuction cross section due to PDF and renormalization and factorization scale choice. Results from previous searches [35, 39, 85] are also shown.

9.1 Outlook

The 1 fb^{-1} of data set used in this analysis was collected with D0 detector from April 2003 to February 2006. Up to now D0 has recorded 3.1 fb^{-1} of data out of 3.75 fb^{-1} delivered by the Tevatron. With the expected 4 fb^{-1} of data collected by the end of this year, the lower limit on the mass of $\tilde{t}_1$ is expected to improve to 175 GeV, for a $\tilde{\chi}_1^0$ mass of 90 GeV [86]. Furthermore the Large Hadron Collider (LHC) is expected to begin data taking in pp collisions at $\sqrt{s} = 14$ TeV before the end of year 2008. At the high center of mass energies available at the LHC, the SUSY particles are expected to be produced copiously. In case of no discovery, the limits on their masses will be improved to a large extent.

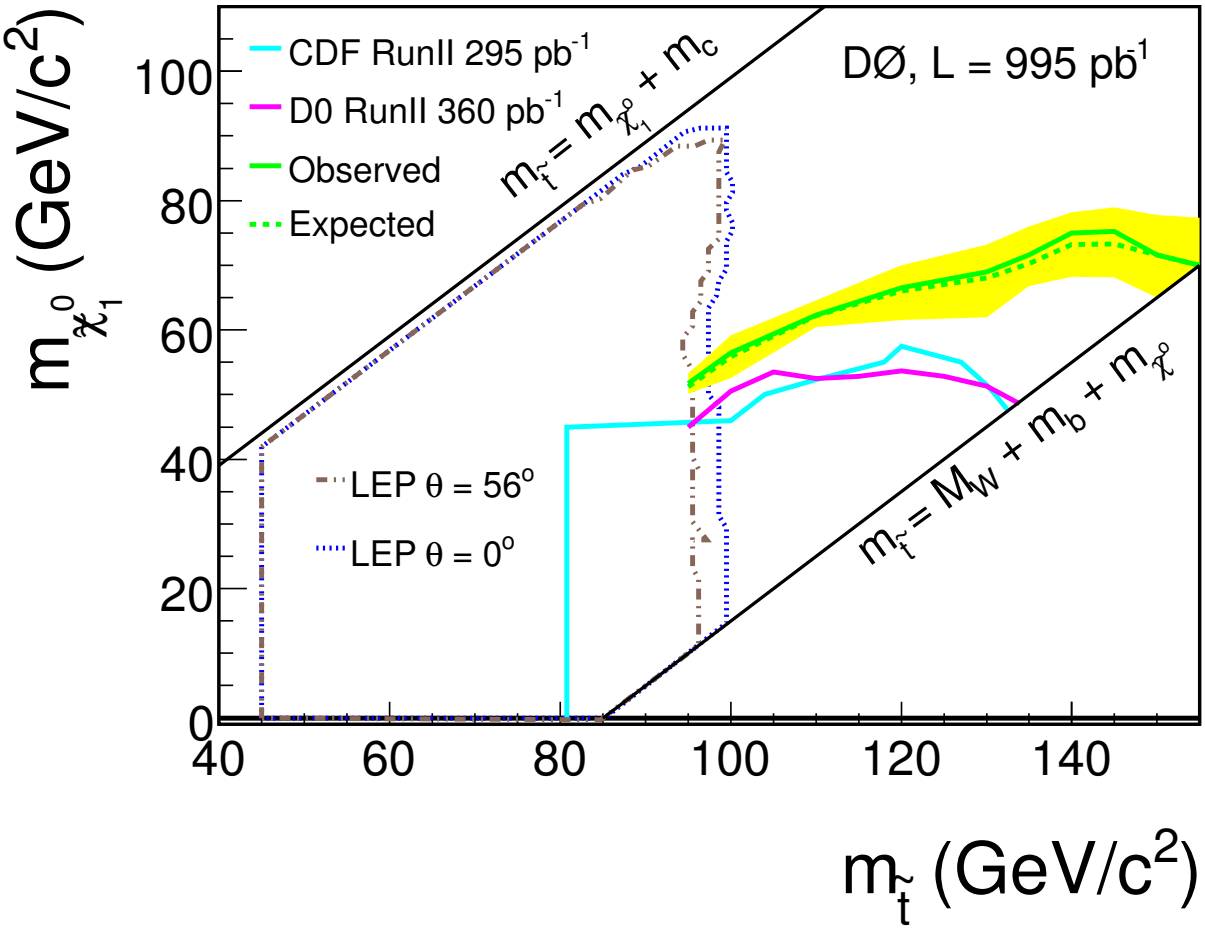

Figure 9.1: Region in the $\tilde{t}_1$–$\tilde{\chi}_1^0$ mass plane excluded at the 95% C.L. by the present search. The observed (expected) exclusion contour is shown as the green solid (dashed) line. The yellow band represents the theoretical uncertainty on the scalar top quark pair production cross section due to PDF and renormalization and factorization scale choice. Results from previous searches carried out by the D0, CDF and LEP collaboration are also shown.

Bibliography

[1] C. Quigg, *Gauge Theories of the Strong, Weak and Electromagnetic Interactions*, Addison-Wesley Publishing Company, 1983.

[2] W. B. Rolnick, *The Fundamental Particles and Their Interactions*, Addison-Wesely Publishing Company, 1994.

[3] F. Halzen and A. D. Martin, *Quarks and Leptons: An Introductory Course in Modern Particle Physics*, John Wiley and Sons, Inc., 1984.

[4] T. Araki et al., Phys. Rev. Lett. **94**, 081801 (2005).

[5] M. Drees, An introduction to supersymmetry, arXiv:hep-ph/9611409v1.

[6] H. E. Haber, Introductory low energy supersymmetry, arxiv:hep-ph/9306207.

[7] S. P. Martin, A supersymmetry primer, arXiv:hep-ph/9709356v4.

[8] J. Wess and J. Bagger, *Supersymmetry and Supergravity*, World Scientific Publishing Company, 1986.

[9] U. Amaldi, W. de Boer, and H. Fürstenau, Phys. Lett. B **260**, 447 (1991).

[10] D. Bailin and A. Love, *Supersymmetric gauge field theory and string theory*, Taylor and Francis Group, 1994.

[11] K. Cahill, Elements of supersymmetry, arxiv:hep-ph/9907295v1.

[12] A. Salam and J. Strathdee, Nucl. Phys. B **80**, 499 (1974).

[13] N. L. Bruner, *A Search for Production of Scalar Top At the Fermilab Tevatron Collider*, PhD thesis, The University of New Mexico, 1999.

[14] G. L. Kane, *Perspectives on Supersymmetry*, World Scientific Publishing Company, 1998.

[15] R. Demina, J. D. Lykken, K. T. Matchev, and A. Nomerotski, Stop and sbottom searches in RunII of the Fermilab Tevatron, arXiv:hep-ph/9910275v1.

[16] W. Beenakker, M. Krmer, T. Plehn, M. Spira, and P. M. Zerwas, Nucl. Phys. B **515**, 3 (1998).

[17] W. Beenakker, R. H*ö*pker, M. Spira, and P. Zerwas, Phys. Rev. Lett. **74**, 2905 (1995).

[18] H. Baer, M. Drees, R. Godbole, J. Gunion, and X. Tata, Phys. Rev. D **44**, 725 (1991).

[19] W. Beenakker, R. H*ö*pker, and M. Spira, Prospino: A program for the production of supersymmetric particles in next-to-leading order qcd, arXiv:hep-ph/9611232v1.

[20] J. Pumplin et al., JHEP **0207**, 012 (2002).

[21] D. Stump et al., JHEP **10**, 046 (2003).

[22] C. Boehm, A. Djouadi, and Y. Mambrini, Phys. Rev. D **61**, 095006 (2000).

[23] A. Djouadi and Y. Mambrini, Phys. Rev. D **63**, 115005 (2001).

[24] W. Porod, Phys. Rev. D **59**, 095009 (1999).

[25] K. Hikasa and M. Kobayashi, Phys. Rev. D **36**, 724 (1987).

[26] V. M. Abazov et al., Phys. Lett. B **660**, 449 (2008).

[27] H. Baer, J. Sender, and X. Tata, Phys. Rev. D **50**, 4517 (1994).

[28] A. Heister et al., Phys. Lett. B **537**, 5 (2002), (ALEPH Collaboration).

[29] J. Abdallah et al., Eur. Phys. J. **C31**, 421 (2003), (DELPHI Collaboration).

[30] P. Achard et al., Phys. Lett. B **580**, 37 (2004), (L3 Collaboration).

[31] G. Abbiendi et al., Phys. Lett. B **545**, 272 (2002), (OPAL Collaboration).

[32] T. Affolder et al., **84**, 5704 (2000), (CDF Collaboration).

[33] T. Affolder et al., Phys. Rev. Lett. **84**, 5273 (2000), (CDF Collaboration).

[34] D. Acosta et al., Phys. Rev. Lett. **90**, 251801 (2003), (CDF Collaboration).

[35] T. Aaltonen et al., Phys. Rev. D **76**, 072010 (2007), (CDF Collaboration).

[36] V. M. Abazov et al., Phys. Rev. Lett. **88**, 171802 (2002), (D0 Collaboration).

[37] V. M. Abazov et al., Phys. Rev. Lett. **93**, 011801 (2004), (D0 Collaboration).

[38] V. M. Abazov et al., Phys. Lett. B **659/3**, 500 (2007), (D0 Collaboration).

[39] V. M. Abazov et al., Phys. Lett. B **645**, 119 (2007), (D0 Collaboration).

[40] http://www.fnal.gov/pub/inquiring/physics/accelerators/chainaccel.html.

[41] http://www-bd.fnal.gov/public/multiturn.html.

[42] S. Jabeen, *Search for the single top quarks produced in s channel via electroweak interactions at $\sqrt{s} = 1.96$ TeV at the Tevatron*, PhD thesis, University of Kansas, 2006.

[43] B. Ward, A Tevatron kinematics primer, GLAS-PPE/01-04, April 2001.

[44] S. Abachi et al., Nucl. Instr. and Methods A **338**, 185 (1994), (D0 Collaboration).

[45] V. M. Abazov et al., Nucl. Instr. and Methods A **565**, 463 (2006), (D0 Collaboration).

[46] http://www-d0.fnal.gov/results/publications_talks/thesis/snyder/html/node28.html.

[47] D. Adams, Finding tracks, D0 Note 2958, CMS TN/96-062, 1996.

[48] K. Black, *A Precision Measurement of the Top Quark Mass*, PhD thesis, Boston University, 2005.

[49] R. Harrington, *Measurement of the Top Quark Mass in Lepton+Jets Events with Secondary Vertex Tagging*, PhD thesis, Northeastern University, 2007.

[50] A. Khanov, HTF: Histogramming method for finding tracks. The algorithm description, D0 Note 3778, 2000.

[51] H. Greenlee, The D0 Kalman track fit, D0 Note 4303, 2004.

[52] A. Schwartzman and C. Tully, Primary vertex reconstruction by means of adaptive vertex fitting, D0 Note 4918, 2005.

[53] W. C. Fisher, *A Search for anomalous heavy-flavor quark production in association with W boson*, PhD thesis, Princeton University, 2005.

[54] G. C. Blazey et al., in Proceedings of the Workshop: QCD and Weak Boson Physics in Run II, edited by U. Baur, R. K. Ellis, and D. Zeppenfeld, Fermilab-Pub-00/297, 2000.

[55] A. Harel, Jet ID Optimization, D0 Note 4919, 2005.

[56] A. Juste et al., Jet Energy Scale Determination at D0 RunII, D0 Note 5382, 2007.

[57] N. Makovec and J.-F. Grivaz, Shifting, Smearing and Removing Simulated Jets, D0 Note 4914, 2005.

[58] M. L. Mangano et al., JHEP **0307**, 001 (2003).

[59] T. Sjöstrand et al., Comput. Phys. Commun. **135**, 238 (2001).

[60] J. Pumplin et al., JHEP **0207**, 012 (2002).

[61] J. Pumplin et al., JHEP **0310**, 046 (2003).

[62] http://www-d0.fnal.gov/computing/MonteCarlo/MonteCarlo.html.

[63] http://www-d0.fnal.gov/computing/MonteCarlo/simulation/d0gstar.html.

[64] http://www-d0.fnal.gov/computing/MonteCarlo/simulation/d0sim.html.

[65] R. Brun and F. Carminati, CERN Program Library Long Writeup W5013, 1993.

[66] http://www-d0.fnal.gov/computing/algorithms/#intro.

[67] MCFM, http://mcfm.fnal.gov/.

[68] E. Boos et al., Nucl. Instrum. Methods Phys. Res.,Sect. A **534**, 250 (2004).

[69] A. Zabi, L. Duflot, J.-F. Grivaz, P. Verdier, and A. Duperrin, A trigger for jets and missing E_T, D0 Note 4315, 2003.

[70] M. Petteni, T. Christoudias, and G. Davies, Search for $ZH \to \nu\bar{\nu}b\bar{b}$, D0 Note 5353, 2007.

[71] https://plone4.fnal.gov/P1/D0Wiki/tdaq/tsg/caftrigger/dietriggers.

[72] J. Collins, D. Soper, and G. Sterman, Nucl. Phys. B **250**, 199 (1985).

[73] C. Balazs and C. P. Yuan, Phys. Rev. D **56**, 5558 (1997).

[74] V. M. Abazov et al., Phys. Rev. Lett. **100**, 102002 (2008).

[75] K. Melnikov and F. Petriello, Phys. Rev. D **74**, 114017 (2006).

[76] J. D. Hobbs, T. Nunnemann, and R. V. Kooten, Study of the $p\bar{p} \to Z/\gamma* \to ee$ and $p\bar{p} \to Z/\gamma* \to \mu\mu$, event yields as a luminosity cross check, D0 Note 5268, 2006.

[77] M. Anastasoaie, S. Robinson, and T. Scanlon, Performance of the NN b-tagging tool on p17 data, D0 Note 5213, 2007.

[78] D. Bloch and B. Clement, Update of the JLIP b-tagger Performance in p14/pass2 data with JES 5.3, D0 Note 4824, 2005.

[79] D. Boline, L. Feligioni, and M. Narain, Update on b-quark Jet Identification with Secondary Vertex Rconstruction using D0Reco Version p14-Pass2 Samples, D0 Note 4976, 2005.

[80] R. Demina, A. Khanov, and F. Rizatdinova, b-tagging with Counting Signed Impact Parameter method, D0 Note 4049, 2002.

[81] C. M. Anăstăsoaie, *A search for $W^{\pm}H \rightarrow \mu\nu b\bar{b}$ production at the Tevatron*, PhD thesis, Radboud Universiteit Nijmegen, 2008.

[82] J. Linnemann, Some comments on angles in LQ and stop analysis, D0 Note 5180, 2006.

[83] T. Junk, Nucl. Instrum. Methods Phys. Res. A **434**, 435 (1999).

[84] A. Read, 1st workshop on confidence limits, CERN Report No. CERN-2000-005, 2000.

[85] LEPSUSYWG Collaboration, ALEPH Collaboration, DELPHI Collaboration, L3 Collaboration, opal collaboration, note lepsusywg/04-02.1, http://lepsusy.web.cern.ch/lepsusy/www/squarks_summer04/stop_combi_208_final.html.

[86] http://www-cdf.fnal.gov/physics/exotic/r2a/20060622.stopsbottom/plots.

Appendix A

Limit Calculation

The selection criteria in $\tilde{t}_1$ search are optimized by minimizing the upper limit on the $\tilde{t}$ pair production cross section. This procedure makes use of the Root based algorithm TLIMIT and the method is called CLs, which stands for confidence level of signal, and is evaluated in the background only hypothesis. The method takes the number of signal, background and data events as input and runs a set of MC experiments to compute the 95% C.L. limits using the likelihood ratio method in modified Frequestist approach. The signal and background inputs are fluctuated according to their systematic uncertainties.

For the given number of observed data and expected background and signal events the likelihood ratio is computed assuming that the probability distributions for signal and background follow Poisson statistics, i.e.

$$M = \frac{e^{-(s+b)}(s+b)^d}{d!} / \frac{e^{-b}b^d}{d!}, \tag{A.1}$$

where s, b and d denote signal, background and data events respectively. By varying the number of expected background and signal events within their statistical and systematic errors, a larger number of MC pseudo-experiments are generated and the quantity

$$M' = \frac{e^{-(s+b)}(s+b)^{d'}}{d'!} / \frac{e^{-b}b^{d'}}{d'!}, \tag{A.2}$$

is evaluated. Here d' is the number of observed events in a particular pseudo-experiment. The quantity CL_{s+b} is defined as the combined likelihood variable for all pseudo-experiments in which

$M' < M$, i.e.

$$CL_{s+b} = \sum_{M'<M} \frac{e^{-(s+b)}(s+b)^{d'}}{d'!}. \tag{A.3}$$

Similarly

$$CL_b = \sum_{M'<M} \frac{e^{-b}b^{d'}}{d'!}. \tag{A.4}$$

The signal confidence level is then defined as the

$$CL_s = \frac{CL_{s+b}}{CL_b}. \tag{A.5}$$

The effects of systematic uncertainties, which are assumed to have a Gaussian distribution, are taken into account when computing the combined likelihood. A particular signal mass point is excluded at the 95% C.L. if $CL_s \leq 5\%$.

Appendix B

Control Plots

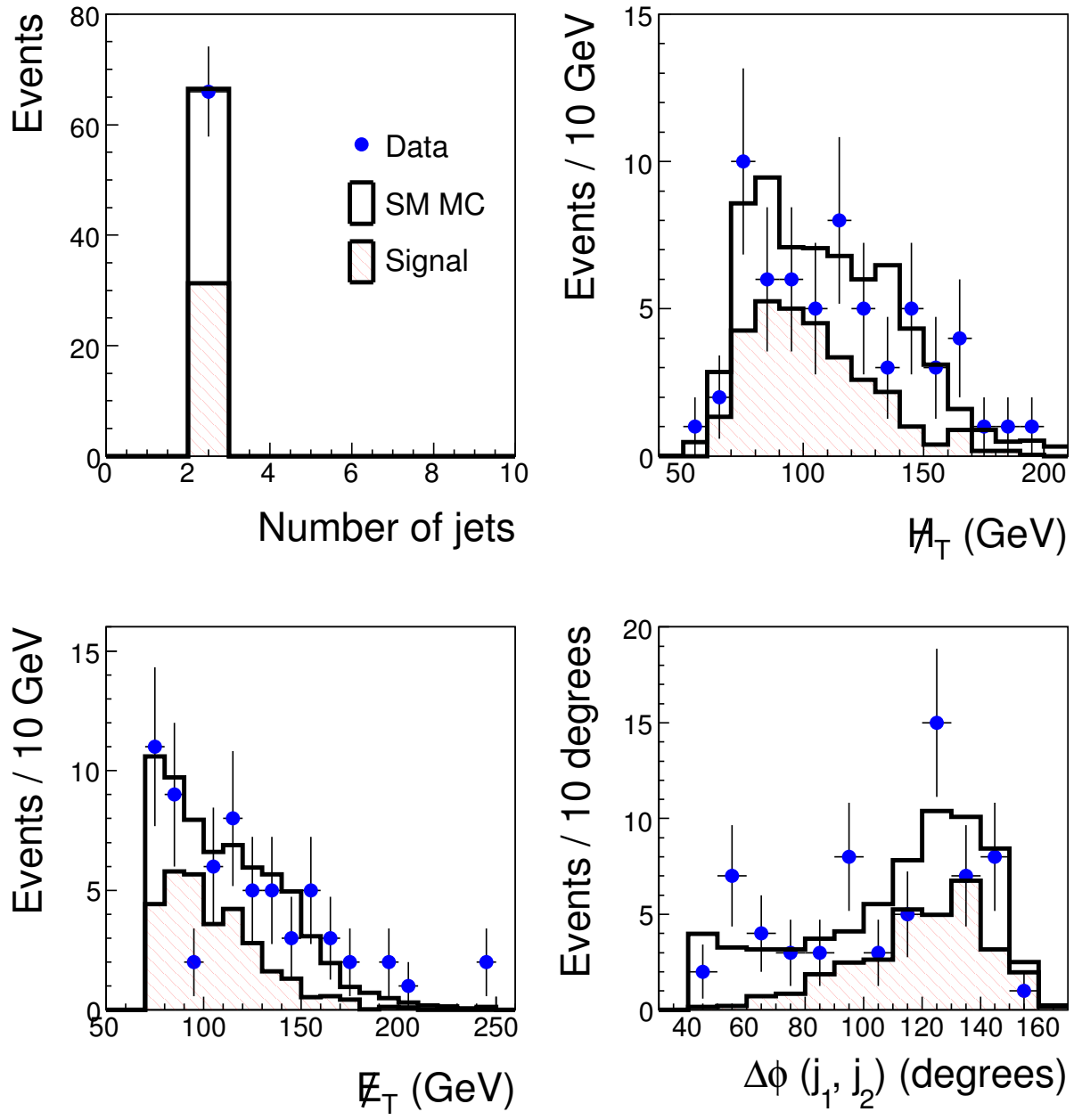

Figure B.1: Distributions for number of jets, $\not\!\!H_T$, $\not\!\!E_T$ and $\Delta\phi(\mathrm{j}_1, \mathrm{j}_2)$ after requiring the selection criteria optimized for $\tilde{t}_1$ masses between 150 GeV to 160 GeV for data (points with error bars), SM background (solid histogram), and a signal with $m_{\tilde{t}_1} = 150$ GeV and $m_{\tilde{\chi}_1^0} = 70$ GeV (hatched histogram).

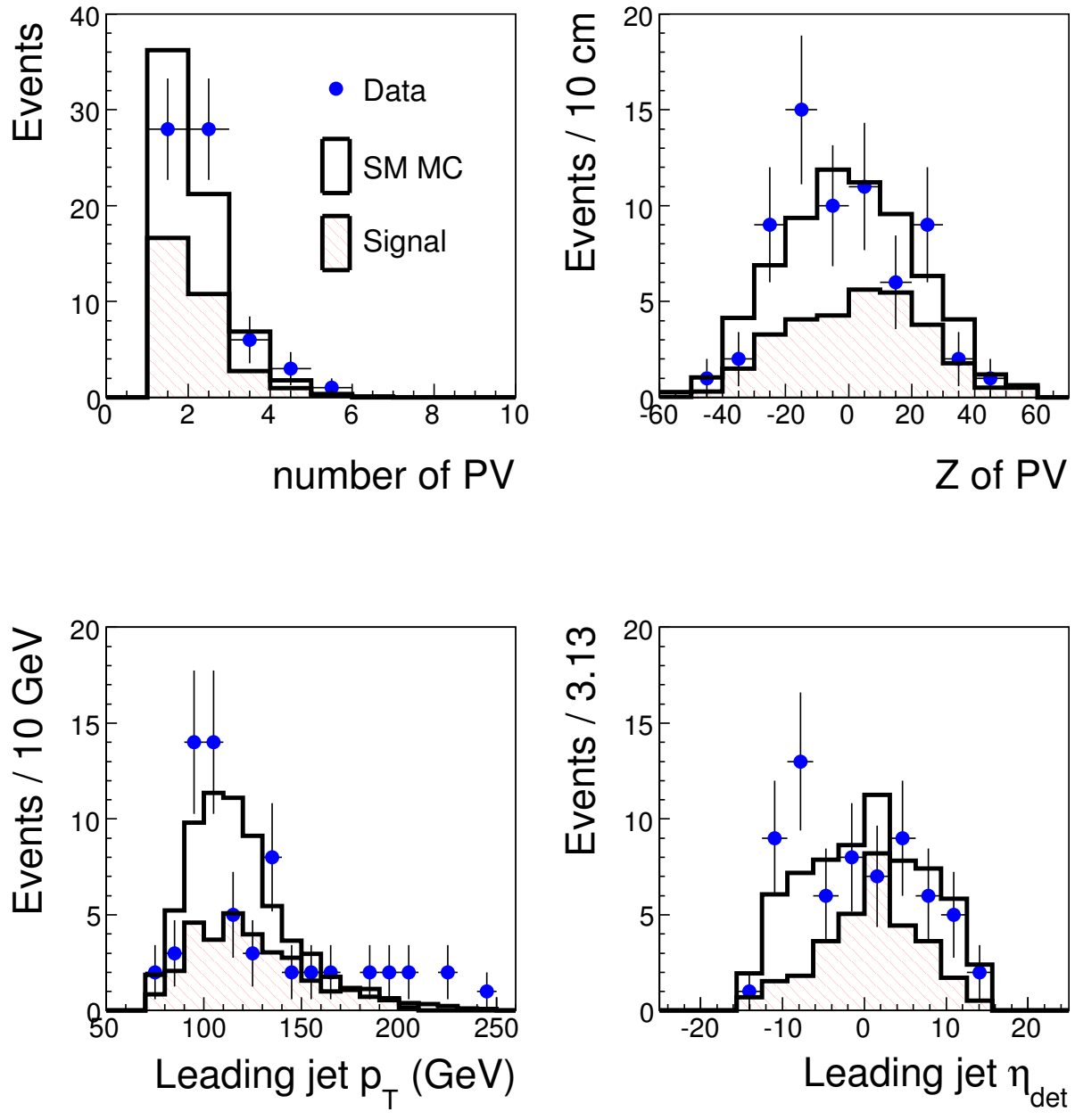

Figure B.2: Distributions for number of primary vertices, z position of the primary vertex, leading jet p_T and leading jet η_{det} after requiring the selection criteria optimized for $\tilde{t}_1$ masses between 150 GeV to 160 GeV for data (points with error bars), SM background (solid histogram), and a signal with $m_{\tilde{t}_1} = 150$ GeV and $m_{\tilde{\chi}_1^0} = 70$ GeV (hatched histogram).

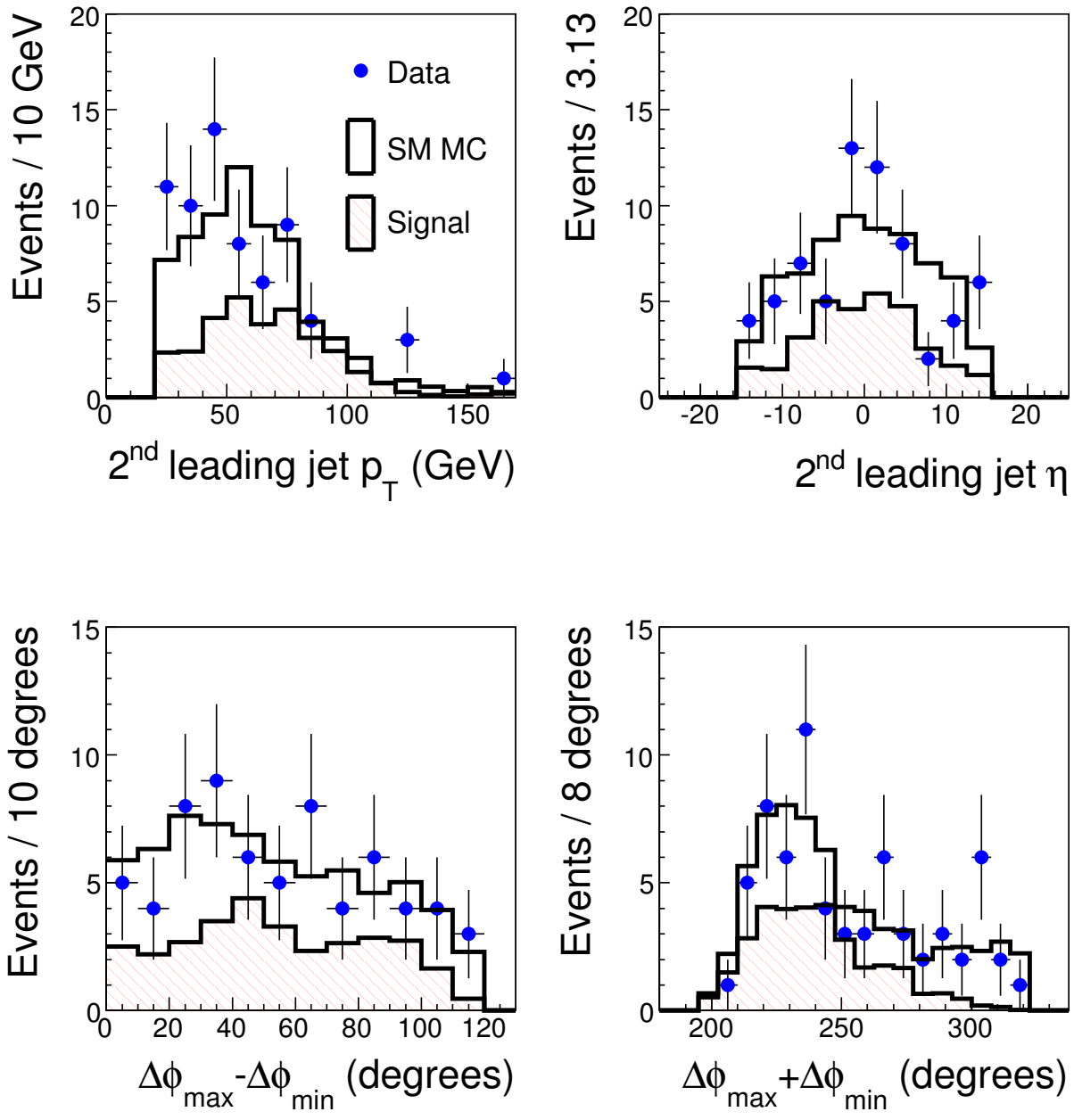

Figure B.3: Distributions for second leading jet p_T, second leading jet $\eta_{\rm det}$, $\Delta\phi_{\rm max} - \Delta\phi_{\rm min}$, $\Delta\phi_{\rm max} + \Delta\phi_{\rm min}$ after requiring the selection criteria optimized for $\tilde{t}_1$ masses between 150 GeV to 160 GeV for data (points with error bars), SM background (solid histogram), and a signal with $m_{\tilde{t}_1} = 150$ GeV and $m_{\tilde{\chi}^0_1} = 70$ GeV (hatched histogram).

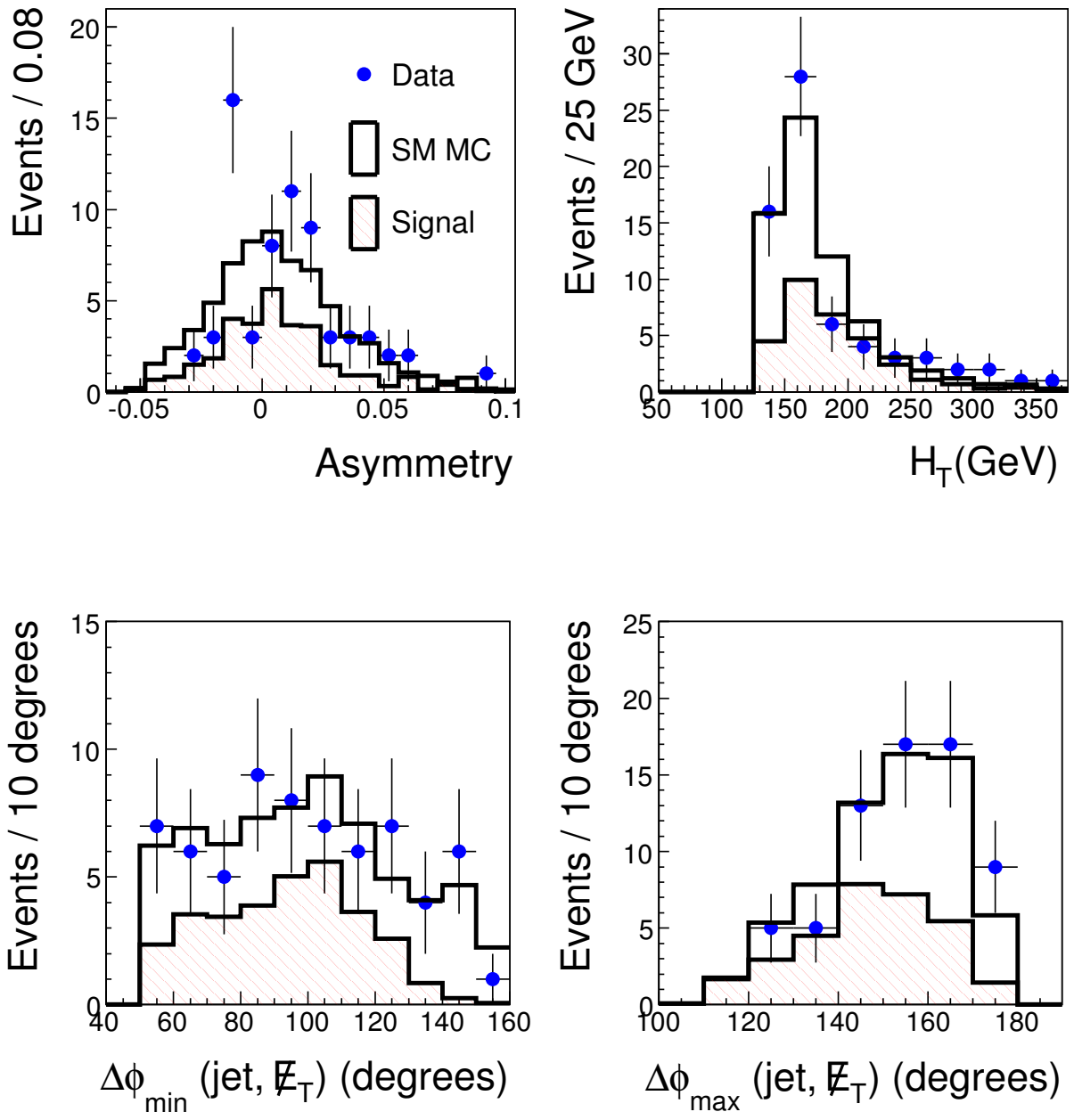

Figure B.4: Distributions for asymmetry, H_T, $\Delta\phi_{\rm min}$(jet,$\not\!\!E_T$) and $\Delta\phi_{\rm max}$(jet,$\not\!\!E_T$) after requiring the selection criteria optimized for $\tilde{t}_1$ masses between 150 GeV to 160 GeV for data (points with error bars), SM background (solid histogram), and a signal with $m_{\tilde{t}_1} = 150$ GeV and $m_{\tilde{\chi}^0_1} = 70$ GeV (hatched histogram).

VITA

Mansoora Shamim was born in Ali Pur, Pakistan in 1976. She graduated from Sir Syed Girls High School, Lalamusa in 1991. After completing her bachelors in 1995 from Lahore College for Women, she joined University of the Punjab, Lahore in 1996 from where she graduated in 1998 with a Masters degree in physics. On completion of her Masters she was awarded a one year scholarship by the Abdus Salam international center for theoretical physics (ICTP). She stayed in Trieste, Italy from August 1999-August 2000 and completed a diploma course in theoretical high energy physics. Before joining Kansas State University in summer 2001, she taught physics to the M. Sc. students at Punjab university during her stay in Pakistan from September 2000-June 2001. After completing the course work at KSU in May 2003, she moved to Fermilab in Batavia, IL to conduct her research in the experimental high energy physics under the guidance of Prof. Tim Bolton. She is expected to graduate from KSU in May 2008 with a Ph.D degree in experimental high energy physics. The results obtained during her Ph.D work have been submitted to Physics Letters B for publication.